Published for SISSA by Springer

Received: *July 5, 2018*
Accepted: *August 8, 2018*
Published: *August 27, 2018*

Holographic entanglement entropy in $AdS_4/BCFT_3$ and the Willmore functional

Domenico Seminara,[a] **Jacopo Sisti**[b] **and Erik Tonni**[b]

[a] *Dipartimento di Fisica, Università di Firenze and INFN Sezione di Firenze, Via G. Sansone 1, 50019 Sesto Fiorentino, Italy*
[b] *SISSA and INFN, via Bonomea 265, 34136, Trieste, Italy*

E-mail: seminara@fi.infn.it, jsisti@sissa.it, erik.tonni@sissa.it

Abstract: We study the holographic entanglement entropy of spatial regions having arbitrary shapes in the $AdS_4/BCFT_3$ correspondence with static gravitational backgrounds, focusing on the subleading term with respect to the area law term in its expansion as the UV cutoff vanishes. An analytic expression depending on the unit vector normal to the minimal area surface anchored to the entangling curve is obtained. When the bulk spacetime is a part of AdS_4, this formula becomes the Willmore functional with a proper boundary term evaluated on the minimal surface viewed as a submanifold of a three dimensional flat Euclidean space with boundary. For some smooth domains, the analytic expressions of the finite term are reproduced, including the case of a disk disjoint from a boundary which is either flat or circular. When the spatial region contains corners adjacent to the boundary, the subleading term is a logarithmic divergence whose coefficient is determined by a corner function that is known analytically, and this result is also recovered. A numerical approach is employed to construct extremal surfaces anchored to entangling curves with arbitrary shapes. This analysis is used both to check some analytic results and to find numerically the finite term of the holographic entanglement entropy for some ellipses at finite distance from a flat boundary.

Keywords: AdS-CFT Correspondence, Boundary Quantum Field Theory

ArXiv ePrint: 1805.11551

https://doi.org/10.1007/JHEP08(2018)164

JHEP08(2018)164

Contents

JHEP08(2018)164

1 Introduction

Entanglement has attracted an intense research activity during the last two decades in quantum field theory, quantum gravity, quantum many-body systems and quantum information (see [1–5] for reviews). Among the entanglement indicators, the entanglement entropy plays a dominant role because it quantifies the entanglement of a bipartition when the entire quantum system is in a pure state.

Given the Hilbert space $\mathcal{H}$ associated to a quantum system in the state characterised by the density matrix ρ, and assuming that it is bipartite as $\mathcal{H} = \mathcal{H}_A \otimes \mathcal{H}_B$, the A's reduced density matrix is $\rho_A = \mathrm{Tr}_{\mathcal{H}_B}\rho$ and the entanglement entropy between A and B is defined as the Von Neumann entropy of ρ_A, namely $S_A = -\mathrm{Tr}(\rho_A \log \rho_A)$. Similarly, the entanglement entropy S_B is the Von Neumann entropy of B's reduced density matrix $\rho_B = \mathrm{Tr}_{\mathcal{H}_A}\rho$. When ρ is a pure state, we have $S_A = S_B$. Hereafter we only consider spatial bipartitions where A is a spatial region and B its complement.

In the approach to quantum gravity based on the gauge/gravity correspondence, a crucial result was found by Ryu and Takayanagi [6, 7], who proposed the holographic formula to compute the entanglement entropy of a $d+1$ dimensional CFT at strong coupling with a gravitational dual description characterised by an asymptotically AdS_{d+2} spacetime. This prescription has been extended to time dependent backgrounds in [8]. Recently, an interesting reformulation of the holographic entanglement entropy through some peculiar flows has been proposed in [9] and explored further in [10].

In this manuscript, for simplicity, only static spacetimes are considered. By introducing the coordinate $z > 0$ along the holographic direction in the gravitational spacetime, the dual CFT_{d+1} is defined on the conformal boundary at $z = 0$. Given a region A in a spatial slice of the CFT_{d+1}, its holographic entanglement entropy at strong coupling is obtained from the area of the d dimensional minimal area hypersurface $\hat{\gamma}_A$ anchored to the boundary of A (i.e. such that $\partial\hat{\gamma}_A = \partial A$) and homologous to A [11, 12]. Since the asymptotically AdS_{d+2} gravitational spacetime is noncompact along the holographic direction and $\hat{\gamma}_A$ reaches its boundary, the area of $\hat{\gamma}_A$ diverges. This divergence is usually regularised by introducing a cutoff $\varepsilon > 0$ in the holographic direction z (i.e. $z \geqslant \varepsilon$) such that $\varepsilon \ll \mathrm{Area}(\partial A)$, which corresponds to the gravitational dual of the UV cutoff in the CFT_{d+1}. Denoting by $\hat{\gamma}_\varepsilon \equiv \hat{\gamma}_A \cap \{z \geqslant \varepsilon\}$ the restriction of $\hat{\gamma}_A$ to $z \geqslant \varepsilon$, the holographic entanglement entropy is given by

$$S_A = \frac{\mathrm{Area}(\hat{\gamma}_\varepsilon)}{4G_{\mathrm{N}}} \tag{1.1}$$

being G_{N} the $d+2$ dimensional gravitational Newton constant.

By expanding the r.h.s. of (1.1) as $\varepsilon \to 0^+$, the leading divergence is $O(1/\varepsilon^{d-1})$ and its coefficient is proportional to the area of the hypersurface $\partial A \cap \partial B$ which separates A and B (entangling surface). The terms subleading with respect to the area law provide important information. For instance, in $d = 3$ and for smooth ∂A, a logarithmic divergence occurs and its coefficient contains the anomaly coefficients of the CFT_4 [13–15].

In this manuscript, we focus on $d = 2$, where (1.1) becomes

$$S_A = \frac{L^2_{\mathrm{AdS}}}{4G_{\mathrm{N}}}\,\mathcal{A}[\hat{\gamma}_\varepsilon] \tag{1.2}$$

JHEP08(2018)164

where the dependence on the AdS radius $L_{\rm AdS}$ has been factored out and the area $\mathcal{A}[\hat{\gamma}_\varepsilon]$ of the two dimensional surface $\hat{\gamma}_\varepsilon$ must be evaluated by setting $L^2_{\rm AdS}=1$. In $\mathrm{AdS}_4/\mathrm{CFT}_3$, the minimal area surface $\hat{\gamma}_A$ is anchored to the entangling curve $\partial A=\partial B$ and the expansion of $\mathcal{A}[\hat{\gamma}_\varepsilon]$ as $\varepsilon\to 0$ reads

$$\mathcal{A}[\hat{\gamma}_\varepsilon]=\frac{P_A}{\varepsilon}-F_A+o(1) \tag{1.3}$$

where $P_A=\text{length}(\partial A)=\text{length}(\partial B)$ is the perimeter of A.

In three dimensional quantum field theories, the subleading term with respect to the area law in S_A is finite for smooth entangling curves and it contains relevant information. For instance, when A is a disk, it has been shown that this term decreases along a renormalization group flow going from an ultraviolet to an infrared fixed point [16–21]. In a CFT_3, when A contains corners, the subleading term with respect to the area law is a logarithmic divergence whose coefficient is determined by a model dependent corner function [22–26]. The limit of this function as the corner disappears provides the coefficient characterising the two point function of the stress tensor [27–30].

These important results tell that it is useful to study the shape dependence of the subleading term with respect to the area law in S_A. Nonetheless, it is very difficult to get analytic expressions valid for generic shapes, even for simple quantum field theories. This problem has been tackled for the holographic entanglement entropy in $\mathrm{AdS}_4/\mathrm{CFT}_3$. Interesting results have been obtained for regions given by small perturbations of the disk and for star shaped domains [31–34]. When A has a generic shape, analytic expressions for F_A can be written where the Willmore functional [35–39] plays an important role. The first result has been found in [40] for the static case where the gravitational background is AdS_4. This analysis has been further developed in [41] and then extended to a generic asymptotically AdS_4 spacetime in [42]. In [42] the analytic results have been also checked against numerical data obtained with *Surface Evolver* [43, 44], which has been first employed to study the holographic entanglement entropy in [45]. The analytic expressions for F_A found in [40–42] hold also when A is made by disjoint regions. We remark that, in CFT_3, it is very difficult to find analytic results about the entanglement entropy of disjoint regions [46, 47]. Also in CFT_2, where the conformal symmetry is more powerful, few analytic results are available when the subsystem is made by disjoint intervals [48–52].

Conformal field theories in the presence of boundaries (BCFTs) have been largely studied in the literature [53–64] and also their gravitational duals through the gauge/gravity correspondence (which is called AdS/BCFT in these cases) have been constructed [65–85]. These gravitational backgrounds are part of asymptotically AdS spacetimes delimited by a hypersurface $\mathcal{Q}$ extended in the bulk whose boundary coincides with the boundary of the dual BCFT [68–74].

We are interested in the shape dependence of the holographic entanglement entropy in AdS/BCFT through the prescription (1.1). Given a spatial region A in a spatial slice of the BCFT, the holographic entanglement entropy is determined by the minimal area hypersurface $\hat{\gamma}_A$ anchored to the entangling surface $\partial A\cap\partial B$. Whenever ∂A intersects the boundary of the BCFT, we have $\partial A\cap\partial B\subsetneq\partial A$ and the area of $\partial A\cap\partial B$ occurs in the leading divergence (area law term). Another peculiar feature of extremal hypersurfaces in

JHEP08(2018)164

the context of AdS/BCFT is that $\hat{\gamma}_A$ may intersect $\mathcal{Q}$ (with a slight abuse of notation, in the following we will denote in the same way $\mathcal{Q}$ and its spatial section). It is important to remark that, since $\hat{\gamma}_A \cap \mathcal{Q}$ is not fixed, the extremization of the area functional leads to the condition that $\hat{\gamma}_A$ intersects $\mathcal{Q}$ orthogonally. Furthermore, as discussed above, in order to evaluate the holographic entanglement entropy we have to introduce the UV cutoff ε and consider the area of the restricted hypersurface $\hat{\gamma}_\varepsilon \equiv \hat{\gamma}_A \cap \{z \geqslant \varepsilon\}$ because $\hat{\gamma}_A$ reaches the conformal boundary of an asymptotically AdS space.

In this manuscript, we consider the holographic entanglement entropy in $\mathrm{AdS}_4/\mathrm{BCFT}_3$ of spatial regions A having an arbitrary shape. For the sake of simplicity, we will consider static backgrounds in $\mathrm{AdS}_4/\mathrm{BCFT}_3$, which provide the simplest arena where the shape dependence plays an important role. The holographic entanglement entropy is computed through (1.2), where the minimal area surface $\hat{\gamma}_A$ is anchored to the entangling curve and it can intersect orthogonally $\mathcal{Q}$ (see also footnote 11 of [10]).

The expansion of the area $\mathcal{A}[\hat{\gamma}_\varepsilon]$ of the two dimensional surface $\hat{\gamma}_\varepsilon$ in (1.2) as $\varepsilon \to 0$ reads

$$\mathcal{A}[\hat{\gamma}_\varepsilon] = \frac{P_{A,B}}{\varepsilon} - F_A + o(1) \tag{1.4}$$

being $P_{A,B} = \mathrm{length}(\partial A \cap \partial B) \leqslant P_A$ the length of the entangling curve. When ∂A is smooth, F_A is finite. It is worth considering the configurations whose subleading term F_A can be computed analytically. For instance, the case of an infinite strip parallel to a flat boundary has been considered in [72, 73, 86, 87].

When A contains corners, the subleading term F_A diverges logarithmically and the coefficient of this divergence is determined by different kinds of corner functions, depending on the position of the tips of the corners. For the corners whose tip is not on the boundary of the BCFT_3, the well known corner function of [22, 23] must be employed. If the tip of the corner is located on the boundary of the BCFT_3, the corner functions encode also the boundary conditions characterising the BCFT_3. In the context of $\mathrm{AdS}_4/\mathrm{BCFT}_3$, these corner functions have been studied analytically in [87] by computing the holographic entanglement entropy of an infinite wedge. For instance, when A is an infinite wedge adjacent to a flat boundary, the holographic entanglement entropy is given by (1.2) with

$$\mathcal{A}[\hat{\gamma}_\varepsilon] = \frac{L}{\varepsilon} - F_\alpha(\omega)\, \log(L/\varepsilon) + O(1) \tag{1.5}$$

where $L \gg \varepsilon$ is an infrared cutoff, ω is the opening angle of the wedge and the subindex α denotes the fact that the corner function $F_\alpha(\omega)$ depends on the boundary conditions in a highly non trivial way. The analytic expression of $F_\alpha(\omega)$ has been checked numerically by employing Surface Evolver [87].

1.1 Summary of the results

In this manuscript, we study the subleading term F_A of the holographic entanglement entropy in $\mathrm{AdS}_4/\mathrm{BCFT}_3$ (see (1.2) and (1.4)) for entangling curves having arbitrary shapes.

After a brief description of the AdS/BCFT setup [68–74], in section 2 we adapt the method employed in [40–42] for the holographic entanglement entropy in $\mathrm{AdS}_4/\mathrm{CFT}_3$ to

JHEP08(2018)164

this case. This analysis leads to writing F_A as a functional evaluated on the surface $\hat{\gamma}_\varepsilon$ embedded in a three dimensional Euclidean space with boundary which is asymptotically flat close to the boundary. This result holds for any static gravitational background and for any region, even when it is made by disjoint domains. Focusing on the simplest $AdS_4/BCFT_3$ setup, where the gravitational background is a part of $\mathbb{H}_3$ and the asymptotically flat space is a part of $\mathbb{R}^3$, in section 2.2 we observe that the functional obtained for F_A becomes the Willmore functional [35–39] with a proper boundary term evaluated on the surface $\hat{\gamma}_\varepsilon$ embedded in $\mathbb{R}^3$. In the remaining part of the manuscript, further simplifications are introduced by restricting to $BCFT_3$'s whose spatial slice is either a half plane (see section 2.2.1) or a disk (see section 2.2.2).

The analytic expression found for F_A is checked by considering some particular regions such that the corresponding F_A can be found analytically. In section 3 we recover the result for an infinite strip parallel to a flat boundary [72, 73, 86, 87]. When A is a finite region with smooth ∂A that does not intersect the boundary, F_A is finite. The simplest configuration to consider is a disk disjoint from a boundary which is either flat or circular. In section 4 we compute F_A analytically for these configurations and check the results against numerical data obtained through Surface Evolver. We remark that Surface Evolver is a very powerful tool in this analysis because it allows to study numerically any kind of region A, even when it is made by disjoint connected domains or when it contains corners (see [45, 87] for some examples in AdS_4). In section 5 Surface Evolver is employed to find numerically F_A corresponding to some ellipses disjoint from a flat boundary.

In section 6 we check that the result derived in section 2.2 for F_A can be applied also when A contains corners by considering the explicit cases of a half disk (see section 6.1) and an infinite wedge adjacent to the flat boundary (see section 6.2). The analytic expression for the corner function $F_\alpha(\omega)$ found in [87] is recovered from the general expression of F_A obtained in section 2.2.

In appendix A we report the mappings that are employed to study the disk disjoint from a flat boundary. The appendix B contains the technical details for the derivation of the analytic results presented in section 4 about a disk concentric to a circular boundary. In appendix C we discuss the details underlying the derivation of the corner function of [87] through the general formula for F_A of section 2.2.1. In appendix D we further discuss the auxiliary surfaces corresponding to some extremal surfaces occurring in the manuscript.

2 Holographic entanglement entropy in $AdS_4/BCFT_3$

In this section we provide an analytic formula for the subleading term F_A of the holographic entanglement entropy in $AdS_4/BCFT_3$ which is valid for any region A and any static background. In section 2.1 we derive the general formula and in section 2.2 we describe how it simplifies when the gravitational background is a part of AdS_4, focusing on the simplest cases where the boundary of a spatial slice of the $BCFT_3$ is either an infinite line or a circle.

Following [68], we consider the gravitational background dual to a $BCFT_{d+1}$ given by an asymptotically AdS_{d+2} spacetime $\mathcal{M}$ restricted by the occurrence of a $d+1$ dimensional hypersurface $\mathcal{Q}$ in the bulk whose boundary coincides with the boundary of the

JHEP08(2018)164

BCFT_{d+1}. Hence the boundary of $\mathcal{M}$ is the union of $\mathcal{Q}$ and the conformal boundary where the BCFT_{d+1} is defined. The gravitational action for the $d+2$ dimensional metric G_{ab} in the bulk reads [68, 69]

$$\mathcal{I} = \frac{1}{16\pi G_{\text{N}}} \int_{\mathcal{M}} \sqrt{-G}\,(R - 2\Lambda) + \frac{1}{8\pi G_{\text{N}}} \int_{\mathcal{Q}} \sqrt{-H}\,K + \mathcal{I}_{\mathcal{Q}} \tag{2.1}$$

being $\Lambda = -\frac{d(d+1)}{2L^2_{\text{AdS}}}$ the negative cosmological constant, H_{ab} the induced metric on $\mathcal{Q}$ and $K = H^{ab}K_{ab}$ the trace of the extrinsic curvature K_{ab} of $\mathcal{Q}$. The boundary term $\mathcal{I}_{\mathcal{Q}}$ describes some matter fields localised on $\mathcal{Q}$. The boundary term due to the fact that ∂M is non smooth [88, 89] along the boundary of the BCFT_{d+1} and the ones introduced by the holographic renormalisation procedure [90–93] have been omitted because they are not relevant in our analysis. We will focus only on static backgrounds.

While in section 2.1 a generic $\mathcal{Q}$ is considered, for the remaining part of the manuscript we focus on the simplest case where $\mathcal{I}_{\mathcal{Q}}$ in (2.1) is given by

$$\mathcal{I}_{\mathcal{Q}} = -\frac{T}{8\pi G_{\text{N}}} \int_{\mathcal{Q}} \sqrt{-H} \tag{2.2}$$

being T a constant real parameter characterising the hypersurface $\mathcal{Q}$. Different proposals have been made to construct $\mathcal{Q}$ [68, 71–73], but they will not be discussed here because our results can be employed independently of the way underlying the construction of $\mathcal{Q}$.

In this manuscript, we consider the holographic entanglement entropy in $\text{AdS}_4/\text{BCFT}_3$ with static gravitational backgrounds.

Given a two dimensional region A in the spatial slice of the BCFT_3, the corresponding holographic entanglement entropy is given by (1.2) and (1.4), as discussed in section 1. The minimal area surface $\hat{\gamma}_A$ is anchored to the entangling curve $\partial A \cap \partial B$ and, whenever $\hat{\gamma}_A \cap \mathcal{Q} \neq \emptyset$, these two surfaces are orthogonal along their intersection. We remind that the expansion (1.4) is defined by first introducing the UV cutoff ε and then computing the area of the part of $\hat{\gamma}_A$ restricted to $z \geqslant \varepsilon$, namely $\hat{\gamma}_\varepsilon \equiv \hat{\gamma}_A \cap \{z \geqslant \varepsilon\}$. By employing the method of [40–42], in section 2.1 we find an analytic expression for the subleading term F_A in (1.4) that is valid for any region A and for any static gravitational background.

2.1 Static backgrounds

In the $\text{AdS}_4/\text{BCFT}_3$ setup described above, let us denote by $\mathcal{M}_3$ the three dimensional Euclidean space with metric $g_{\mu\nu}$ obtained by taking a constant time slice of the static asymptotically AdS_4 gravitational background. The boundary of $\mathcal{M}_3$ is the union of the conformal boundary, which is the constant time slice of the spacetime where the BCFT_3 is defined, and the surface $\mathcal{Q}$ delimiting the gravitational bulk.

Let us consider a two dimensional surface γ embedded into $\mathcal{M}_3$ whose boundary $\partial\gamma$ is made by either one or many disjoint closed curves. Denoting by n_μ the spacelike unit vector normal to γ, the metric induced on γ (first fundamental form) and the extrinsic curvature of γ (second fundamental form) are given respectively by

$$h_{\mu\nu} = g_{\mu\nu} - n_\mu n_\nu \qquad\qquad K_{\mu\nu} = h_\mu{}^\alpha h_\nu{}^\beta \nabla_\alpha n_\beta \tag{2.3}$$

where ∇_α is the torsionless covariant derivative compatible with $g_{\mu\nu}$.

JHEP08(2018)164

In our analysis $g_{\mu\nu}$ is conformally equivalent to the metric $\tilde{g}_{\mu\nu}$ corresponding to a Euclidean space $\widetilde{\mathcal{M}}_3$ which is asymptotically flat near the conformal boundary, namely

$$g_{\mu\nu} = e^{2\varphi}\, \tilde{g}_{\mu\nu} \tag{2.4}$$

where φ is a function of the coordinates. The two dimensional surface γ is also a submanifold of $\widetilde{\mathcal{M}}_3$. Denoting by $\tilde{n}_\mu$ the spacelike unit vector normal to $\gamma \subset \widetilde{\mathcal{M}}_3$, we have that $n_\mu = e^{\varphi}\, \tilde{n}_\mu$. The fundamental forms in (2.3) can be written in terms of the fundamental forms $\tilde{h}_{\mu\nu}$ and $\widetilde{K}_{\mu\nu}$ characterising the embedding $\gamma \subset \widetilde{\mathcal{M}}_3$ as follows

$$h_{\mu\nu} = e^{2\varphi}\, \tilde{h}_{\mu\nu} \qquad\qquad K_{\mu\nu} = e^{\varphi}\big(\widetilde{K}_{\mu\nu} + \tilde{h}_{\mu\nu}\, \tilde{n}^\lambda \partial_\lambda \varphi\big) \tag{2.5}$$

The area $\mathcal{A}[\gamma]$ of the surface γ can be written as [42]

$$\begin{aligned}\mathcal{A}[\gamma] = \oint_{\partial\gamma} \tilde{b}^\mu \partial_\mu \varphi\, d\tilde{s} + \frac{1}{4}\int_\gamma \big(\mathrm{Tr}K\big)^2\, d\mathcal{A} \\ - \int_\gamma \left(\frac{1}{4}\big(\mathrm{Tr}\widetilde{K}\big)^2 + \widetilde{\nabla}^2\varphi - e^{2\varphi} - \tilde{n}^\mu \tilde{n}^\nu\, \widetilde{\nabla}_\mu \widetilde{\nabla}_\nu \varphi + \big(\tilde{n}^\lambda \partial_\lambda \varphi\big)^2 \right) d\tilde{\mathcal{A}}\end{aligned} \tag{2.6}$$

where $\widetilde{\nabla}_\alpha$ is the torsionless covariant derivative compatible with $\tilde{g}_{\mu\nu}$ and $\tilde{b}^\mu$ is the unit vector on $\partial\gamma$ that is tangent to γ, orthogonal to $\partial\gamma$ and outward pointing with respect to γ. The area element $d\mathcal{A} = \sqrt{h}\, d\Sigma$ of $\gamma \subset \mathcal{M}_3$ and the area element $d\tilde{\mathcal{A}} = \sqrt{\tilde{h}}\, d\Sigma$ of $\gamma \subset \widetilde{\mathcal{M}}_3$ are related as $d\mathcal{A} = e^{2\varphi} d\tilde{\mathcal{A}}$, being $d\Sigma = d\sigma_1 d\sigma_2$, where σ_i are some local coordinates on γ.

If part of γ belongs to the conformal boundary at $z = 0$, the area (2.6) in infinite because of the behaviour of the metric $h_{\mu\nu}$ near the conformal boundary. In order to regularise the area, one introduces the UV cutoff ε and considers the part of γ given by $\gamma_\varepsilon \equiv \gamma \cap \{z \geqslant \varepsilon\}$. The curve $\partial\gamma_\varepsilon$ can be decomposed as $\partial\gamma_\varepsilon = \partial\gamma_{\mathcal{Q}} \cup \partial\gamma_{\shortparallel}$, where $\partial\gamma_{\mathcal{Q}} \equiv \gamma_\varepsilon \cap \mathcal{Q}$ and $\partial\gamma_{\shortparallel} \equiv \gamma_\varepsilon \cap \{z = \varepsilon\}$ are not necessarily closed lines. Consequently, for the surfaces γ_ε the boundary term in (2.6) can be written as

$$\oint_{\partial\gamma_\varepsilon} \tilde{b}^\mu \partial_\mu \varphi\, d\tilde{s} = \int_{\partial\gamma_{\shortparallel}} \tilde{b}^\mu \partial_\mu \varphi\, d\tilde{s} + \int_{\partial\gamma_{\mathcal{Q}}} \tilde{b}^\mu \partial_\mu \varphi\, d\tilde{s} \tag{2.7}$$

Let us consider the integral over $\partial\gamma_{\shortparallel}$ in the r.h.s. of this expression. Since in our analysis $\varphi = -\log(z) + O(z^a)$ with $a > 1$ as $z \to 0$, we need to know the behaviour of the component $\tilde{b}^z$ at $z = \varepsilon$ as $\varepsilon \to 0$. If $\tilde{b}^z = -1 + o(\varepsilon)$, for the integral over $\partial\gamma_{\shortparallel}$ in (2.7) we obtain the following expansion

$$\int_{\partial\hat{\gamma}_{\shortparallel}} \tilde{b}^\mu \partial_\mu \varphi\, d\tilde{s} = \frac{P_{A,B}}{\varepsilon} + o(1) \tag{2.8}$$

as $\varepsilon \to 0$, being $P_{A,B} = \mathrm{length}(\partial A \cap \partial B)$ the length of the entangling curve. The above expansion for $\tilde{b}^z$ holds for any surface, not necessarily minimal, which intersects the conformal boundary orthogonally [41]. Hereafter we will consider only this class of surfaces, which includes also the extremal surfaces, which are compelled to intersect orthogonally the conformal boundary [40–42, 94].

JHEP08(2018)164

By plugging (2.8) into (2.7) first and then substituting the resulting expression into (2.6), for the area of the surfaces γ_ε we find the following expansion

$$\mathcal{A}[\gamma_\varepsilon] = \frac{P_{A,B}}{\varepsilon} + \int_{\partial\gamma_\mathcal{Q}} \tilde{b}^\mu \partial_\mu \varphi \, d\tilde{s} + \frac{1}{4}\int_{\gamma_\varepsilon} \big(\mathrm{Tr}K\big)^2 \, d\mathcal{A} \\ - \int_{\gamma_\varepsilon} \left(\frac{1}{4}\big(\mathrm{Tr}\widetilde{K}\big)^2 + \widetilde{\nabla}^2\varphi - e^{2\varphi} - \tilde{n}^\mu\tilde{n}^\nu\, \widetilde{\nabla}_\mu\widetilde{\nabla}_\nu\varphi + \big(\tilde{n}^\lambda\partial_\lambda\varphi\big)^2 \right) d\tilde{\mathcal{A}} + o(1) \tag{2.9}$$

as $\varepsilon \to 0$. We remark that (2.9) also holds for surfaces γ_ε that are not extremal of the area functional. Furthermore, no restrictions are imposed along the curve $\partial\gamma_\mathcal{Q}$.

In order to compute the holographic entanglement entropy in $\mathrm{AdS}_4/\mathrm{BCFT}_3$ through (1.2), we must consider the minimal area surface $\hat{\gamma}_A$ which is anchored to the entangling curve $\partial A \cap \partial B$. This implies that $\hat{\gamma}_A$ intersects the surface $\mathcal{Q}$ orthogonally, whenever $\hat{\gamma}_A \cap \mathcal{Q} \neq \emptyset$. The expression (2.9) significantly simplifies for the extremal surfaces $\hat{\gamma}_\varepsilon \equiv \hat{\gamma}_A \cap \{z \geqslant \varepsilon\}$ (with a slight abuse of notation, sometimes we denote by $\hat{\gamma}_A$ also extremal surfaces which are not the global minimum). The local extrema of the area functional are the solutions of the following equation

$$\mathrm{Tr}K = 0 \quad \Longleftrightarrow \quad \big(\mathrm{Tr}\widetilde{K}\big)^2 = 4(\tilde{n}^\lambda\partial_\lambda\varphi)^2 \tag{2.10}$$

which, furthermore, intersect orthogonally $\mathcal{Q}$ whenever $\hat{\gamma}_A \cap \mathcal{Q} \neq \emptyset$. The second expression in (2.10) has been obtained by using the second formula in (2.5).

Plugging the extremality condition (2.10) into (2.9), we find the expansion of $\mathcal{A}[\hat{\gamma}_\varepsilon]$ as $\varepsilon \to 0$, which provides the holographic entanglement entropy of a region A in $\mathrm{AdS}_4/\mathrm{BCFT}_3$ for static gravitational backgrounds. It reads

$$\mathcal{A}[\hat{\gamma}_\varepsilon] = \frac{P_{A,B}}{\varepsilon} + \int_{\partial\hat{\gamma}_\mathcal{Q}} \tilde{b}^\mu \partial_\mu \varphi \, d\tilde{s} - \int_{\hat{\gamma}_\varepsilon} \left(\frac{1}{2}\big(\mathrm{Tr}\widetilde{K}\big)^2 + \widetilde{\nabla}^2\varphi - e^{2\varphi} - \tilde{n}^\mu\tilde{n}^\nu\, \widetilde{\nabla}_\mu\widetilde{\nabla}_\nu\varphi \right) d\tilde{\mathcal{A}} + o(1) \tag{2.11}$$

where the leading divergence gives the expected area law term for the holographic entanglement entropy in $\mathrm{AdS}_4/\mathrm{BCFT}_3$. Comparing (2.11) with the expansion (1.4) expected for $\mathcal{A}[\hat{\gamma}_\varepsilon]$, we find that the subleading term is given by

$$F_A = \int_{\hat{\gamma}_\varepsilon} \left(\frac{1}{2}\big(\mathrm{Tr}\widetilde{K}\big)^2 + \widetilde{\nabla}^2\varphi - e^{2\varphi} - \tilde{n}^\mu\tilde{n}^\nu\, \widetilde{\nabla}_\mu\widetilde{\nabla}_\nu\varphi \right) d\tilde{\mathcal{A}} - \int_{\partial\hat{\gamma}_\mathcal{Q}} \tilde{b}^\mu \partial_\mu \varphi \, d\tilde{s} \tag{2.12}$$

This is the main result of this manuscript. According to (2.12), the subleading term is made by two contributions: an integral over the whole minimal surface $\hat{\gamma}_\varepsilon$ and a line integral over the curve $\partial\hat{\gamma}_\mathcal{Q} = \hat{\gamma}_\varepsilon \cap \mathcal{Q}$. We remark that the definition of $\mathcal{Q}$ has not been employed in the derivation of (2.12).

The integrand of the surface term in (2.12) is the same obtained in [42], where this analysis has been applied for the holographic entanglement entropy in $\mathrm{AdS}_4/\mathrm{CFT}_3$. The holographic entanglement entropy in $\mathrm{AdS}_4/\mathrm{BCFT}_3$ includes the additional term given by the line integral over $\partial\hat{\gamma}_\mathcal{Q}$. This term can be written in a more geometrical form by considering the transformation rule of the geodesic curvature k under Weyl transformations (see e.g. [41])

$$k = e^{-\varphi}\big(\tilde{k} + \tilde{b}^\mu\partial_\mu\varphi\big) \tag{2.13}$$

JHEP08(2018)164

This formula allows to write the line integral over $\partial\gamma_{\mathcal{Q}}$ in (2.12) as follows

$$\int_{\partial\gamma_{\mathcal{Q}}} \tilde{b}^{\mu}\partial_{\mu}\varphi\, d\tilde{s} = \int_{\partial\gamma_{\mathcal{Q}}} k\, ds - \int_{\partial\gamma_{\mathcal{Q}}} \tilde{k}\, d\tilde{s} \tag{2.14}$$

In this manuscript, we consider backgrounds such that $\varphi = -\log(z)$ in (2.4). In these cases, the first and the last term of the integrand in the surface integral in (2.12) become respectively

$$\big(\mathrm{Tr}\widetilde{K}\big)^2 = \frac{4(\tilde{n}^z)^2}{z^2} \qquad \tilde{n}^{\mu}\tilde{n}^{\nu}\,\widetilde{\nabla}_{\mu}\widetilde{\nabla}_{\nu}\varphi = \frac{(\tilde{n}^z)^2}{z^2} + \frac{1}{z}\,\widetilde{\Gamma}^{z}_{\mu\nu}\,\tilde{n}^{\mu}\tilde{n}^{\nu} \tag{2.15}$$

where the first expression has been obtained from the second expression in (2.10) and $\widetilde{\Gamma}^{z}_{\mu\nu}$ are some components of the Christoffel connection compatible with $\tilde{g}_{\mu\nu}$.

2.2 AdS_4

In the remaining part of the manuscript, we focus on the simple gravitational background given by a part of AdS_4 delimited by $\mathcal{Q}$ and the conformal boundary, which provides the gravitational background dual to the ground state of the $BCFT_3$. The metric of AdS_4 in Poincaré coordinates reads

$$ds^2 = \frac{1}{z^2}\Big(-dt^2 + dz^2 + dx^2 + dy^2 \Big) \tag{2.16}$$

where $z > 0$, while the range of the remaining coordinates is $\mathbb{R}$. The metric induced on a $t = \text{const}$ slice of AdS_4 is the one characterising the three dimensional Euclidean hyperbolic space $\mathbb{H}_3$

$$ds^2 = \frac{1}{z^2}\Big(dz^2 + dx^2 + dy^2 \Big) \tag{2.17}$$

Specialising the results of section 2.1 to this background, we have $\mathcal{M}_3 = \mathbb{H}_3$, i.e. $g_{\mu\nu} = \frac{1}{z^2}\,\delta_{\mu\nu}$, which means that $\tilde{g}_{\mu\nu} = \delta_{\mu\nu}$ and $\varphi = -\log(z)$. In this case, drastic simplifications occur (2.12) because $\widetilde{\nabla}^2\varphi - e^{2\varphi} = 0$ and all the components of the connection $\widetilde{\Gamma}^{z}_{\mu\nu}$ vanish identically. Thus, when the gravitational bulk is a proper subset of $\mathbb{H}_3$ delimited by the surface $\mathcal{Q}$ and the conformal boundary, the expression (2.12) for F_A reduces to

$$F_A = \frac{1}{4}\int_{\hat{\gamma}_{\varepsilon}} \big(\mathrm{Tr}\widetilde{K}\big)^2\, d\tilde{\mathcal{A}} + \int_{\partial\hat{\gamma}_{\mathcal{Q}}} \frac{\tilde{b}^{z}}{z}\, d\tilde{s} = \int_{\hat{\gamma}_{\varepsilon}} \frac{(\tilde{n}^z)^2}{z^2}\, d\tilde{\mathcal{A}} + \int_{\partial\hat{\gamma}_{\mathcal{Q}}} \frac{\tilde{b}^{z}}{z}\, d\tilde{s} \tag{2.18}$$

The surface integral over $\hat{\gamma}_{\varepsilon}$ in the first expression is the Willmore functional of $\hat{\gamma}_{\varepsilon} \subset \mathbb{R}^3$. Notice that the curves $\partial\hat{\gamma}_{\mathcal{Q}}$ corresponding to some configurations may intersect the plane given by $z = \varepsilon$.

When A contains corners, the expression (2.18) diverges logarithmically as $\varepsilon \to 0$. In AdS_4/CFT_3, the emergence of the logarithmic divergence from the Willmore functional for domains with corners has been studied in [42], where the corner function found [22, 23] has been recovered. In this $AdS_4/BCFT_3$ setup, the occurrence of a logarithmic divergence in (2.18) for singular domains will be discussed in section 6 and the corner function found in [87] will be obtained.

JHEP08(2018)164

When the entangling curve is a smooth and closed line that does not intersect the spatial boundary of the BCFT$_3$, the limit $\varepsilon \to 0$ of (2.18) provides the following finite expression

$$F_A = \frac{1}{4}\int_{\hat{\gamma}_A} \left(\mathrm{Tr}\widetilde{K}\right)^2 d\tilde{\mathcal{A}} + \int_{\partial\hat{\gamma}_{\mathcal{Q}}} \frac{\tilde{b}^z}{z}\, d\tilde{s} = \int_{\hat{\gamma}_A} \frac{(\tilde{n}^z)^2}{z^2}\, d\tilde{\mathcal{A}} + \int_{\partial\hat{\gamma}_{\mathcal{Q}}} \frac{\tilde{b}^z}{z}\, d\tilde{s} \tag{2.19}$$

which will be largely employed throughout this manuscript.

Hereafter we will focus on BCFT$_3$'s whose spatial slice is either the half plane bounded by a straight line or the disk. In section 2.2.1 and section 2.2.2 some details about these two setups are discussed.

2.2.1 Flat boundary

Let us consider a BCFT$_3$ defined in a spacetime whose generic spatial slice is the half plane $\{(x,y) \in \mathbb{R}^2, x \geqslant 0\}$ bounded by the straight line $x = 0$ (see the grey horizontal half plane and the straight solid black line in figure 1). When the term (2.2) occurs in the gravitational action (2.1), it has been found in [68, 69] that the spatial section of the gravitational background is given by $\mathbb{H}_3$, whose metric is (2.17), bounded by the following half plane $\mathcal{Q}$ in the bulk

$$\mathcal{Q}: \quad x = -(\cot\alpha)\, z \qquad \alpha \in (0,\pi) \qquad z \geqslant 0 \tag{2.20}$$

(the green half plane in figure 1) whose boundary coincides with the straight line $x = 0$ bounding the spatial slice of the BCFT$_3$. The angular parameter α provides the slope of the half plane $\mathcal{Q}$ and it is related to the constant T in (2.2) as $T = (2/L_{\mathrm{AdS}})\cos\alpha$. In particular, a $t = \text{const}$ slice of the gravitational bulk is the part of $\mathbb{H}_3$ defined by

$$x \geqslant -(\cot\alpha)\, z \tag{2.21}$$

The term F_A in the holographic entanglement entropy can be easily obtained by specialising (2.18) to this AdS$_4$/BCFT$_3$ setup. We remark that, for this case, the line integral over $\partial\hat{\gamma}_{\mathcal{Q}}$ in (2.18) simplifies because $\tilde{b}^z = -\cos\alpha$ for all the points of $\partial\hat{\gamma}_{\mathcal{Q}}$. Furthermore, $\tilde{k} = 0$ in (2.14) in this setup, i.e. $\partial\hat{\gamma}_{\mathcal{Q}}$ is a geodesic of $\hat{\gamma}_\varepsilon \in \mathbb{R}^3$. Thus, for any region A in the half plane $x \geqslant 0$, we find

$$F_A = \int_{\hat{\gamma}_\varepsilon} \frac{(\tilde{n}^z)^2}{z^2}\, d\tilde{\mathcal{A}} - (\cos\alpha)\int_{\partial\hat{\gamma}_{\mathcal{Q}}} \frac{1}{z}\, d\tilde{s} \tag{2.22}$$

The two integrals in this expression are always positive, but their relative sign depends on the slope α. In particular, when $\alpha \geqslant \pi/2$ we have $F_A > 0$, while F_A can be negative when $\alpha < \pi/2$ (see e.g. the expression (6.1) for the half disk adjacent to the flat boundary considered in section 6.1).

When ∂A is a closed and smooth curve that does not intersect the boundary $x = 0$, the limit $\varepsilon \to 0$ of (2.22) is finite and one finds

$$F_A = \int_{\hat{\gamma}_A} \frac{(\tilde{n}^z)^2}{z^2}\, d\tilde{\mathcal{A}} - (\cos\alpha)\int_{\partial\hat{\gamma}_{\mathcal{Q}}} \frac{1}{z}\, d\tilde{s} \tag{2.23}$$

which corresponds to (2.19) specialised to this setup.

JHEP08(2018)164

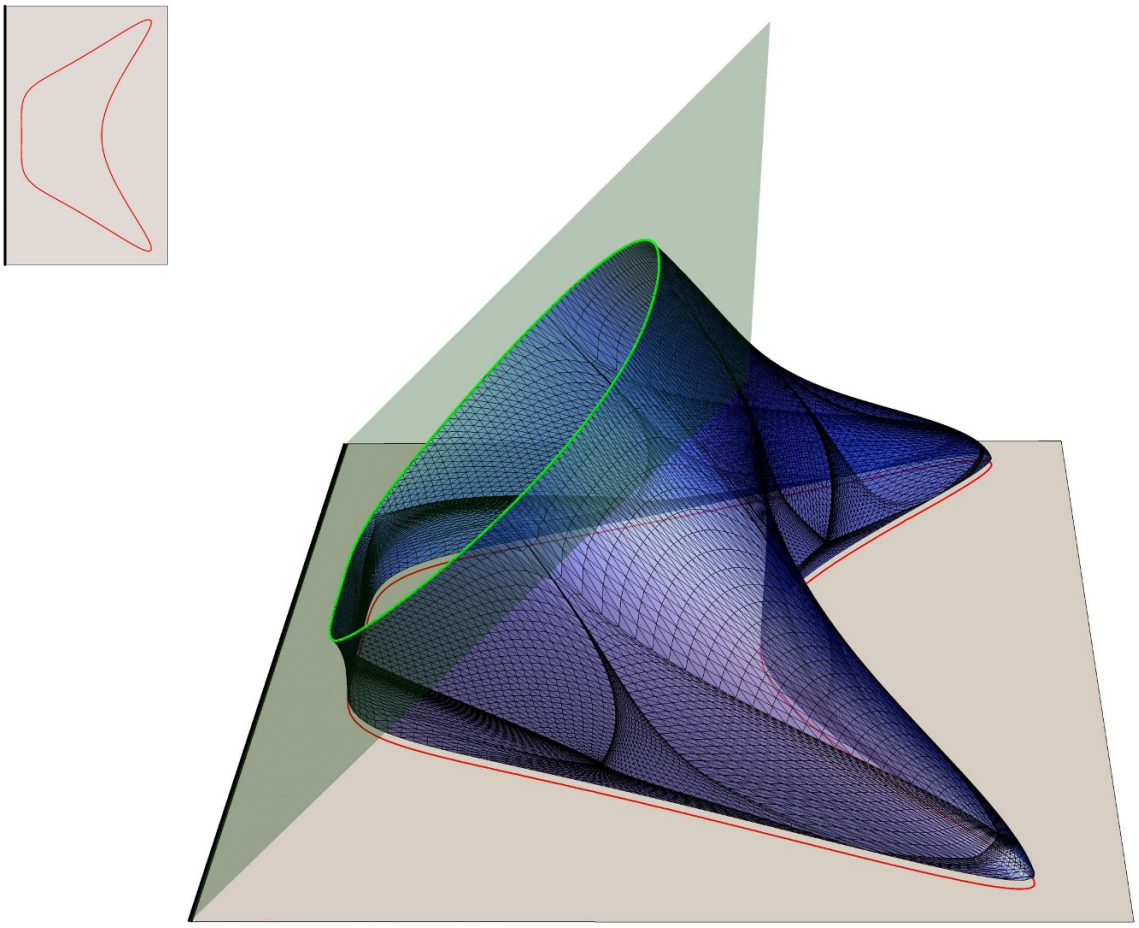

Figure 1. Extremal surface $\hat{\gamma}_\varepsilon$ constructed with Surface Evolver from a spatial domain A in the right half plane (the grey half plane) whose ∂A is the red curve, which is also highlighted in the inset. The gravitational bulk is the part of $\mathbb{H}_3$ defined by (2.21), whose boundary is made by the conformal boundary at $z = 0$ (the grey half plane) and $\mathcal{Q}$ (the green half plane defined in (2.20)). Here $\alpha = 3\pi/4$. The green curve corresponds to $\partial\hat{\gamma}_\mathcal{Q} = \hat{\gamma}_\varepsilon \cap \mathcal{Q}$, and $\hat{\gamma}_\varepsilon$ intersects $\mathcal{Q}$ orthogonally along this curve.

In figure 1 we show an explicit example where (2.23) can be applied. The entangling curve ∂A is the red curve in the $z = 0$ half plane also highlighted in the inset. Surface Evolver has been employed to construct $\hat{\gamma}_\varepsilon$, as done in [87] for other regions in this $AdS_4/BCFT_3$ setup.

2.2.2 Circular boundary

The second setup is given by a $BCFT_3$ defined on a spacetime whose $t =$ const slice is a disk of radius $R_\mathcal{Q}$, that can be conveniently described by introducing the polar coordinates (ρ, ϕ) with the origin in the center of the disk, namely such that $0 \leqslant \rho \leqslant R_\mathcal{Q}$ and $0 \leqslant \phi < 2\pi$. This disk can be mapped into the half plane $\{(x, y) \in \mathbb{R}^2, x \geqslant 0\}$ considered in section 2.2.1, as discussed in appendix A. In terms of the polar coordinates in the conformal boundary, the metric of $\mathbb{H}_3$ reads $ds^2 = (dz^2+d\rho^2+\rho^2 d\phi^2)/z^2$, being $z > 0$ the holographic coordinate.

JHEP08(2018)164

For a BCFT$_3$ defined in the above disk of radius $R_{\mathcal{Q}}$, the gravitational background dual to the ground state is a region of $\mathbb{H}_3$ delimited by a surface $\mathcal{Q}$ invariant under rotations about the z-axis, whose boundary is the circle $\mathcal{C}_{\mathcal{Q}}$ given by $(\rho, z) = (R_{\mathcal{Q}}, 0)$. When the term (2.2) occurs in the gravitational action (2.1), the profile of $\mathcal{Q}$ can be found as the image of the half plane (2.20) through the conformal map (A.3) described in appendix A. The result reads [68, 69]

$$\rho = \sqrt{(R_{\mathcal{Q}} \csc\alpha)^2 - (z - R_{\mathcal{Q}} \cot\alpha)^2} \tag{2.24}$$

(see also (A.4)), which corresponds to a spherical cap $\mathcal{Q}$ centered in $(\rho, z) = (0, R_{\mathcal{Q}} \cot\alpha)$ with radius $R_{\mathcal{Q}}/\sin\alpha$ (see the green surface in the left panel of figure 3). When $\alpha = \pi/2$, this spherical cap becomes the hemisphere $\rho^2 + z^2 = R_{\mathcal{Q}}^2$. By introducing the angular coordinate θ as $\tan\theta = z/\rho$, from (2.24) we find that the coordinates of a point of $\mathcal{Q}$ are $(\rho, z) = R_{\mathcal{Q}}\big(Q_\alpha(\theta), Q_\alpha(\theta)\tan\theta\big)$ with

$$Q_\alpha(\theta) \equiv \cos\theta \left(\cot\alpha \, \sin\theta + \sqrt{1 + (\cot\alpha \, \sin\theta)^2}\,\right) = \frac{\sqrt{\zeta^2 + (\sin\alpha)^2} + \zeta\cos\alpha}{(\zeta^2+1)\sin\alpha} \tag{2.25}$$

where in the last step we have introduced $\zeta \equiv \tan\theta$, that will be employed also in section 4.1.

In this AdS$_4$/BCFT$_3$ setup, F_A is given by (2.18) (or (2.19) whenever it can be applied). We remark that typically $\tilde{b}^z$ is not constant along $\partial\hat{\gamma}_{\mathcal{Q}}$. Instead, this simplification occurs when A is a disk sharing the origin with $\mathcal{C}_{\mathcal{Q}}$ (see the left panel of figure 3).

3 Infinite strip adjacent to the boundary

In this section we focus on the holographic entanglement entropy of infinite strips parallel to the flat boundary, in the AdS$_4$/BCFT$_3$ setup described in section 2.2.1. We show that the formula (2.23) reproduces the result for F_A computed in [72, 73, 86, 87] by means of a straightforward computation of the area for the corresponding minimal surfaces.

An infinite strip A of width ℓ adjacent to the boundary can be studied by taking the rectangular domain $(x, y) \in \mathbb{R}^2$ such that $0 \leqslant x \leqslant \ell$ and $-L_\parallel/2 \leqslant y \leqslant L_\parallel/2$ in the regime of $L_\parallel \gg \ell \gg \varepsilon$. In this limit, the invariance under translations in the y direction can be assumed. The corresponding minimal surfaces $\hat{\gamma}_A$ have been studied in [87] in the whole regime of $\alpha \in (0, \pi)$, by employing the partial results previously obtained in [72, 73, 86].

The minimal surface $\hat{\gamma}_A$ intersects the $z = 0$ half plane orthogonally along the line $x = \ell$, which is a component of $\partial\hat{\gamma}_A$. In this case $P_{A,B} = L_\parallel$ in (2.11), therefore the leading linear divergence (area law term) in the expansion of $\mathcal{A}[\hat{\gamma}_\varepsilon]$ as $\varepsilon \to 0$ is $L_\parallel/\varepsilon$. We are mainly interested in the subleading term F_A, which depends on the entire surface. Because of the invariance under translations in the y direction, $\hat{\gamma}_A$ is characterised by its section at $y = \text{const}$.

When $\alpha \leqslant \pi/2$, two surfaces $\hat{\gamma}_A^{\text{dis}}$ and $\hat{\gamma}_A^{\text{con}}$ extremise the area functional (see the left panel in figure 2); therefore their areas must be compared to find the global minimum [72, 73, 87]. The surface $\hat{\gamma}_A^{\text{dis}}$ is the half plane $x = \ell$ (the purple half plane in figure 2), which remains orthogonal to the $z = 0$ plane and does not intersect $\mathcal{Q}$ at a finite value of z.

JHEP08(2018)164

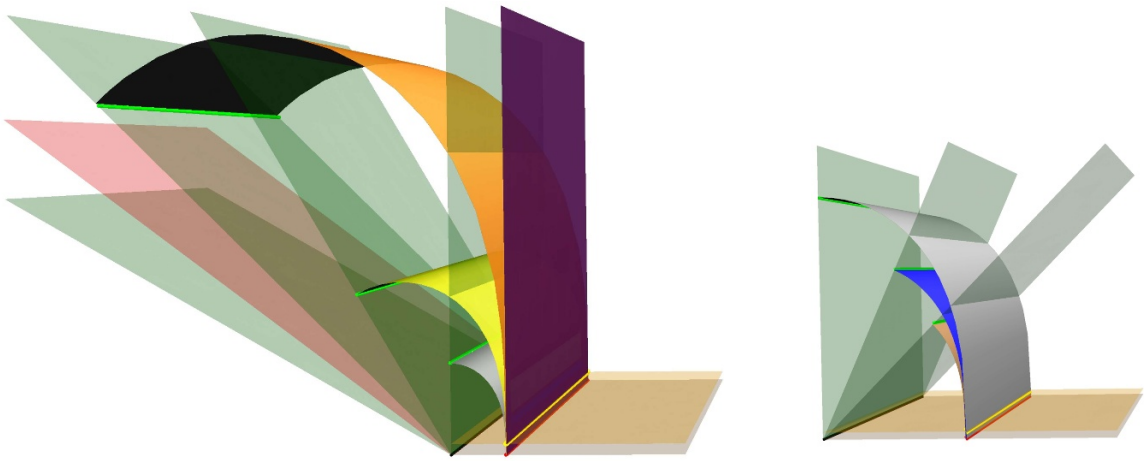

Figure 2. Minimal area surfaces corresponding to the same infinite strip A in the $z = 0$ half plane (the grey half plane) which is adjacent to the boundary $x = 0$ (straight solid black line). The entangling curve is the straight solid red line. The yellow horizontal plane is given by $z = \varepsilon$. The green half planes correspond to $\mathcal{Q}$ in (2.20) for different values of α and the red half plane is $\mathcal{Q}$ with $\alpha = \alpha_c$. For $\alpha > \alpha_c$ we show $\hat{\gamma}_A^{\rm con}$ and $\partial\hat{\gamma}_{\mathcal{Q}} = \hat{\gamma}_A^{\rm con} \cap \mathcal{Q}$ are highlighted (green straight lines). The vertical purple half plane corresponds to $\hat{\gamma}_A^{\rm dis}$. In the left panel $0 < \alpha \leqslant \pi/2$ and in the right panel $\pi/2 \leqslant \alpha < \pi$.

Instead, the surface $\hat{\gamma}_A^{\rm con}$ intersects the half plane $\mathcal{Q}$ orthogonally at a finite value z_* of the coordinate z. When $\alpha > \pi/2$ (see the right panel in figure 2), the solution $\hat{\gamma}_A^{\rm dis}$ does not exist; hence the global minimum is given by $\hat{\gamma}_A^{\rm con}$.

The extremal surface $\hat{\gamma}_A^{\rm con}$ for a given $\alpha \in (0, \pi)$ is characterised by the following profile [87]

$$P_\theta = \big(x(\theta)\,, z(\theta)\big) = \frac{\ell}{\mathfrak{g}(\alpha)} \left(\mathbb{E}\big(\pi/4 - \alpha/2\,|\,2\big) - \frac{\cos\alpha}{\sqrt{\sin\alpha}} + \mathbb{E}\big(\pi/4 - \theta/2\,|\,2\big)\,,\, \sqrt{\sin\theta} \right) \tag{3.1}$$

where $\theta \in [0, \pi - \alpha]$ is the angular parameter such that $\theta = 0$ corresponds to $z = 0$ and

$$\mathfrak{g}(\alpha) \equiv \mathbb{E}\big(\pi/4 - \alpha/2\,|\,2\big) - \frac{\cos\alpha}{\sqrt{\sin\alpha}} + \frac{\Gamma\big(\frac{3}{4}\big)^2}{\sqrt{2\pi}} \tag{3.2}$$

being $\mathbb{E}(x|y)$ the incomplete elliptic integral of the second kind (we adopt the convention of Mathematica for the elliptic function throughout this manuscript). From (3.1) we can easily obtain $z_* = z(\pi - \alpha)$ given by

$$z_* = \frac{\sqrt{\sin\alpha}}{\mathfrak{g}(\alpha)}\,\ell \tag{3.3}$$

which characterises the position of the straight green lines corresponding to $\hat{\gamma}_A^{\rm con} \cap \mathcal{Q}$ in figure 2. Since we must have $z_* > 0$, from (3.3) one observes that $\hat{\gamma}_A^{\rm con}$ is well defined when $\mathfrak{g}(\alpha) > 0$. It is straightforward to notice that $\mathfrak{g}(\alpha)$ has only one zero for $\alpha \in (0, \pi)$ given by $\alpha_c \simeq \pi/4.85$. Thus, when $\alpha \leqslant \alpha_c$ the solution $\hat{\gamma}_A^{\rm con}$ does not exist and the global minimum is $\hat{\gamma}_A^{\rm dis}$ (the purple half plane in figure 2), as discussed in [72, 73, 87].

JHEP08(2018)164

The $O(1)$ term in the expansion of $\mathcal{A}[\hat{\gamma}_\varepsilon]$ as $\varepsilon \to 0$ for $\alpha \in (0,\pi)$ reads [87]

$$F_A = L_\parallel \frac{a_0(\alpha)}{\ell} \qquad a_0(\alpha) = \begin{cases} -\mathfrak{g}(\alpha)^2 & \alpha \geqslant \alpha_c \\ 0 & \alpha \leqslant \alpha_c \end{cases} \tag{3.4}$$

The main observation of this section is that the non trivial expression for F_A corresponding to the regime $\alpha \geqslant \alpha_c$ in (3.4) can be recovered by evaluating (2.23) for $\hat{\gamma}_A^{\text{con}}$ as surface embedded in $\mathbb{R}^3$. The surface $\hat{\gamma}_A^{\text{con}}$ is described by the constraint $\mathcal{C} = 0$, being $\mathcal{C} \equiv z - z(x)$, and its unit normal vector $\tilde{n}_\mu = (\tilde{n}_z, \tilde{n}_x, \tilde{n}_y)$ can be found by first computing $\partial_\mu \mathcal{C}$ and then normalising the resulting vector. We find $\tilde{n}_\mu = (1, -z', 0)/\sqrt{1+(z')^2}$. The area element in the surface integral occurring in (2.23) reads $d\tilde{\mathcal{A}} = \sqrt{1+(z')^2}\, dx\, dy$ in this case. Combining these observations, we get

$$\int_{\hat{\gamma}_A} \frac{(\tilde{n}^z)^2}{z^2}\, d\tilde{\mathcal{A}} = \int_{\hat{\gamma}_A} \frac{dx\, dy}{z^2 \sqrt{1+(z')^2}} \tag{3.5}$$

where we have not used yet the fact that $z(x)$ corresponds to $\hat{\gamma}_A$. Specifying (3.5) to the profile (3.1), we find $\sqrt{1+(z')^2} = 1/\sin\theta$ and $dx = \ell\sqrt{\sin\theta}\, d\theta/(2\mathfrak{g}(\alpha))$. By employing these observations, (3.5) becomes

$$\int_{\hat{\gamma}_A} \frac{(\tilde{n}^z)^2}{z^2}\, d\tilde{\mathcal{A}} = L_\parallel \frac{2\mathfrak{g}(\alpha)}{\ell} \int_0^{\pi-\alpha} \sqrt{\sin\theta}\, d\theta = L_\parallel \frac{\mathfrak{g}(\alpha)}{\ell} \left(\mathbb{E}\big(\pi/4 - \alpha/2 \,|\, 2\big) + \frac{\Gamma(\frac{3}{4})^2}{\sqrt{2\pi}} \right) \tag{3.6}$$

The integral over the line $\partial\hat{\gamma}_\mathcal{Q}$ in (2.23) significantly simplifies for these domains because $\partial\hat{\gamma}_\mathcal{Q}$ is the straight line given by $(z, x, y) = (z_*, x_*, y)$ with $-L_\parallel/2 \leqslant y \leqslant L_\parallel/2$, where $(x_*, z_*) = P_{\pi-\alpha}$ can be read from (3.1) and it corresponds to the green straight lines in figure 2. Thus, the line integral in (2.23) gives

$$\int_{\partial\hat{\gamma}_\mathcal{Q}} \frac{1}{z}\, d\tilde{s} = \frac{L_\parallel}{z_*} = \frac{\mathfrak{g}(\alpha)}{\ell\sqrt{\sin\alpha}} L_\parallel \tag{3.7}$$

where (3.3) has been used in the last step.

Plugging (3.6) and (3.7) into the general expression (2.23), for an infinite strip of width ℓ adjacent to the boundary we find

$$F_A\big|_{\hat{\gamma}_A^{\text{con}}} = L_\parallel \frac{\mathfrak{g}(\alpha)}{\ell} \left[\left(\mathbb{E}\big(\pi/4 - \alpha/2 \,|\, 2\big) + \frac{\Gamma(\frac{3}{4})^2}{\sqrt{2\pi}} \right) - \frac{\cos\alpha}{\sqrt{\sin\alpha}} \right] = L_\parallel \frac{\mathfrak{g}(\alpha)^2}{\ell} \tag{3.8}$$

where the last result has been obtained by employing (3.2). Notice that both the terms in (2.23) provide non trivial contributions.

From the results discussed in this section, it is straightforward to find F_A when A is an infinite strip parallel to the flat boundary and at a finite distance from it through the formula (2.23), recovering the result presented in section 5.3 of [87]. In the analysis of this configuration, we find it instructive to employ the extremal surfaces anchored to two infinite parallel strips in the plane [95] as discussed in appendix D.

JHEP08(2018)164

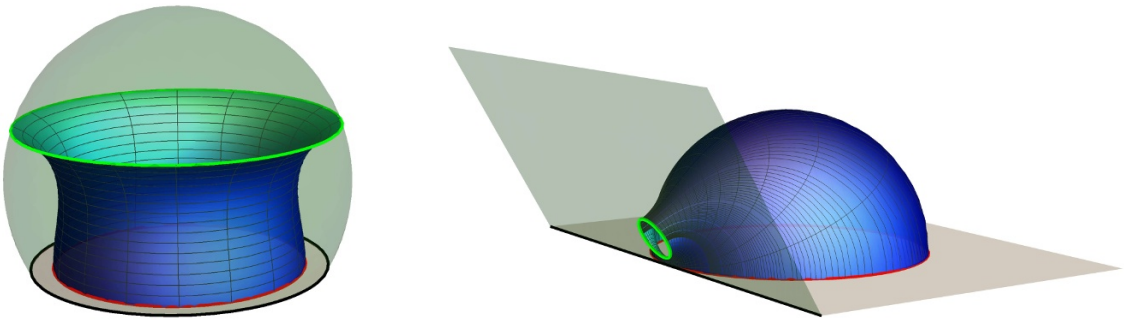

Figure 3. Left: extremal area surface $\hat{\gamma}_A^{\text{con}}$ anchored to a disk A disjoint from a circular concentric boundary (see section 2.2.2 and section 4.1) where $\mathcal{Q}$ (green spherical dome) is described by (2.24). Here $\alpha = \pi/3$ and $R_\circ/R_\mathcal{Q} \sim 0.85$, which corresponds to $r_{\circ,\,\text{min}}$ (see section 4.1.1). Right: extremal surface $\hat{\gamma}_A^{\text{con}}$ anchored to a disk disjoint from a flat boundary (see section 2.2.1 and section 4.2). Here $\alpha = \pi/3$ and d/R can be obtained from the first expression in (4.22) with the value of $R_\circ/R_\mathcal{Q}$ of the left panel because the two configurations shown in these panels are related through (A.3).

4 Disk disjoint from the boundary

In this section we study the holographic entanglement entropy of a disk A at a finite distance from the boundary.

In the setup described in section 2.2.2, in section 4.1 we consider the case of a disk A concentric to the circular boundary because the symmetry of this configuration allows us to obtain an analytic expression for the profile characterising the minimal surface $\hat{\gamma}_A$ (in the left panel of figure 3 we show an example of $\hat{\gamma}_A$). The corresponding area $\mathcal{A}[\hat{\gamma}_\varepsilon]$ is computed in two ways: by the direct evaluation of the integral and by specifying the general formula (2.23) to this case. In section 4.2, by employing the second transformation in (A.3) and the analytic results presented in section 4.1, we study the holographic entanglement entropy of a disk disjoint from the flat boundary in the setup introduced in section 2.2.1 (see the right panel of figure 3 for an example of $\hat{\gamma}_A$ in this setup). The two configurations in figure 3 have the same α and are related through the map (A.3) discussed in appendix A.

4.1 Disk disjoint from a circular concentric boundary

In the $\text{AdS}_4/\text{BCFT}_3$ setup introduced in section 2.2.2, let us consider a disk A with radius $R_\circ < R_\mathcal{Q}$ which is concentric to the boundary of the spatial slice of the spacetime. In section 4.1.1 we obtain an analytic expression for the profile characterising $\hat{\gamma}_A$ and in section 4.1.2 we evaluate the corresponding area $\mathcal{A}[\hat{\gamma}_\varepsilon]$. In the following we report only the main results of this analysis. Their detailed derivation, which is closely related to the evaluation of the holographic entanglement entropy of an annulus in $\text{AdS}_4/\text{CFT}_3$ [45, 96–99] has been presented in appendix B.

4.1.1 Profile of the extremal surfaces

Adopting the coordinate system (ρ, ϕ, z) introduced in section 2.2.2, the invariance under rotations around the z-axis for this configuration in the $z = 0$ plane implies that the local extrema of the area functional are described by the profiles of their sections at $\phi = \text{const}$.

JHEP08(2018)164

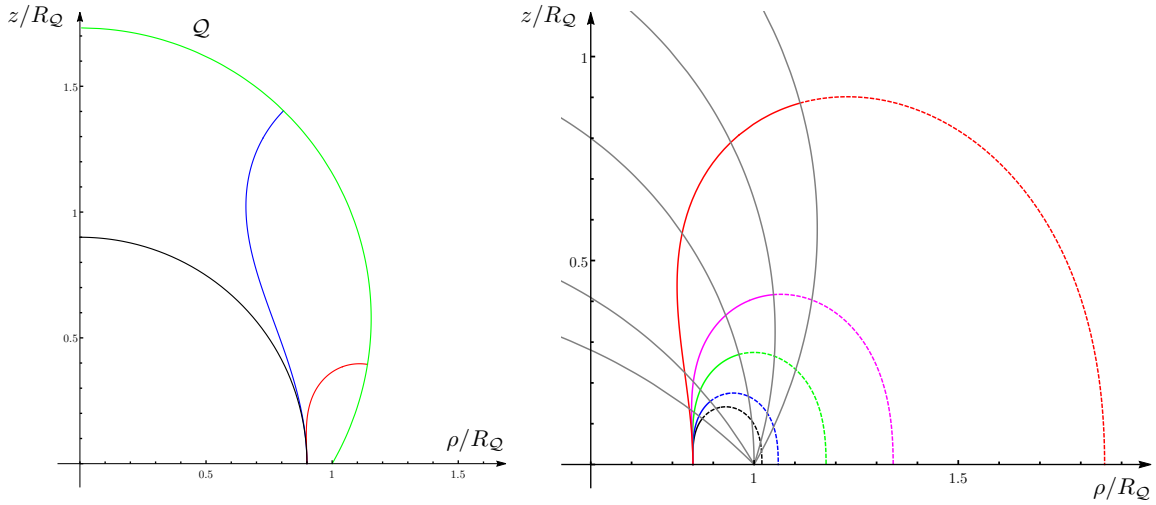

Figure 4. Sections of the extremal surfaces anchored to a disk A of radius $R_\circ$ disjoint from a circular concentric boundary with radius $R_{\mathcal{Q}}$ (see section 4.1.1). Left: profiles corresponding to the three extremal surfaces in the case of $R_\circ/R_{\mathcal{Q}} = 0.9$ and $\alpha = \pi/3$. The green curve represents $\mathcal{Q}$. The black curve corresponds to $\hat{\gamma}_A^{\rm dis}$ (the hemisphere). The red curve and the blue curve correspond to $\hat{\gamma}_A^{\rm con}$ and they have been obtained through the analytic results discussed in section 4.1.1 and in appendix B. The red curve provides the global minimum in this case. Right: extremal surfaces $\hat{\gamma}_A^{\rm con}$ having $R_\circ/R_{\mathcal{Q}} \simeq 0.85$ for different values of α: $\alpha = \pi/3$ (red), $\alpha = \pi/2.5$ (magenta), $\alpha = \pi/2$ (green), $\alpha = 2\pi/3$ (blue) and $\alpha = 3\pi/4$ (black). The dashed curves are the profiles of the auxiliary surfaces $\hat{\gamma}_{A,\,\rm aux}^{\rm con}$, with the same color code. All the profiles correspond to the smaller value of k whenever two surfaces $\hat{\gamma}_A^{\rm con}$ exists. All the curves except for the red one provide the global minimum of the corresponding configuration.

For a given A, an extremal surface is the hemisphere anchored to the circle ∂A. Since it does not intersect $\mathcal{Q}$, this solution will be denoted by $\hat{\gamma}_A^{\rm dis}$, while we will refer to the extremal surfaces that intersect $\mathcal{Q}$ orthogonally as $\hat{\gamma}_A^{\rm con}$. The holographic entanglement entropy of A is provided by the surface corresponding to the global minimum of the area. Let us anticipate that we find at most two solutions $\hat{\gamma}_A^{\rm con}$; hence we have at most three local extrema for a given disk A. The number of solutions depends on the value of α, as we will discuss in the following. By employing the analytic result that will be presented below, in the left panel of figure 4 we show the three profiles corresponding to $\hat{\gamma}_A^{\rm dis}$ (black curve) and $\hat{\gamma}_A^{\rm con}$ (blue and red curve) in an explicit case. The red curve provides the holographic entanglement entropy in this example.

We find it worth introducing an auxiliary surface that allows to relate our problem to the one of finding the extremal surfaces in $\mathbb{H}_3$ anchored to an annulus, which has been already addressed in the literature. Given $\hat{\gamma}_A^{\rm con}$, let us consider its unique surface $\hat{\gamma}_{A,\,\rm aux}^{\rm con}$ in the whole $\mathbb{H}_3$ such that $\hat{\gamma}_A^{\rm con} \cup \hat{\gamma}_{A,\,\rm aux}^{\rm con}$ is an extremal area surface in $\mathbb{H}_3$ anchored to the annulus whose boundary is made by the two concentric circles with radii $R_\circ$ and $R_{\rm aux} > R_\circ$. Thus, $\hat{\gamma}_A^{\rm con}$ can be viewed as part of an extremal surface anchored to a proper annulus whose boundary are the union of two circles, one of which is ∂A. By using the solution that will be discussed in the following, in the right panel of figure 4 we fix A and we show the profiles

JHEP08(2018)164

associated to $\hat{\gamma}_A^{\text{con}}$ (solid curves) for various α and the ones for the corresponding extensions $\hat{\gamma}_{A,\,\text{aux}}^{\text{con}}$ (dashed curves). Other examples are shown in figure 6.

The profile of a section of $\hat{\gamma}_A^{\text{con}}$ at fixed ϕ can be written as $(\rho, z) = (\rho_\gamma(\theta), \rho_\gamma(\theta)\tan\theta)$, where the angular variable is defined as $\zeta \equiv \tan\theta = z/\rho$ (see section 2.2.2). Considering the construction of the extremal surfaces in $\mathbb{H}_3$ anchored to an annulus reported in [45], we have that the curve $\rho_\gamma(\theta)$ can be written by introducing two branches as follows

$$\rho_\gamma(\theta) = \begin{cases} R_\circ\, e^{-q_{-,k}(\zeta)} \\ R_{\text{aux}}\, e^{-q_{+,k}(\zeta)} \end{cases} \tag{4.1}$$

with $R_{\text{aux}} > R_\circ$. The functions $q_{\pm,k}(\zeta)$ are defined as

$$q_{\pm,k}(\zeta) \equiv \int_0^\zeta \frac{\lambda}{1+\lambda^2}\left(1 \pm \frac{\lambda}{\sqrt{k\,(1+\lambda^2)-\lambda^4}}\right) d\lambda \qquad\qquad 0 \leqslant \zeta \leqslant \zeta_m \tag{4.2}$$

being $k > 0$ and $\zeta_m^2 \equiv \big(k + \sqrt{k(k+4)}\,\big)/2$ the unique admissible root of the biquadratic equation coming from the expression under the square root in (4.2). Since $q_{\pm,k}(0) = 0$, the two branches in (4.1) give $\rho_\gamma = R_\circ$ and $\rho_\gamma = R_{\text{aux}}$ when $z = 0$.

The two branches characterised by $q_{\pm,k}(\zeta)$ in (4.1) match at the point $P_m = (\rho_m, \zeta_m)$ associated to the maximum value of θ. The coordinates of P_m read (see also appendix B)

$$\zeta_m^2 = \frac{k + \sqrt{k(k+4)}}{2} \qquad\qquad \rho_m = R_\circ\, e^{-q_{-,k}(\zeta_m)} = R_{\text{aux}}\, e^{-q_{+,k}(\zeta_m)} \tag{4.3}$$

The last equality in the second expression follows from the continuity of the profile (4.1) and it gives

$$\frac{R_\circ}{R_{\text{aux}}} = e^{q_{-,k}(\zeta_m) - q_{+,k}(\zeta_m)} \tag{4.4}$$

which will be denoted by $\chi(\zeta_m)$ in the following. Being ζ_m given by the first expression in (4.3), from (4.4) we observe that the ratio $R_\circ/R_{\text{aux}}$ is a function of the parameter $k > 0$. Moreover, by employing (4.2) in (4.4), it is straightforward to observe that $R_\circ/R_{\text{aux}} < 1$.

The integral in (4.2) can be computed analytically, finding that $q_{\pm,k}(\zeta)$ can be written in terms of the incomplete elliptic integrals of the first and third kind as follows

$$q_{\pm,k}(\zeta) = \frac{1}{2}\log(1+\zeta^2) \pm \kappa\sqrt{\frac{1-2\kappa^2}{\kappa^2-1}}\,\Big[\,\Pi\big(1-\kappa^2, \Omega(\zeta)|\kappa^2\big) - \mathbb{F}\big(\Omega(\zeta)|\kappa^2\big)\Big] \tag{4.5}$$

where

$$\Omega(\zeta) \equiv \arcsin\left(\frac{\zeta/\zeta_m}{\sqrt{1+\kappa^2(\zeta^2/\zeta_m^2-1)}}\right) \qquad \kappa \equiv \sqrt{\frac{1+\zeta_m^2}{2+\zeta_m^2}} \tag{4.6}$$

Let us remark that the above expressions depend on the positive parameters $R_\circ$ and k. The dependence on the parameters $R_{\mathcal{Q}}$ and α characterising the boundary occurs through the requirement that $\hat{\gamma}_A^{\text{con}} \perp \mathcal{Q}$.

Denoting by $P_* = (\rho_*, z_*)$ the point in the radial profile corresponding to the intersection between $\hat{\gamma}_A^{\text{con}}$ and $\mathcal{Q}$, in appendix B we have found that

$$\zeta_*^2 = \frac{k + \sqrt{k(k+4(\sin\alpha)^2)}}{2} \qquad\qquad \rho_* = R_{\mathcal{Q}}\,\frac{\sqrt{\zeta_*^2 + (\sin\alpha)^2} + \zeta_*\cos\alpha}{(\zeta_*^2+1)\sin\alpha} \tag{4.7}$$

JHEP08(2018)164

where the first expression has been obtained by imposing that $\hat{\gamma}_A^{\text{con}}$ intersects $\mathcal{Q}$ orthogonally at P_*, while the second one comes from (2.25). In appendix B.1 (see below (B.12)) we have also remarked that the orthogonality condition also implies that P_* belongs to the branch described $q_{-,k}$ when $\alpha \geqslant \pi/2$, while it belongs to the branch characterised by $q_{+,k}$ when $\alpha \leqslant \pi/2$. This observation and (4.1) specialised to P_* lead to

$$R_\circ = \rho_* \left(\frac{1+\eta_\alpha}{2}\, e^{q_{-,k}(\zeta_*)} + \frac{1-\eta_\alpha}{2}\, \chi(\zeta_m)\, e^{q_{+,k}(\zeta_*)} \right) \tag{4.8}$$

where $\eta_\alpha \equiv -\operatorname{sign}(\cot\alpha)$ and $\chi(\zeta_m)$ denotes the ratio in (4.4).

Notice that $e^{q_{-,k}(\zeta_*)} = \chi(\zeta_m)\, e^{q_{+,k}(\zeta_*)}$ for $\alpha = \pi/2$. Moreover, if we employ this observation into the second expression of (4.3), we find that $P_* = P_m$ when $\alpha = \pi/2$.

By using the expression of ρ_* in (4.7) into (4.8), we get the following relation

$$\frac{R_\circ}{R_\mathcal{Q}} = \frac{\sqrt{\zeta_*^2 + (\sin\alpha)^2} + \zeta_* \cos\alpha}{(\zeta_*^2+1)\sin\alpha} \left(\frac{1+\eta_\alpha}{2}\, e^{q_{-,k}(\zeta_*)} + \frac{1-\eta_\alpha}{2}\, \chi(\zeta_m)\, e^{q_{+,k}(\zeta_*)} \right) \tag{4.9}$$

where ζ_* is the function of k and α given by the first formula in (4.7). The expression (4.9) tells us that $R_\circ/R_\mathcal{Q}$ is a function of k and α. In figure 5 we plot this function by employing $\sqrt[4]{k}$ as the independent variable and α as parameter. Since the disk A is a spatial subsystem of the disk with radius $R_\mathcal{Q}$, the admissible configurations have $R_\circ/R_\mathcal{Q} < 1$.

We find it worth discussing the behaviour of the curves $R_\circ/R_\mathcal{Q}$ in (4.9) parameterised by α in the limiting regimes given by $k \to 0$ and $k \to \infty$. The technical details of this analysis have been reported in appendix B.3.

The expansion of (4.9) for small k reads

$$\frac{R_\circ}{R_\mathcal{Q}} = 1 - \mathfrak{g}(\alpha)\, \sqrt[4]{k} + \frac{\mathfrak{g}(\alpha)^2}{2}\, \sqrt{k} + o\big(\sqrt{k}\,\big) \tag{4.10}$$

where $\mathfrak{g}(\alpha)$ has been defined in (3.2). Since $\mathfrak{g}(\alpha) > 0$ only for $\alpha > \alpha_c$, being α_c the unique zero of $\mathfrak{g}(\alpha)$ introduced in section 3, the expansion (4.10) tells us that, in the regime of small k, an extremal surface $\hat{\gamma}_A^{\text{con}}$ can be found only when $\alpha > \alpha_c$ because $R_\circ/R_\mathcal{Q} < 1$. From figure 5 we notice that this observation can be extended to the entire regime of k. Indeed, since $R_\circ/R_\mathcal{Q} \geqslant 1$ for the curves with $\alpha \leqslant \alpha_c$, we have that $\hat{\gamma}_A^{\text{con}}$ does not exist in this range of α.

In appendix B.3 also the limit of (4.9) for large k has been discussed, finding that for any $\alpha \in (0,\pi)$ it reads

$$\lim_{k\to\infty} \frac{R_\circ}{R_\mathcal{Q}} = \cot(\alpha/2) \tag{4.11}$$

which gives the asymptotic value of the curves in figure 5 for large k.

When $\alpha > \alpha_c$ the curve $R_\circ/R_\mathcal{Q}$ has only one local minimum (see figure 5). Denoting by $k_{\circ,\min}$ and $r_{\circ,\min}$ the values of k and $R_\circ/R_\mathcal{Q}$ characterising this point, we have that $r_{\circ,\min} < \cot(\alpha/2)$. The plot of $r_{\circ,\min}$ in terms of $\alpha > \alpha_c$ has been reported in figure 8 (black solid curve) where $\cot(\alpha/2)$ corresponds to the dashed blue curve.

These observations about the limits of $R_\circ/R_\mathcal{Q}$ and the numerical analysis of figure 5 allow to discuss the number of extremal surfaces $\hat{\gamma}_A^{\text{con}}$ in the various regimes of the parameters. When $\alpha \leqslant \alpha_c$ the solutions $\hat{\gamma}_A^{\text{con}}$ do not exist because $R_\circ/R_\mathcal{Q} \geqslant 1$. When $\alpha > \alpha_c$ also

JHEP08(2018)164

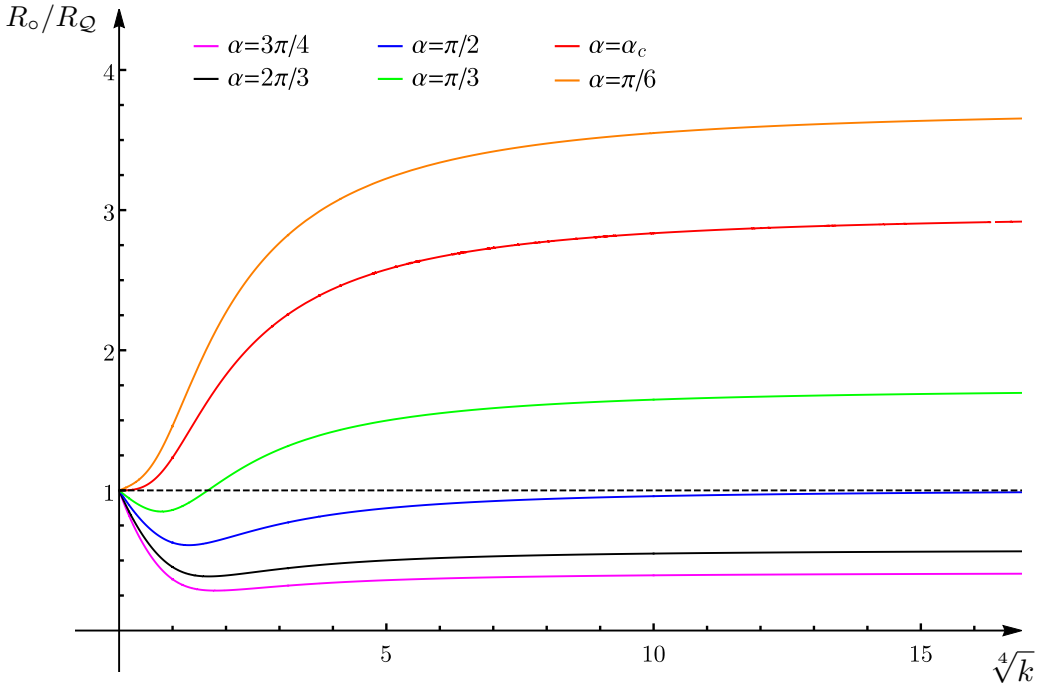

Figure 5. The ratio $R_\circ/R_\mathcal{Q}$ providing $\hat{\gamma}_A^{\rm con}$ as a function of $\sqrt[4]{k}$ from (4.9) for different values of α. The allowed configurations have $R_\circ/R_\mathcal{Q} < 1$ and the black dashed line corresponds to the limiting value $R_\circ/R_\mathcal{Q} = 1$. The asymptotic behaviours of these curves for $k \to 0$ and $k \to \infty$ are given by (4.10) and (4.11) respectively. For fixed values of $\alpha > \alpha_c$ and $R_\circ/R_\mathcal{Q} < 1$, the number of extremal solutions $\hat{\gamma}_A^{\rm con}$ is given by the number of intersections between the curve corresponding to α and the horizontal line characterised by the given value of $R_\circ/R_\mathcal{Q}$.

the global minimum $r_{\circ,\,\rm min}$ of $R_\circ/R_\mathcal{Q}$ is an important parameter to consider. Indeed, for $\alpha_c < \alpha \leqslant \pi/2$ (see e.g. the green curve in figure 5) one has two distinct extremal surfaces $\hat{\gamma}_A^{\rm con}$ when $r_{\circ,\,\rm min} < R_\circ/R_\mathcal{Q} < 1$, one extremal surface when $R_\circ/R_\mathcal{Q} = r_{\circ,\,\rm min}$ and none of them when $R_\circ/R_\mathcal{Q} < r_{\circ,\,\rm min}$. For $\alpha > \pi/2$ also the asymptotic value (4.11) plays an important role. Indeed, when $\cot(\alpha/2) \leqslant R_\circ/R_\mathcal{Q} < 1$ we can find only one extremal surface $\hat{\gamma}_A^{\rm con}$, when $r_{\circ,\,\rm min} < R_\circ/R_\mathcal{Q} < \cot(\alpha/2)$ there are two solutions $\hat{\gamma}_A^{\rm con}$, when $r_{\circ,\,\rm min} = R_\circ/R_\mathcal{Q}$ we have again only one solution, while $\hat{\gamma}_A^{\rm con}$ do not exist when $R_\circ/R_\mathcal{Q} < r_{\circ,\,\rm min}$. Whenever two distinct solutions $\hat{\gamma}_A^{\rm con}$ can be found, considering their values $k_1 < k_2$ for the parameter k, we have that $k_1 < k_{\circ,\,\rm min} < k_2$ because $R_\circ/R_\mathcal{Q}$ has at most one local minimum for $k > 0$.

As for the extremal surface $\hat{\gamma}_A^{\rm dis}$, which does not intersect $\mathcal{Q}$, its existence depends on the value of α because the condition that $\hat{\gamma}_A^{\rm dis}$ does not intersect $\mathcal{Q}$ provides a non trivial constraint when $\alpha < \pi/2$. In order to write this constraint, one first evaluates the z coordinate $z_\mathcal{Q}$ of the tip of $\mathcal{Q}$ by setting $\rho = 0$ in (2.24), finding that $z_\mathcal{Q}/R_\mathcal{Q} = \cot(\alpha/2)$. Then, being $\hat{\gamma}_A^{\rm dis}$ a hemisphere, we must impose that $R_\circ \leqslant z_\mathcal{Q}$ and this leads to $R_\circ/R_\mathcal{Q} \leqslant \cot(\alpha/2)$.

Focusing on the regimes where at least one extremal surface $\hat{\gamma}_A^{\rm con}$ exists and employing the above observations, we can plot the profile given by the section of $\hat{\gamma}_A^{\rm con}$ at $\phi = {\rm const}$ by using (4.1) and the related expressions. In figure 6 we show some radial profiles of $\hat{\gamma}_A^{\rm con}$

JHEP08(2018)164

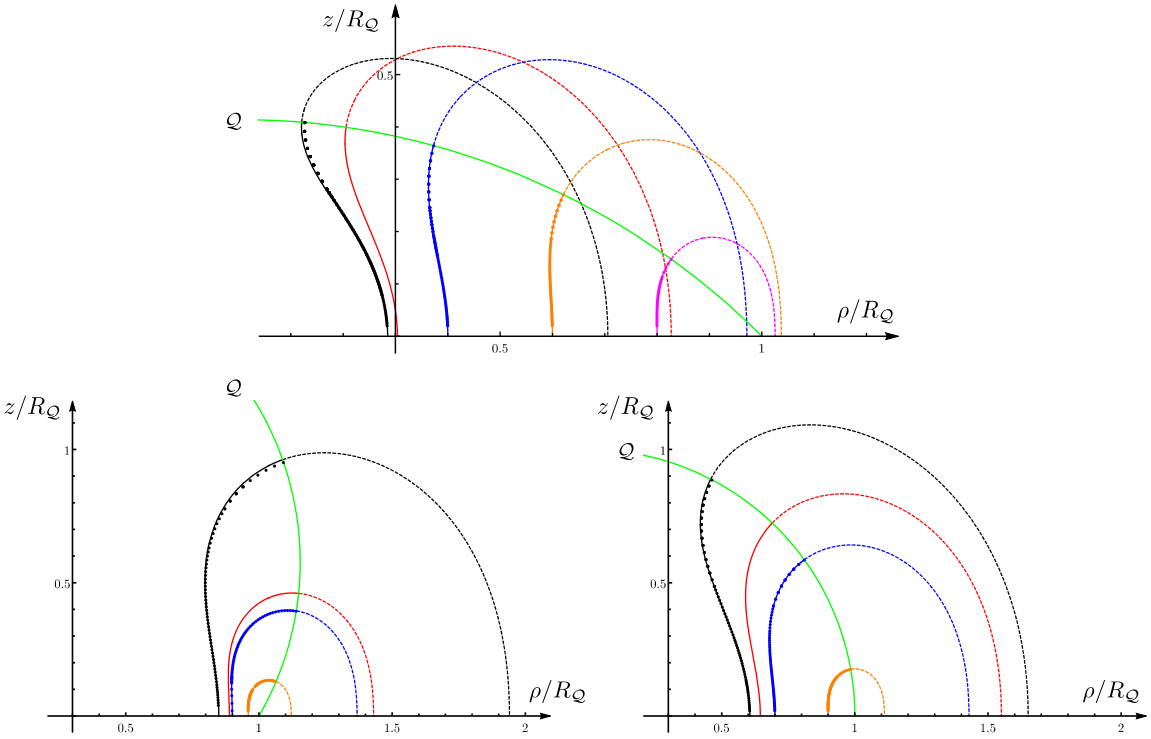

Figure 6. Radial profiles of extremal surfaces $\hat{\gamma}_A^{\rm con}$ intersecting $\mathcal{Q}$ (green curve) orthogonally and anchored to a disk A of radius $R_\circ$ concentric to a circular boundary with radius $R_{\mathcal{Q}}$ (see section 4.1.1). The value of α in the three panels is $\alpha = 3\pi/4$ (top), $\alpha = \pi/2$ (bottom, right) and $\alpha = \pi/3$ (bottom, left). The solid lines give $\hat{\gamma}_A^{\rm con}$, while the dashed ones (with the same colour) give the corresponding auxiliary surface $\hat{\gamma}_{A,\,\rm aux}^{\rm con}$. The value of k associated to all the shown profiles is the minimum one, whenever two solutions occur (see figure 5). All the profiles except for the black one correspond to the global minimum. The red curves correspond to the critical value of the ratio $R_\circ/R_{\mathcal{Q}}$ where the area of the extremal surface $\hat{\gamma}_A^{\rm dis}$ is equal to the minimum of the area of the extremal surfaces $\hat{\gamma}_A^{\rm con}$. The points have been found by taking the ϕ = const section of the extremal surfaces constructed by Surface Evolver and they nicely agree with the corresponding analytic solutions.

(solid lines) and of the corresponding auxiliary surfaces $\hat{\gamma}_{A,\,\rm aux}^{\rm con}$ (dashed lines) obtained from the analytic expressions discussed above. These analytic results have been also checked numerically by employing Surface Evolver as done in [42, 45, 87] for other configurations. The data points in figure 6 correspond to the ϕ = const section of the extremal surfaces obtained numerically with Surface Evolver. The nice agreement between the solid curves and the data points provides a highly non trivial check of our analytic results. We remark that Surface Evolver constructs also extremal surfaces that are not the global minimum corresponding to a given configuration.

A detailed discussion about the position of the auxiliary circle with respect to the circular boundary has been reported in appendix D. Here let us notice that in the top panel, where $\alpha = 3\pi/4$, for the black curve and the blue curve we have $R_{\rm aux} < R_{\mathcal{Q}}$.

In the above analysis we have considered the case of a disk concentric to a circular boundary. Nonetheless, we can also study the case of a disk whose center does not coincide

JHEP08(2018)164

with the center of the circular boundary by combining the analytic expressions obtained for this configuration and the mapping discussed in appendix A.

4.1.2 Area

Given a configuration characterised by a disk A of radius $R_\circ < R_\mathcal{Q}$ concentric to the spatial disk of radius $R_\mathcal{Q}$ and the value α for $\mathcal{Q}$, in section 4.1.1 we have seen that we can find at most three local extrema of the area functional among the surfaces anchored to A: the hemisphere $\hat{\gamma}_A^{\text{dis}}$ and at most two surfaces $\hat{\gamma}_A^{\text{con}} \perp \mathcal{Q}$. Since for these three surfaces the expansion of the regularised area is given by the r.h.s. of (1.4) with $P_{A,B} = P_A = 2\pi R_\circ$, the holographic entanglement entropy of A can be found by comparing their subleading terms F_A. Let us denote by F_{con} the subleading term for the surfaces intersecting $\mathcal{Q}$ orthogonally discussed in section 4.1.1. Since $F_A = 2\pi$ for the hemisphere [6, 7, 100], the holographic entanglement entropy of A is given by

$$\mathcal{A}[\hat{\gamma}_\varepsilon] = \frac{2\pi R_\circ}{\varepsilon} - \max\big(2\pi, \widehat{F}_{\text{con}}\big) + \mathcal{O}(\varepsilon) \tag{4.12}$$

where we have denoted by $\widehat{F}_{\text{con}}$ the maximum between the (at most) two values taken by F_{con} for the values of k corresponding to the local extrema $\hat{\gamma}_A^{\text{con}}$.

In appendix B.2, we have computed F_{con} by employing two methods: a straightforward evaluation of the integral coming from the area functional and the general expression (2.19) specialized to the extremal surfaces $\hat{\gamma}_A^{\text{con}}$ of these configurations. Both these approaches lead to the following result

$$F_{\text{con}} = 2\pi \left[\frac{1+\eta_\alpha}{2}\, \mathcal{F}_k(\zeta_*) + \frac{1-\eta_\alpha}{2} \Big(2\, \mathcal{F}_k(\zeta_m) - \mathcal{F}_k(\zeta_*) \Big) \right] \tag{4.13}$$

where

$$\mathcal{F}_k(\zeta) \equiv \frac{\sqrt{k(1+\zeta^2)-\zeta^4}}{\sqrt{k}\,\zeta} - \frac{\mathbb{F}(\arcsin(\zeta/\zeta_m)\,|\,-\zeta_m^2-1) - \mathbb{E}(\arcsin(\zeta/\zeta_m)\,|\,-\zeta_m^2-1)}{\zeta_m} \tag{4.14}$$

and we recall that ζ_m and ζ_* are the values of ζ corresponding to the points P_m and P_* respectively (see section 4.1.1). For $\zeta = \zeta_m$, we have

$$\mathcal{F}_k(\zeta_m) = \frac{\mathbb{E}(-\zeta_m^2-1) - \mathbb{K}(-\zeta_m^2-1)}{\zeta_m} \tag{4.15}$$

where $\mathbb{K}$ and $\mathbb{E}$ are the complete elliptic integral of the first and second kind respectively. Since ζ_m is a function of k (see (4.3)), the r.h.s. of (4.15) depends only on this parameter. Instead, since ζ_* depends on both k and α (see the first expression in (4.7)), we have that (4.13) defines a family of functions of k parameterised by $\alpha \in (0, \pi)$.

We find it worth discussing the limiting regimes of F_{con} in (4.13) for small and large values of k (the technical details of this analysis have been reported in appendix B.3).

In the limit $k \to 0$, which corresponds to $R_\circ \to R_\mathcal{Q}$ (see (4.10) and figure 5), the expansion of F_{con} reads

$$F_{\text{con}} = \frac{2\pi\, \mathfrak{g}(\alpha)}{\sqrt[4]{k}} + \frac{\pi}{2} \left(\frac{\cot\alpha}{\sqrt{\sin\alpha}} + \mathbb{F}\big(\pi/4 - \alpha/2\,|\,2\big) + \frac{\Gamma^2\left(\frac{1}{4}\right)}{4\sqrt{2\pi}} \right) \sqrt[4]{k} + o\big(\sqrt[4]{k}\big) \tag{4.16}$$

JHEP08(2018)164

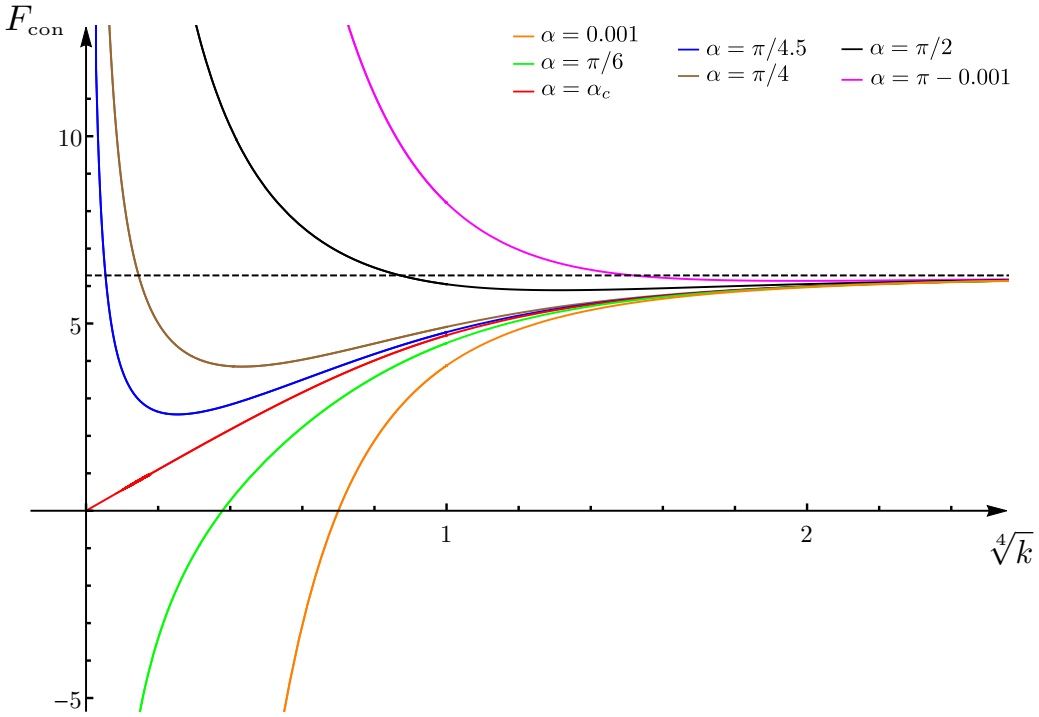

Figure 7. The subleading term $F_{\rm con}$ for the extremal surfaces $\hat{\gamma}_A^{\rm con}$ which intersect $\mathcal{Q}$ orthogonally as a function of $\sqrt[4]{k}$ (see (4.13)). The horizontal dashed line corresponds to 2π, i.e. the value of F_A for the hemisphere $\hat{\gamma}_A^{\rm dis}$, and it provides the asymptotic limit at large k for any value of α. The asymptotic behaviour for $k \to 0$ is given by (4.16). The curve with $\alpha = \alpha_c$ vanishes as $k \to 0$ and the slope of its tangent at $k = 0$ is given by the coefficient of the $O(\sqrt[4]{k}\,)$ term in (4.16). We numerically observe that, for $\alpha \geqslant \alpha_c$, the values of k corresponding to the local minima coincide with the values of k of the local minima in figure 5.

Since the coefficient of the leading term is positive when $\alpha > \alpha_c$, negative when $\alpha < \alpha_c$ and zero when $\alpha = \alpha_c$, different qualitative behaviours are observed when $k \to 0$. In particular, for $\alpha = \alpha_c$ the subleading term is $o(1)$; therefore $F_{\rm con} \to 0$.

By using (4.10), the expansion (4.16) can be written also as an expansion for $R_\circ/R_{\mathcal{Q}} \to 1$, finding that

$$F_{\rm con} = \frac{2\pi\, \mathfrak{g}(\alpha)^2}{1 - R_\circ/R_{\mathcal{Q}}} - \pi\, \mathfrak{g}(\alpha)^2 + \mathcal{O}(1 - R_\circ/R_{\mathcal{Q}}) \tag{4.17}$$

In the limit $k \to \infty$ we have seen that (4.11) and in appendix B.3 we find that $F_{\rm con} \to (2\pi)^-$ for every α.

In figure 7 we show $F_{\rm con}$ in terms of $\sqrt[4]{k}$ for different values of α. The horizontal dashed line corresponds to 2π, which is the value of the subleading term in the expansion of the area of the hemisphere $\hat{\gamma}_A^{\rm dis}$. This value provides the asymptotic limit of all the curves, confirming the result obtained in appendix B.3.

When $\alpha \leqslant \alpha_c$, from figure 7 we observe that $F_{\rm con} < 2\pi$ for all values of k. Since in section 4.1.1 we have shown that the local solutions $\hat{\gamma}_A^{\rm con}$ do not exist in this regime, the curves $F_{\rm con}$ having $\alpha \leqslant \alpha_c$ do not occur in the computation of holographic entanglement entropy. Thus, for $\alpha \leqslant \alpha_c$ the holographic entanglement entropy is given by $\hat{\gamma}_A^{\rm dis}$.

JHEP08(2018)164

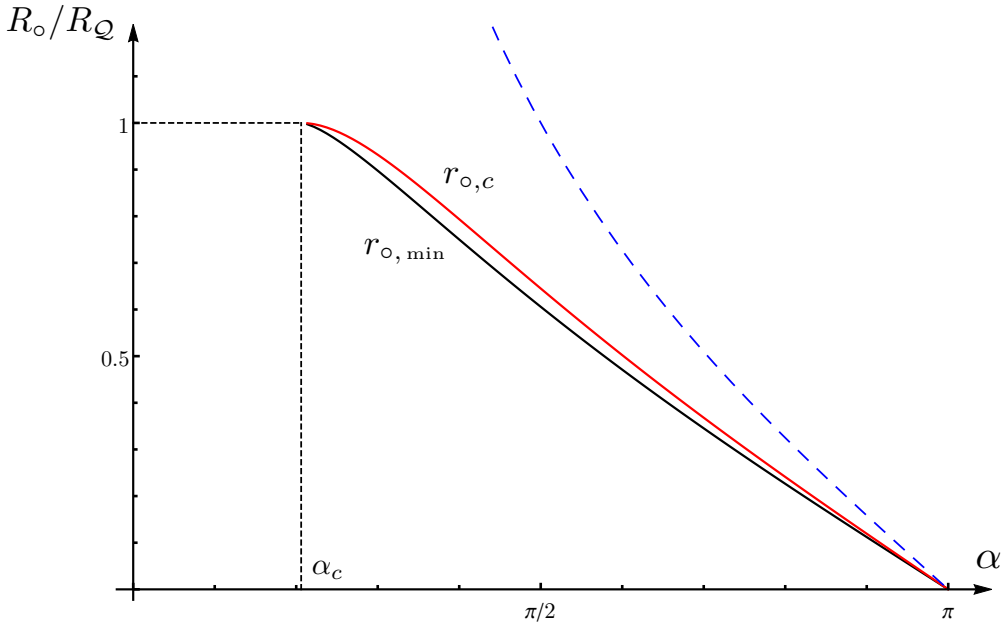

Figure 8. The solid black curve is the minimal value $r_{\circ,\,\mathrm{min}}$ of $R_\circ/R_\mathcal{Q}$, below which the local solutions $\hat{\gamma}_A^{\mathrm{con}}$ intersecting $\mathcal{Q}$ orthogonally do not exist (see also figure 5), in terms of $\alpha > \alpha_c$. The solid red curve gives the value $r_{\circ,c} > r_{\circ,\,\mathrm{min}}$ of $R_\circ/R_\mathcal{Q}$ for $\alpha > \alpha_c$ corresponding to the critical configuration where $\hat{\gamma}_A^{\mathrm{con}}$ and $\hat{\gamma}_A^{\mathrm{dis}}$ provide the same finite term F_A of the holographic entanglement entropy. The dashed blue curve is the asymptotic value (4.11).

When $\alpha > \alpha_c$ we have that $F_{\mathrm{con}} \to +\infty$ for $k \to 0$ and $F_{\mathrm{con}} \to (2\pi)^-$ for $k \to \infty$. This implies that at least a local minimum exists. We observe numerically that F_{con} has only one local extremum for $k = k_{\circ,\,\mathrm{min}}$, i.e. the same value for k corresponding to the minimum of the ratio $R_\circ/R_\mathcal{Q}$. This observation and the fact that, whenever two solutions $\hat{\gamma}_A^{\mathrm{con}}$ can be found, for their values $k_1 < k_2$ of k we have $k_1 < k_{\circ,\,\mathrm{min}} < k_2$ lead to conclude that $F_{\mathrm{con}}(k_2) < 2\pi$. Hence, the holographic entanglement entropy is obtained by comparing 2π with F_{con} evaluated on k_1. When $\alpha > \alpha_c$, let us denote with $k = k_c$ the solution of $F_{\mathrm{con}} = 2\pi$, which can be found numerically and characterises the configuration where the subleading terms for $\hat{\gamma}_A^{\mathrm{con}}$ and $\hat{\gamma}_A^{\mathrm{dis}}$ take the same value. Since $k_c < k_{\circ,\,\mathrm{min}}$, the minimal surface providing the holographic entanglement entropy is $\hat{\gamma}_A^{\mathrm{con}}$ if $k_1 < k_c$ and $\hat{\gamma}_A^{\mathrm{dis}}$ if $k_1 > k_c$. Denoting by $r_{\circ,c}$ the value of the ratio $R_\circ/R_\mathcal{Q}$ for the critical configuration having $k = k_c$, in figure 8 we show $r_{\circ,\,\mathrm{min}} < r_{\circ,c}$ in terms of $\alpha \in (\alpha_c, \pi)$.

The solid curves in figure 9, which are parameterised by α, have been obtained by combining (4.9) and (4.13) through a parametric plot. The allowed configurations have $R_\circ/R_\mathcal{Q} < 1$. A vertical line having $R_\circ/R_\mathcal{Q} < 1$ can intersect twice a solid curve corresponding to a fixed value of $\alpha > \alpha_c$. These two intersection points provide the values of F_{con} (see figure 7) obtained from the two values of k given by the intersection of the horizontal line $R_\circ/R_\mathcal{Q}$ with the curve in figure 5 having the same α.

In figure 9, the value of $R_\circ/R_\mathcal{Q}$ corresponding to the intersection between F_{con} for a given α and the horizontal dashed line (whose height is 2π) is $r_{\circ,c}$ (see the red line in figure 8), while $r_{\circ,\,\mathrm{min}}$ is the value of $R_\circ/R_\mathcal{Q}$ corresponding to the cusp.

JHEP08(2018)164

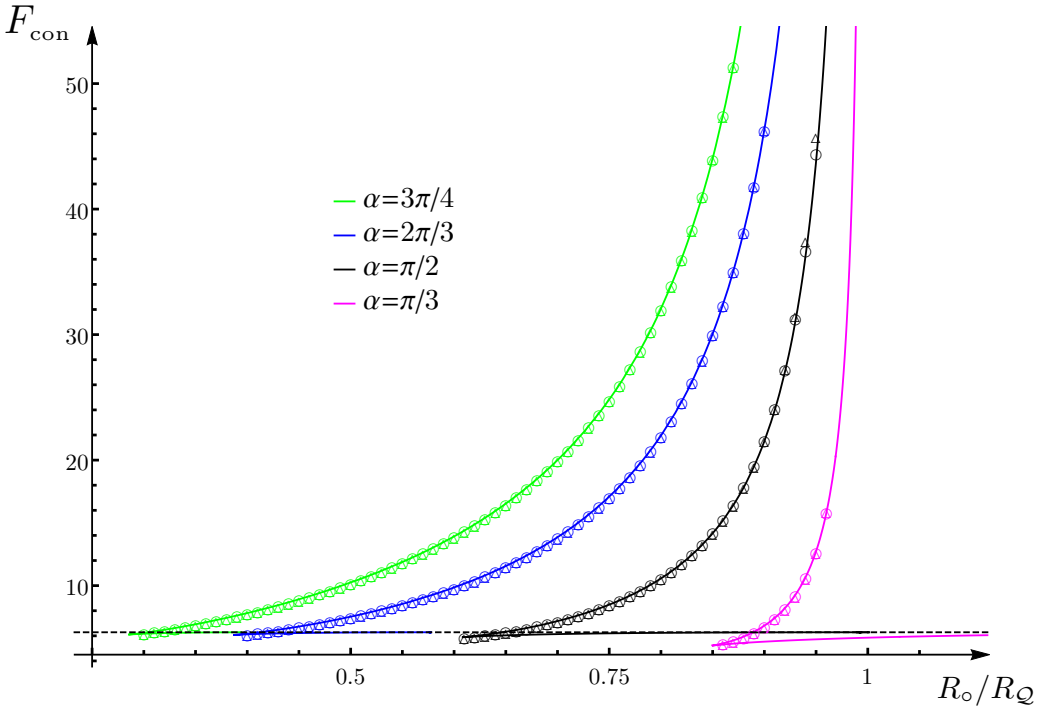

Figure 9. The subleading term $F_{\rm con}$ for the extremal surfaces $\hat{\gamma}_A^{\rm con}$ intersecting orthogonally $\mathcal{Q}$ in terms of the ratio $R_\circ/R_{\mathcal{Q}}$, for some values of α. The allowed configurations have $R_\circ/R_{\mathcal{Q}} < 1$. The solid curves have been obtained by combining the analytic expressions (4.9) and (4.13). The horizontal dashed line corresponds to the value of the subleading term of the hemisphere $\hat{\gamma}_A^{\rm dis}$, i.e. $F_A = 2\pi$. The data points are the numerical values obtained through Surface Evolver. The ones below the horizontal dashed line correspond to extremal surfaces that are not global minima. Different kind of markers are associated to the two different ways employed to extract $F_{\rm con}$ from the numerical data provided by Surface Evolver: either by subtracting the area law term from the area of the entire extremal surface (empty circles) or by applying the general formula (2.18) (empty triangles).

The analytic expression for $F_{\rm con}$ has been checked numerically with Surface Evolver, by adapting the method discussed in [87] to the configurations considered in this manuscript. The numerical results are the data points in figure 9, where the two different kind of markers (the empty circles and the empty triangles) correspond to two different ways to obtain the numerical value of $F_{\rm con}$ from the numerical data about the extremal surface $\hat{\gamma}_A^{\rm con}$. One way is to evaluate $\hat{\mathcal{A}}_\varepsilon^{\rm SE} - 2\pi R_\circ/\varepsilon$, being $\hat{\mathcal{A}}_\varepsilon^{\rm SE}$ the numerical value of the area of the extremal surface $\hat{\gamma}_A^{\rm con}$. The other method consists in finding $F_{\rm con}$ by plugging into (2.18) the geometrical quantities about $\hat{\gamma}_A^{\rm con}$ required to employ this formula, which are also given by Surface Evolver.

Notice that figure 9 shows that the extremal surfaces $\hat{\gamma}_A^{\rm con}$ do not exist when $R_\circ/R_{\mathcal{Q}} \to 0$. This means that the hemisphere $\hat{\gamma}_A^{\rm dis}$ provides the holographic entanglement entropy in this regime, as expected.

The agreement between the solid curves and the data points in figure 9 provides a highly non trivial confirmation of the analytic expressions obtained above.

JHEP08(2018)164

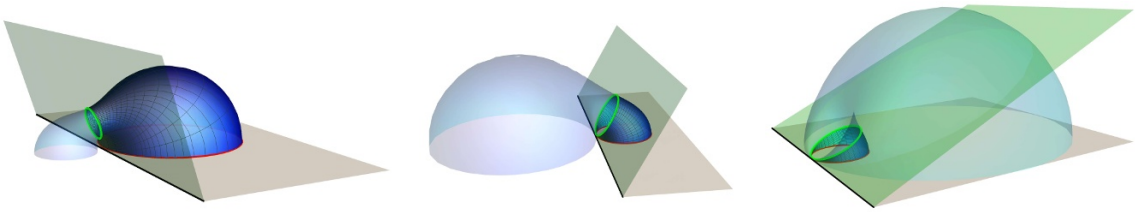

Figure 10. Extremal surfaces $\hat{\gamma}_A^{\text{con}}$ anchored to a disk of radius R (bounded by the red circle) at finite distance d from the flat boundary (see section 4.2). Here $d/R \sim 0.042$ is fixed and different values of α are considered: $\alpha = \pi/2.5$ (left), $\alpha = 2\pi/3$ (middle) and $\alpha = 2.7$ (right). The surface $\hat{\gamma}_A^{\text{con}}$ intersects the green half plane $\mathcal{Q}$ orthogonally along the green circle $\partial\hat{\gamma}_{\mathcal{Q}}$. The shaded surfaces correspond to the auxiliary surfaces $\hat{\gamma}_{A,\,\text{aux}}^{\text{con}}$ (see also appendix D). The extremal surface $\hat{\gamma}_A^{\text{con}}$ is the global minimum when the corresponding F_A is larger than 2π. Here $F_A = 5.6$ (left), $F_A = 17.1$ (middle) and $F_A = 47.1$ (right). The surface in the left panel has the smallest area among the two solutions $\hat{\gamma}_A^{\text{con}}$ but the global minimum is the hemisphere $\hat{\gamma}_A^{\text{dis}}$ in this case.

The formula (4.13) can be found also by specialising the general result (2.19) to the extremal surfaces $\hat{\gamma}_A^{\text{con}}$ for the disks A that we are considering. The details of this computation have been reported in appendix B.2 and in the following we report only the main results. For the surface integral in (2.19) we find

$$\int_{\hat{\gamma}_A} \frac{(\tilde{n}^z)^2}{z^2}\, d\tilde{\mathcal{A}} = 2\pi \left(\frac{1+\eta_\alpha}{2}\, \mathcal{F}_{k,-}(\zeta_*) + \frac{1-\eta_\alpha}{2} \Big[\mathcal{F}_{k,+}(\zeta_m) + \mathcal{F}_{k,-}(\zeta_m) - \mathcal{F}_{k,+}(\zeta_*) \Big] \right) \tag{4.18}$$

where the functions $\mathcal{F}_{k,\pm}$ can be written in terms of the function $\mathcal{F}_k$ introduced in (4.14) as follows (the derivation of this identity is briefly discussed in appendix B.2)

$$\mathcal{F}_{k,\pm}(\zeta) = \mathcal{F}_k(\zeta) - \frac{\sqrt{k(\zeta^2+1)-\zeta^4}}{\sqrt{k}\,\zeta\big(\zeta^2+1\big)} \pm \frac{\zeta^2}{\sqrt{k}\,(\zeta^2+1)} \tag{4.19}$$

Since for $\zeta = \zeta_m$ the expression under the square root in (4.19) vanishes, it is straightforward to observe that, by plugging (4.19) into (4.18), one obtains (4.13) and an additive contribution which depends on ζ_* but that does not contain ζ_m. This additive contribution is cancelled by the integral over the line $\partial\hat{\gamma}_{\mathcal{Q}} = \hat{\gamma}_A^{\text{con}} \cap \mathcal{Q}$ in (2.19), which gives

$$\int_{\partial\hat{\gamma}_{\mathcal{Q}}} \frac{\tilde{b}^z}{z}\, d\tilde{s} = 2\pi\, \frac{\sqrt{\zeta_*^2 + (\sin\alpha)^2}\,\zeta_* - \cos\alpha}{\zeta_*\,(\zeta_*^2+1)} \tag{4.20}$$

This concludes our analysis of the disk concentric to a circular boundary. We remark that we can easily study disks which are not concentric to the circular boundary by combining the analytic expressions presented above with the mapping discussed in appendix A.

4.2 Disk disjoint from a flat boundary

In the final part of this section we consider a disk A of radius R at finite distance d from a flat boundary, in the $\text{AdS}_4/\text{BCFT}_3$ setup described in section 2.2.1. By combining the results presented in section 4.1 with the mapping (A.3) discussed in appendix A, one can

JHEP08(2018)164

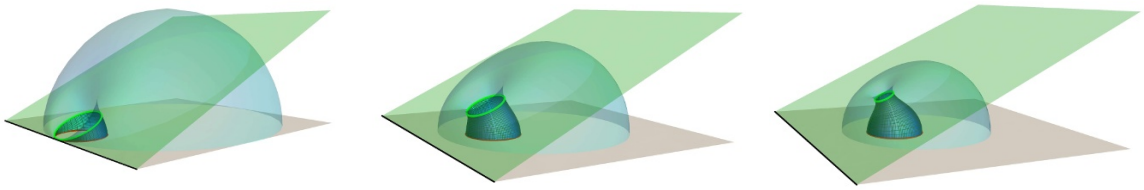

Figure 11. Extremal surfaces $\hat{\gamma}_A^{\rm con}$ anchored to a disk (bounded by the red circle) of radius R at finite distance d from the flat boundary, like in figure 10. Here $\alpha = 2.7$ is fixed (like in the right panel of figure 10) and the different values of d/R are considered: $d/R \sim 0.042$ (left), $d/R \sim 1.6$ (middle) and $d/R \sim 2.243$ (right). The shaded surfaces correspond to $\hat{\gamma}_{A,\,\rm aux}^{\rm con}$ and for all the configurations of this figure part of $\hat{\gamma}_{A,\,\rm aux}^{\rm con}$ belongs to the gravitational spacetime (2.21) (see also appendix D). The extremal surface $\hat{\gamma}_{A,\,\rm aux}^{\rm con}$ is a global minimum when its F_A is larger than 2π. The configuration in the left panel is the same shown in the right panel of figure 10. In the remaining panels $F_A = 6.95$ (middle) and $F_A = 6.13$ (right).

easily obtain the analytic expressions for the extremal surfaces anchored to ∂A and for the corresponding subleading term in the expansion of the area as $\varepsilon \to 0$.

The values of R and d are related to the parameters $R_\circ$ and $R_{\mathcal{Q}}$ characterising the configuration considered in section 4.1.1 and section 4.1.2 as follows

$$R = \frac{R_\circ\, R_{\mathcal{Q}}^2}{R_{\mathcal{Q}}^2 - R_\circ^2} \qquad\qquad d = \frac{R_{\mathcal{Q}}(R_{\mathcal{Q}} - R_\circ)}{2(R_{\mathcal{Q}} + R_\circ)} \tag{4.21}$$

From these expressions it is straightforward to find that

$$\frac{d}{R} = \frac{(R_\circ/R_{\mathcal{Q}} - 1)^2}{2\, R_\circ/R_{\mathcal{Q}}} \qquad\qquad \frac{R_\circ}{R_{\mathcal{Q}}} = \frac{d}{R} + 1 - \sqrt{\frac{d}{R}\left(\frac{d}{R} + 2\right)} \tag{4.22}$$

Since the extremal surfaces anchored to a disk disjoint from the flat boundary in the setup of section 2.2.1 are obtained by mapping the extremal surfaces described in section 4.1.1 through (A.3), also for this configuration we have at most three local extrema of the area functional, depending on the ratio d/R: the hemisphere $\hat{\gamma}_A^{\rm dis}$ and at most two solutions $\hat{\gamma}_A^{\rm con}$ intersecting the half plane $\mathcal{Q}$ orthogonally.

In figure 10 we show some examples of $\hat{\gamma}_A^{\rm con}$ for a fixed configuration of the disk A and three different slopes of $\mathcal{Q}$ (the green half plane). In each panel, the shaded surface is the auxiliary surface $\hat{\gamma}_{A,\,\rm aux}^{\rm con}$ corresponding to $\hat{\gamma}_A^{\rm con}$, which intersects orthogonally $\mathcal{Q}$ along $\partial\hat{\gamma}_{\mathcal{Q}}$ and is such that $\hat{\gamma}_A^{\rm con} \cup \hat{\gamma}_{A,\,\rm aux}^{\rm con}$ is an extremal surface in $\mathbb{H}_3$ anchored to the two disjoint circles (one of them is ∂A). In figure 11 we show $\hat{\gamma}_A^{\rm con}$ and the corresponding $\hat{\gamma}_{A,\,\rm aux}^{\rm con}$ for a fixed value of α and three different values of d/R. Notice that for some configurations $\hat{\gamma}_{A,\,\rm aux}^{\rm con}$ lies entirely outside the gravitational spacetime (2.21) (see e.g. the left panel and the middle panel of figure 10), while for other ones part of $\hat{\gamma}_{A,\,\rm aux}^{\rm con}$ belongs to it. The latter case occurs when the auxiliary region $A_{\rm aux}$ is a subset of the half plane $x > 0$, where also A is defined.

For the extremal surfaces that we are considering, the leading term of $\mathcal{A}[\hat{\gamma}_\varepsilon]$ as $\varepsilon \to 0$ is the area law term $2\pi R/\varepsilon$ and the subleading finite term is $-\max(2\pi, \widehat{F}_{\rm con})$, like in (4.12), where $\widehat{F}_{\rm con}$ corresponds to the maximum between the values of $F_{\rm con}$ evaluated for the

JHEP08(2018)164

extrema $\hat{\gamma}_A^{\rm con}$. The analytic expression of $F_{\rm con}$ as function of d/R can be obtained through a parametric plot involving $F_{\rm con}$ in (4.13), d/R in (4.22) and $R_\circ/R_{\mathcal{Q}}$ in (4.9). This procedure has been employed to find the solid black curves in figure 13, which correspond to a disk.

From (4.22), it is straightforward to observe that $d/R \to \infty$ corresponds to $R_\circ/R_{\mathcal{Q}} \to 0$, and $d/R \to 0$ to $R_\circ/R_{\mathcal{Q}} \to 1$. Thus, when $d/R \to \infty$ the hemisphere $\hat{\gamma}_A^{\rm dis}$ is the minimal surface providing the holographic entanglement entropy (see also section 4.1.2). In the opposite limiting regime $d/R \to 0$, the second expression in (4.22) implies that $R_\circ/R_{\mathcal{Q}} = 1 - \sqrt{2\,d/R} + d/R + O((d/R)^{3/2})$. Hence, from the expansion (4.17), it is straightforward to obtain that $F_{\rm con} = 2\pi\,\mathfrak{g}(\alpha)^2/\sqrt{2d/R} + \mathcal{O}\big(\sqrt{d/R}\big)$ at leading order.

5 On smooth domains disjoint from the boundary

Analytic expressions for the subleading term F_A in (1.4) can be obtained for configurations which are particularly simple or highly symmetric. Two important cases have been discussed in section 3 and section 4. In order to find analytic solutions for an extremal surface anchored to a generic entangling curve, typically a partial differential equation must be solved, which is usually a difficult task. Thus, it is useful to develop efficient numerical methods that allow us to study the shape dependence of F_A.

The crucial tool of our numerical analysis is Surface Evolver, which has been already employed to study the holographic entanglement entropy in AdS_4/CFT_3 [42, 45] and to check the corner functions in $AdS_4/BCFT_3$ [87]. In this manuscript we consider some regions disjoint from the boundary in $AdS_4/BCFT_3$. In section 4.1 Surface Evolver has been used to check numerically the analytic expressions of the extremal surfaces and of F_A for a disk concentric to a circular boundary (see figure 6 and figure 9 respectively). In this section we use Surface Evolver to study the extremal surfaces $\hat{\gamma}_A$ and the corresponding F_A for some simple domains which cannot be treated through analytic methods.

Considering the simple $AdS_4/BCFT_3$ setup described in section 2.2.1, in figure 1 we showed the extremal surface corresponding to a region A with a complicated shape (the entangling curve is the red curve in the inset) which has been constructed by using Surface Evolver and which is very difficult to describe analytically.

In the same setup, let us consider, for simplicity, regions A delimited by ellipses at distance d from the flat boundary with one of the semiaxis parallel to the flat boundary. These regions are given by the points $(x, y) \in \mathbb{R}^2$ with $x > 0$ such that $(x - d - R_\perp)^2/R_\parallel^2 + y^2/R_\perp^2 \leqslant 1$, where $R_\perp$ and $R_\parallel$ are the lengths of the semiaxis which are respectively orthogonal and parallel to the flat boundary $x = 0$. As for the extremal surfaces anchored to the entangling curve ∂A, either they are disconnected from the half plane $\mathcal{Q}$ or they intersect it orthogonally. The occurrence of these different kind of extremal surfaces and which of them gives the global minimum depend on the values of α, of the ratio $d/R_\perp$ and of the eccentricity of A. For some configurations only the solutions disconnected from $\mathcal{Q}$ are allowed, while for other configurations only the extremal surfaces intersecting $\mathcal{Q}$ exist, as discussed in a specific example in the final part of section 4.1.1. In figure 12 we show two examples of extremal surfaces anchored to ellipses in the $z = 0$ half plane (the red curves) which intersect $\mathcal{Q}$ orthogonally along the green line $\partial\hat{\gamma}_{\mathcal{Q}}$.

JHEP08(2018)164

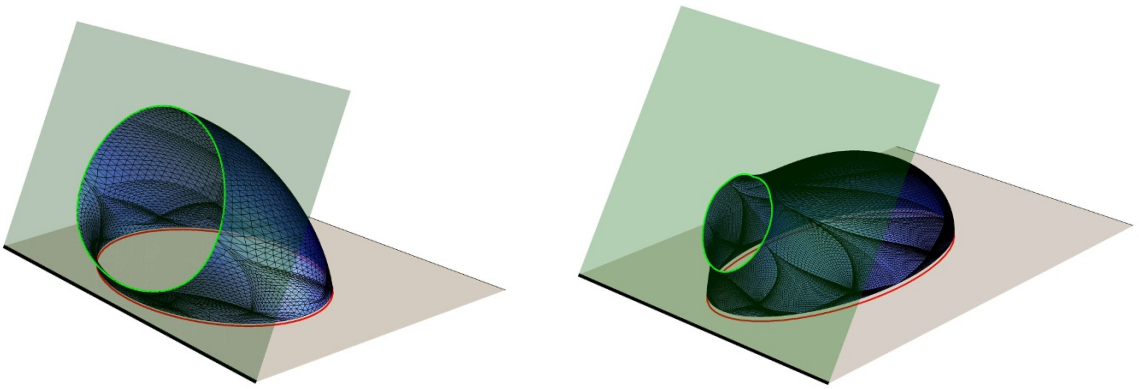

Figure 12. Extremal surfaces $\hat{\gamma}_A^{\rm con}$ found with Surface Evolver in the gravitational setup described in section 2.2.1. The extremal surfaces are anchored to the boundary of two different ellipses A (red curves) and intersect orthogonally the half plane $\mathcal{Q}$ with $\alpha = 2\pi/3$ (green half plane). Here $\varepsilon = 0.03$. Denoting by $R_\perp$ and $R_\parallel$ the lengths of the semiaxis which are respectively orthogonal and parallel to the flat boundary, and by d the distance of ∂A from the flat boundary, we have $d/R_\perp = 0.2$ in both the panels. Instead, $R_\parallel = 2R_\perp$ in the left panel and $R_\parallel = 0.5R_\perp$ in the right panel.

In figure 13 the values of the subleading term for extremal surfaces intersecting $\mathcal{Q}$ and anchored to various ellipses are plotted in terms of the ratio $d/R_\perp$. These data points have been obtained through Surface Evolver by first constructing the extremal surface $\hat{\gamma}_\varepsilon^{\rm SE}$ anchored to the ellipses defined at $z = \varepsilon$ and then employing the information about $\hat{\gamma}_\varepsilon^{\rm SE}$ provided by the code (in particular its area $\mathcal{A}[\hat{\gamma}_\varepsilon^{\rm SE}]$ and its normal vectors) in two different ways. One way to extract the subleading term is to compute $P_A/\varepsilon - \mathcal{A}[\hat{\gamma}_\varepsilon^{\rm SE}]$ (empty circles in figure 13). Another way is to evaluate (2.22) from the unit vector $\tilde{n}^\mu$ normal to $\hat{\gamma}_\varepsilon^{\rm SE}$ (empty triangles in figure 13). The agreement between these two approaches provides a strong numerical evidence that (2.22) is correct. The numerical analysis has been performed by adapting the method discussed in [87] to the configurations considered here.

The horizontal dashed lines in figure 13 correspond to the extremal surfaces that do not intersect $\mathcal{Q}$. Denoting by $F_{\rm dis}$ the subleading term in the expansion of $\mathcal{A}[\hat{\gamma}_\varepsilon^{\rm SE}]$ for these surfaces, we have that F_A in (1.4) is finite and given by $F_A = \max(F_{\rm con}, F_{\rm dis})$. The relation $F_{\rm con} = F_{\rm dis}$ provides the critical value of $d/R_\perp$ characterising the transition in the holographic entanglement entropy between the surfaces connected to $\mathcal{Q}$ and the ones disjoint from $\mathcal{Q}$ (see the intersection between the curve identified by the data points and the horizontal dashed line having the same colour in figure 13, except for the magenta points, that must be compared with the red dashed line).

The black points in figure 13 correspond to disks disjoint from a flat boundary and the solid black curves have been obtained through the analytic expressions discussed in section 4 (see (4.13) and (4.22)). The nice agreement with the data points found with Surface Evolver is a strong check for the analytic expressions.

In section 4 we have found that the critical value α_c (defined as the unique zero of (3.2)) for the slope of $\mathcal{Q}$ in the $AdS_4/BCFT_3$ setup of section 2.2.1 is such that extremal surfaces

JHEP08(2018)164

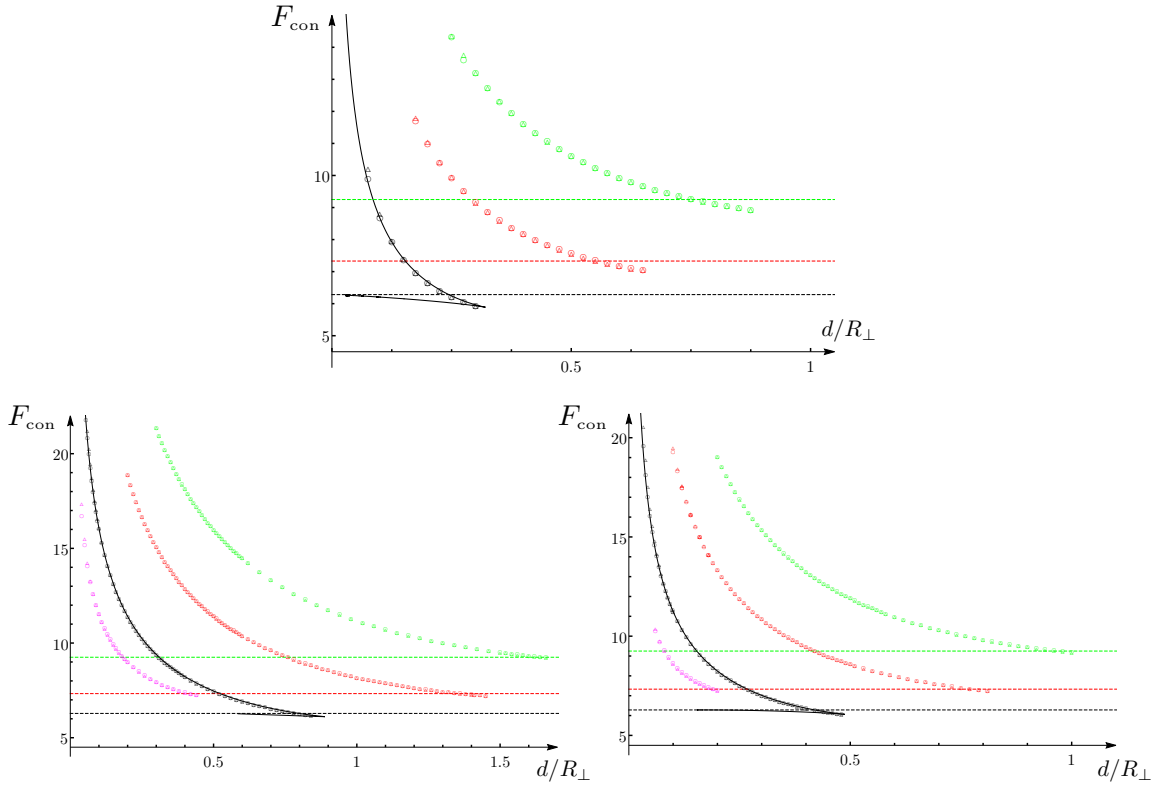

Figure 13. The subleading term $F_{\rm con}$ for the extremal surfaces $\hat{\gamma}_A^{\rm con}$ intersecting orthogonally the half plane $\mathcal{Q}$ and anchored to ellipses at distance d from a flat boundary (see figure 12). A semiaxes of the ellipse is orthogonal to the flat boundary and its length is $R_\perp$, while $R_\parallel$ is the length of the other one. The three panels are characterised by three diverse values of the slope α for the half plane $\mathcal{Q}$ (see figure 12): $\alpha = \pi/2$ (top), $\alpha = 2\pi/3$ (bottom right) and $\alpha = 3\pi/4$ (bottom left). Different colours correspond to different eccentricities: $R_\parallel = 3R_\perp$ (green), $R_\parallel = 2R_\perp$ (red), $R_\parallel = R_\perp$ (black) and $R_\parallel = 0.5R_\perp$ (magenta). The solid black curves correspond to the analytic expressions obtained in section 4.2 for disks. The dashed horizontal lines provide the value $F_A = F_{\rm dis}$ for the extremal surfaces disconnected from $\mathcal{Q}$. In particular, $F_{\rm dis} = 9.25$ (green), $F_{\rm dis} = 2\pi$ (black) and $F_{\rm dis} = 7.33$ (red and magenta).

anchored to a disk A disjoint from the flat boundary and intersecting $\mathcal{Q}$ orthogonally do not exist for $\alpha \leqslant \alpha_c$. We find it reasonable to conjecture the validity of this property (with same α_c) for any smooth region A disjoint from the boundary in the $AdS_4/BCFT_3$ setups described in section 2.2.1 and section 2.2.2.

We find it worth exploring the existence of bounds on the subleading term F_A. In the AdS_4/CFT_3 duality when the dual gravitational background is AdS_4, by employing a well known bound for the Willmore functional in $\mathbb{R}^3$, it has been shown that $F_A \geqslant 2\pi$ for any kind of spatial region, including the ones with singular ∂A and the ones made by disjoint components [42].

In the remaining part of this section we discuss that, in the context of $AdS_4/BCFT_3$ and when the gravitational dual is the part of AdS_4 delimited by $\mathcal{Q}$ and the conformal boundary, for any kind of spatial region A disjoint from the boundary we have

$$F_A \geqslant 2\pi \tag{5.1}$$

JHEP08(2018)164

If A contains at least one corner, this bound is trivially satisfied because F_A diverges logarithmically and the coefficient of this divergence is positive, being determined by the corner function of [22, 23].

For regions A with smooth ∂A, the subleading term F_A in (1.4) is finite and the corresponding minimal surface $\hat{\gamma}_A$ is such that either $\hat{\gamma}_A \cap \mathcal{Q} = \emptyset$ or $\hat{\gamma}_A \cap \mathcal{Q} \neq \emptyset$. In the former case $\hat{\gamma}_A$ is also a minimal surface in $\mathbb{H}_3$, therefore we can employ the observation made in [42] for AdS_4/CFT_3 and conclude that (5.1) holds.

If $\hat{\gamma}_A \cap \mathcal{Q} \neq \emptyset$, let us denote by $F_A = F_{\rm con}$ the value of the subleading term corresponding to $\hat{\gamma}_A$. In these cases, we have two possibilities: either another extremal surface $\hat{\gamma}_A^{\rm dis}$ such that $\hat{\gamma}_A^{\rm dis} \cap \mathcal{Q} = \emptyset$ exists or not. In the former case, being $\hat{\gamma}_A$ the global minimum, we have that $F_{\rm con} \geqslant F_{\rm dis} \geqslant 2\pi$, where the last inequality is obtained from the observation of [42], as above.

The remaining configurations are the ones such that only the extremal surface $\hat{\gamma}_A$ with $\hat{\gamma}_A \cap \mathcal{Q} \neq \emptyset$ exists (see e.g. the explicit case discussed in the final part of section 4.1.1). In these cases $\hat{\gamma}_A^{\rm dis}$ does not occur because, by introducing the extremal surface $\hat{\gamma}_A^{(0)}$ in $\mathbb{H}_3$ anchored to ∂A, we have that $\hat{\gamma}_A^{(0)} \cap \mathcal{Q} \neq \emptyset$. Let us consider the part $\hat{\gamma}_A^{\lessdot} \subset \hat{\gamma}_A^{(0)}$ of $\hat{\gamma}_A^{(0)}$ belonging to the region of AdS_4 delimited by $\mathcal{Q}$ and the conformal boundary. We remark that $\hat{\gamma}_\varepsilon^{\lessdot}$ intersects $\mathcal{Q}$ but, typically, they are not orthogonal along their intersection. Restricting both $\hat{\gamma}_A^{(0)}$ and $\hat{\gamma}_A^{\lessdot}$ to $z \geqslant \varepsilon$, for the resulting surfaces $\hat{\gamma}_\varepsilon^{(0)}$ and $\hat{\gamma}_\varepsilon^{\lessdot}$ the expansion (1.3) holds with the same P_A but different $O(1)$ terms, that will be denoted by $F_A^{(0)}$ and $F_A^{\lessdot}$ respectively. Notice that the observation of [42] here gives $F_A^{(0)} \geqslant 2\pi$. Since $\hat{\gamma}_A^{\lessdot} \subset \hat{\gamma}_A^{(0)}$, we have $\mathcal{A}[\hat{\gamma}_\varepsilon^{(0)}] \geqslant \mathcal{A}[\hat{\gamma}_\varepsilon^{\lessdot}]$, which implies $F_A^{(0)} \leqslant F_A^{\lessdot}$, being P_A the same for $\hat{\gamma}_\varepsilon^{(0)}$ and $\hat{\gamma}_\varepsilon^{\lessdot}$. Since $F_{\rm con}$ corresponds to an extremal surface and $\hat{\gamma}_\varepsilon^{\lessdot}$ is not extremal, we can conclude that $F_{\rm con} \geqslant F_A^{\lessdot}$. Collecting these observations, we find that $F_{\rm con} \geqslant F_A^{\lessdot} \geqslant F_A^{(0)} \geqslant 2\pi$.

This completes our discussion about the validity of the inequality (5.1) for any spatial region A disjoint from the boundary, including the ones having singular ∂A or that are made by disjoint connected components. We find it worth remarking that the bound (5.1) does not hold in general when A is adjacent to the boundary because the corner function is negative for some configurations [87].

6 Domains with corners adjacent to the boundary

The holographic entanglement entropy of domains A with corners whose tip is on the boundary contains a subleading logarithmic divergence whose coefficient is determined by a model dependent corner function which depends also on the boundary conditions. In the setups of $AdS_4/BCFT_3$ of section 2.2.1, the analytic expression of the corner function $F_\alpha(\omega)$ has been found in [87] from a direct evaluation of the area of the minimal surface corresponding to an infinite wedge adjacent to the flat boundary (see (1.5)).

Below, we show that the corner function $F_\alpha(\omega)$ can be also obtained also from (2.22). In section 6.1 we focus on the simplest configuration given by a half disk centered on the flat boundary, while in section 6.2 we discuss the most general case of an infinite wedge adjacent to the flat boundary with generic opening angle.

JHEP08(2018)164

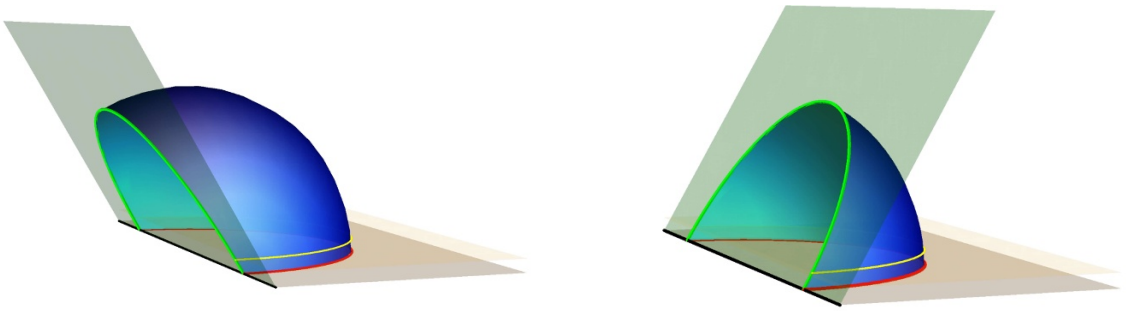

Figure 14. Minimal surfaces $\hat{\gamma}_A$ anchored to the entangling curve corresponding to a half disk A centered on the flat boundary. The slope of the green half plane $\mathcal{Q}$ is $\alpha = \pi/3$ in the left panel and $\alpha = 2\pi/3$ in the right panel. The yellow half plane has $z = \varepsilon$ and its intersection with $\hat{\gamma}_A$ is the yellow curve. The green curve corresponds to $\partial\hat{\gamma}_{\mathcal{Q}}$ in (6.2).

6.1 Half disk centered on the boundary

In the gravitational setup described in section 2.2.1, let us consider the half disk A of radius R centered in the origin, which belongs to the flat boundary, i.e. $A = \{(x, y) \in \mathbb{R}^2 \,|\, x^2 + y^2 \leqslant R^2,\, x \geqslant 0\}$. The minimal surface corresponding to this configuration is simply given by the part of the hemisphere anchored to the entire circle centered in the origin which satisfies the constraint 2.2.1. In figure 14 the minimal surface $\hat{\gamma}_A$ is shown for two different values of α. When $\alpha \neq \pi/2$, a non trivial logarithmic divergence occurs in the expansion of the area $\mathcal{A}[\hat{\gamma}_\varepsilon]$. In particular, it has been found that [87]

$$\mathcal{A}[\hat{\gamma}_\varepsilon] = \frac{\pi R}{\varepsilon} + 2\cot\alpha\, \log(R/\varepsilon) + O(1) \tag{6.1}$$

which tells us that $F_\alpha(\pi/2) = -\cot\alpha$ for the corner function introduced in (1.5), being the factor of 2 due to the fact that A has two corners adjacent to the boundary. The expression of $F_\alpha(\pi/2)$ has been first obtained in [74] by considering the equal bipartition of the half plane where the entangling curve is the half line orthogonal to the flat boundary.

It is instructive to show that the general formula (2.22) is able to reproduce the logarithmic term occurring in (6.1). Let us observe that the integral over $\hat{\gamma}_\varepsilon$ in (2.22) provides a finite result as $\varepsilon \to 0$ because $\hat{\gamma}_\varepsilon$ is part of the hemisphere $\hat{\gamma}_A \cup \hat{\gamma}_{A,\,\text{aux}}$ and, being the integrand positive, the integral over $\hat{\gamma}_\varepsilon$ is smaller than the integral over the entire hemisphere $\hat{\gamma}_A \cup \hat{\gamma}_{A,\,\text{aux}}$, which gives 2π.

The intersection between $\hat{\gamma}_A$ and $\mathcal{Q}$ is given by the following semi-circle

$$\partial\hat{\gamma}_{\mathcal{Q}} : \begin{cases} x^2 + y^2 + z^2 = R^2 \\ z = -\,x\tan\alpha \end{cases} \tag{6.2}$$

By employing the spherical coordinates

$$z = R\,\sin\theta\,\cos\phi \qquad x = -\,R\,\sin\theta\,\sin\phi \qquad y = R\,\cos\theta \tag{6.3}$$

one finds the following parametric representation of $\partial\hat{\gamma}_{\mathcal{Q}}$

$$\partial\hat{\gamma}_{\mathcal{Q}} : \quad (z, x, y) = R\big(\sin\theta\,\cos(\pi/2-\alpha)\,,\, -\sin\theta\,\sin(\pi/2-\alpha)\,,\, \cos\theta\big) \qquad \theta_\varepsilon \leqslant \theta \leqslant \pi - \theta_\varepsilon \tag{6.4}$$

JHEP08(2018)164

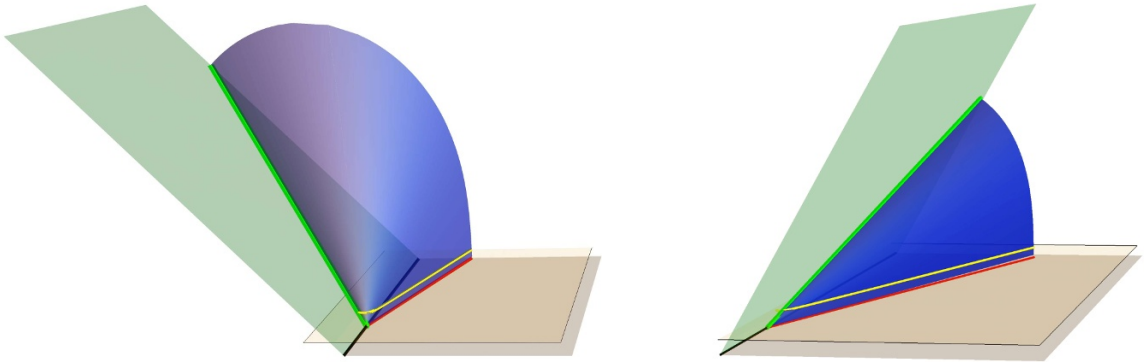

Figure 15. Minimal surface $\hat{\gamma}_A$ anchored to the entangling edge (the red line) of an infinite wedge A adjacent to the flat boundary, in the gravitational setup of section 2.2.1. The analytic results of [87] have been employed to plot these surfaces (see section 6.2). The green half plane is $\mathcal{Q}$ and the yellow plane corresponds to $z = \varepsilon$, and they intersect $\hat{\gamma}_A$ along the green line and the yellow curve respectively. Left: $\omega = 0.2$ and $\alpha = \pi/4$. Right: $\omega = 0.3$ and $\alpha = 2\pi/3$.

The angle θ_ε is given by the intersection of $\partial\hat{\gamma}_{\mathcal{Q}}$ with the cutoff $z = \varepsilon$; therefore it can be found from the condition $\varepsilon = R \sin\theta_\varepsilon \cos(\pi/2 - \alpha)$. Since the line element is $d\tilde{s} = R\, d\theta$, from (6.4) we easily obtain the following result for the line integral over $\partial\hat{\gamma}_{\mathcal{Q}}$ in (2.18) and (2.22) for this configuration

$$\int_{\partial\hat{\gamma}_{\mathcal{Q}}} \frac{\tilde{b}^z}{z}\, d\tilde{s} = -\cot\alpha \int_{\theta_\varepsilon}^{\pi-\theta_\varepsilon} \frac{1}{\sin\theta}\, d\theta = -\cot\alpha \, \log\big[\tan(\theta/2)\big]\Big|_{\theta_\varepsilon}^{\pi-\theta_\varepsilon} \tag{6.5}$$

As $\varepsilon \to 0$, at the leading order we obtain

$$\int_{\partial\hat{\gamma}_{\mathcal{Q}}} \frac{\tilde{b}^z}{z}\, d\tilde{s} = -\,2\cot\alpha \, \log(R/\varepsilon) + O(1) \tag{6.6}$$

Thus, the logarithmic divergence and its coefficient in (6.1) have been recovered by specifying the general formula (2.22) to this configuration, finding that they come from the line integral over $\partial\hat{\gamma}_{\mathcal{Q}}$.

6.2 Infinite wedge adjacent to the boundary

In the gravitational setup described in section 2.2.1, let us consider the following infinite wedge A adjacent to the flat boundary

$$A = \big\{(\rho,\phi)\,\big|\, 0 \leqslant \phi \leqslant \omega\,,\, \rho \leqslant L\big\} \qquad\qquad L \gg \varepsilon \tag{6.7}$$

where ω is the opening angle of the wedge and we have adopted the polar coordinates (ρ,ϕ) for the spatial section of the conformal boundary such that $\phi = 0$ corresponds to the positive y semiaxis, which are related to the usual Cartesian coordinates as $x = \rho\sin\phi$ and $y = \rho\cos\phi$.

The minimal surface $\hat{\gamma}_A$ has been found analytically in [87]. In figure 15 we show two examples of $\hat{\gamma}_A$ corresponding to the same A and to different slopes for $\mathcal{Q}$. In [87] the area

JHEP08(2018)164

of the corresponding regularised surface $\hat{\gamma}_\varepsilon = \hat{\gamma}_A \cap \{z \geqslant \varepsilon\}$ has been computed, finding (1.5) and an explicit expression for the corner function $F_\alpha(\omega)$.

The parametric form of the minimal surface $\hat{\gamma}_A$ can be written in cylindrical coordinates (z, ρ, ϕ) by introducing the following ansatz

$$(z, \rho, \phi) = \left(\frac{\rho}{q(\phi)} \, , \, \rho \, , \, \phi \right) \qquad \rho \in (0, L), \qquad \phi \in (\phi_* \, , \omega) \tag{6.8}$$

where ϕ_* corresponds to the value of ϕ characterising the line $\partial\hat{\gamma}_\mathcal{Q}$ along which $\hat{\gamma}_A \perp \mathcal{Q}$ (the green line in figure 15).

The function $q(\phi)$, which provides the minimal surface, can be implicitly obtained from (see (F.9) and (F.10) in [87])

$$\big|\phi - \omega + P_0(q_0)\big| = P(q, q_0) \tag{6.9}$$

where

$$P_0(q_0) \equiv \frac{1}{q_0} \left\{ (1 + Q_0^2) \, \Pi\left(-1/Q_0^2 \, , -Q_0^2\right) - Q_0^2 \, \mathbb{K}\left(-Q_0^2\right) \right\} \tag{6.10}$$

$$P(q, q_0) \equiv \frac{1}{q_0} \left\{ (1 + Q_0^2) \, \Pi\big(- 1/Q_0^2 \, , \, \sigma(q, q_0) \, \big| \, - Q_0^2\big) - Q_0^2 \, \mathbb{F}\big(\sigma(q, q_0) \, \big| \, - Q_0^2\big) \right\} \tag{6.11}$$

with

$$\sigma(q, q_0) \equiv \arctan \sqrt{\frac{q^2 - q_0^2}{1 + 2q_0^2}} \qquad\qquad Q_0^2 \equiv \frac{q_0^2}{1 + q_0^2} \in (0, 1) \tag{6.12}$$

being $\mathbb{F}(\phi|m)$ and $\Pi(n, \phi|m)$ the incomplete elliptic integrals of the first and third kind respectively, while $\mathbb{K}(x)$ is the complete elliptic integral of the first kind. Here q_0 is the minimum value of q. Given the opening angle ω of the wedge and the slope α of $\mathcal{Q}$, the values of q_0 and ϕ_* are obtained by inverting the following transcendental equations

$$\phi_*(\alpha, q_0) = \eta_\alpha \arcsin[s_*(\alpha, q_0)] \qquad \omega = P_0(q_0) + \phi_*(\alpha, q_0) - \eta_\alpha \, P\big(q_*(\alpha, q_0), q_0\big) \tag{6.13}$$

where we have introduced

$$s_*(\alpha, q_0) \equiv - \eta_\alpha \frac{\cot\alpha}{\sqrt{2}} \left\{ \frac{\sqrt{1 + 4(\sin\alpha)^2(q_0^4 + q_0^2)} - \cos(2\alpha)}{(\cos\alpha)^2 + q_0^4 + q_0^2} \right\}^{\frac{1}{2}} \qquad q_*(\alpha, q_0) = \frac{|\cot\alpha\,|}{s_*(\alpha, q_0)} \tag{6.14}$$

The expansion of the area of the minimal surface $\hat{\gamma}_\varepsilon$ as $\varepsilon \to 0$ is given by (1.5). The analytic expression of the corner function reads [87]

$$F_\alpha(\omega) = F(q_0) + \eta_\alpha \, \mathcal{G}\big(q_*(\alpha, q_0), q_0\big) \tag{6.15}$$

where

$$F(q_0) \equiv \frac{\mathbb{E}(\tilde{q}_0^2) - (1 - \tilde{q}_0^2) \, \mathbb{K}(\tilde{q}_0^2)}{\sqrt{1 - 2\tilde{q}_0^2}} \qquad\qquad \tilde{q}_0 = \frac{q_0^2}{1 + 2q_0^2} \tag{6.16}$$

JHEP08(2018)164

and

$$\mathcal{G}(q,q_0) \equiv \sqrt{1+q_0^2}\left\{\mathbb{F}\big(\sigma(q,q_0)\,\big|\,-Q_0^2\big)-\mathbb{E}\big(\sigma(q,q_0)\,\big|\,-Q_0^2\big)+\sqrt{\frac{(q^2+1)(q^2-q_0^2)}{(q_0^2+1)(q^2+q_0^2+1)}}\right\} \tag{6.17}$$

The goal of this section is to show that (6.15) can be recovered also from the general expression (2.22). In appendix C, we discuss the details of this computation, while in the following we only report the main intermediate steps. Let us remark that, while for the half disk centered on the flat boundary the logarithmic divergence in the expansion of $\mathcal{A}[\hat{\gamma}_\varepsilon]$ comes only from the line integral over $\partial\hat{\gamma}_\mathcal{Q}$ (see section 6.1), for the wedge adjacent to the boundary both the surface integral over $\hat{\gamma}_\varepsilon$ and the line integral over $\partial\hat{\gamma}_\mathcal{Q}$ provide a logarithmic divergence. In particular, for the line integral over $\partial\hat{\gamma}_\mathcal{Q}$ we find

$$\int_{\partial\hat{\gamma}_\mathcal{Q}} \frac{\tilde{b}^z}{z}\, d\tilde{s} = -\cot\alpha\,\sqrt{1+(\cos\alpha\,\cot\phi_*)^2}\,\log(L/\varepsilon)+\mathcal{O}(1) \tag{6.18}$$

Notice that, since for the half disk centered on the flat boundary $\phi_* = \eta_\alpha\,\pi/2$, the expression (6.18) is consistent with (6.6) (where we recall that the factor of 2 occurs because the half disk contains two corners).

The evaluation of the surface integral over $\hat{\gamma}_\varepsilon$ in (2.22) is less straightforward than (6.18) and it provides the following logarithmic divergence

$$\int_{\hat{\gamma}_\varepsilon} \frac{(\tilde{n}^z)^2}{z^2}\, d\tilde{\mathcal{A}} = \mathcal{I}(q_*,q_0)\log(L/\varepsilon)+O(1) \tag{6.19}$$

whose coefficient is given by

$$\mathcal{I}(q_*,q_0) \equiv F(q_0)-\eta_\alpha\left(S(q_*,q_0)+\sqrt{\frac{(q_*-q_0)\,(q_*+q_0)\,(q_*^2+q_0^2+1)}{q_*^2+1}}\right) \tag{6.20}$$

where

$$S(q_*,q_0) \equiv \sqrt{q_0^2+1}\left[\mathbb{E}\left(i\,\mathrm{arccsch}\,\frac{q_0}{\sqrt{q^2+1}}\,\middle|\,\frac{-q_0^2}{q_0^2+1}\right)-\mathbb{F}\left(i\,\mathrm{arccsch}\,\frac{q_0}{\sqrt{q^2+1}}\,\middle|\,\frac{-q_0^2}{q_0^2+1}\right)\right]\Bigg|_{q_0}^{q_*} \tag{6.21}$$

By combining (6.18) and (6.19) as prescribed by the general formula (2.18) (see the appendix C for some technical details), we recover the expression (6.15) for the corner function.

7 Conclusions

Understanding the gauge/gravity correspondence when the dual conformal field theory has a physical boundary is an important question.

In this manuscript we studied the holographic entanglement entropy in $AdS_4/BCFT_3$ for spatial regions having arbitrary shapes, along the lines of [68–74, 86, 87]. Considering the expansion of the holographic entanglement entropy as the UV cutoff vanishes (see (1.4)

JHEP08(2018)164

and (1.2)), our main result is the analytic formula (2.12) for the subleading term F_A, that can be applied for any spatial region and any static gravitational background. Known analytic expressions corresponding to some particular configurations such as an infinite strip parallel to a flat boundary [72, 73, 86, 87] or an infinite wedge adjacent to a flat boundary [87] have been recovered through (2.12).

The second result is the analytic study of the extremal surfaces anchored to a disk disjoint from a boundary which is either flat or circular, when the gravitational background is a part of $\mathbb{H}_3$. The corresponding expression for the subleading term F_A has been obtained both by evaluating the area in the standard way and by specialising (2.12) to this configuration. Furthermore, when the spatial section of the gravitational spacetime is a part of $\mathbb{H}_3$, we found the bound $F_A \geqslant 2\pi$ for any region A that does not intersect the boundary.

The numerical analysis of the holographic entanglement entropy in $\mathrm{AdS}_4/\mathrm{BCFT}_3$ performed in this manuscript is based on Surface Evolver, which has been previously employed to study the holographic corner functions in $\mathrm{AdS}_4/\mathrm{BCFT}_3$ [87] and the holographic entanglement entropy in $\mathrm{AdS}_4/\mathrm{CFT}_3$ for regions with arbitrary shape [42, 45].

Many interesting directions can be explored in the future. In the AdS/BCFT construction, it is important to identify the possible relation occurring between the geometrical parameter α in the bulk and the allowed boundary conditions for the dual BCFT_3. As for the holographic entanglement entropy in $\mathrm{AdS}_4/\mathrm{BCFT}_3$, gravitational backgrounds dual to a BCFT_3 at finite temperature or to a boundary RG flows could be considered. The expression (2.12) found in this manuscript holds also in these cases; nonetheless, it would be interesting to find explicit analytic expressions in some simple setups. An interesting direction to address involves time-dependent gravitational backgrounds.

The results and the methods discussed in this manuscript could be useful also in the context of the gauge/gravity correspondence in the presence of defects (AdS/dCFT) [86, 101–105].

Acknowledgments

It is our pleasure to thank Matthew Headrick, Luca Heltai, Alberto Sartori, Michael Smolkin, Tadashi Takayanagi and in particular Jonas Hirsch and Martina Teruzzi for useful discussions. JS and ET are grateful to the Instituto Balseiro, Bariloche, for hospitality and the stimulating environment enjoyed during the *It from Qubit* workshop/school. ET thanks the Hebrew University for the hospitality during part of this work. We are grateful to the Galileo Galilei Institute for Theoretical Physics for the hospitality during the program *Entanglement in Quantum Systems* and the INFN for partial support during the final stage of this work.

JHEP08(2018)164

A Useful mappings

In this appendix we discuss two useful transformations employed in section 2.2 and section 4.

Let us consider the map $(x, y, z) \to (X, Y, Z)$ with $z > 0$ and $Z > 0$ defined by [100]

$$\begin{cases} X = \lambda \, \dfrac{x - a_x + c_x \left[(\boldsymbol{x} - \boldsymbol{a})^2 + z^2 \right]}{1 + 2\, \boldsymbol{c} \cdot (\boldsymbol{x} - \boldsymbol{a}) + \boldsymbol{c}^2 \left[(\boldsymbol{x} - \boldsymbol{a})^2 + z^2 \right]} \\ Y = \lambda \, \dfrac{y - a_y + c_y \left[(\boldsymbol{x} - \boldsymbol{a})^2 + z^2 \right]}{1 + 2\, \boldsymbol{c} \cdot (\boldsymbol{x} - \boldsymbol{a}) + \boldsymbol{c}^2 \left[(\boldsymbol{x} - \boldsymbol{a})^2 + z^2 \right]} \\ Z = \lambda \, \dfrac{z}{1 + 2\, \boldsymbol{c} \cdot (\boldsymbol{x} - \boldsymbol{a}) + \boldsymbol{c}^2 \left[(\boldsymbol{x} - \boldsymbol{a})^2 + z^2 \right]} \end{cases} \tag{A.1}$$

where $\lambda > 0$, the vectors $\boldsymbol{x} = (x, y)$, $\boldsymbol{a} = (a_x, a_y)$ and $\boldsymbol{c} = (c_x, c_y)$ belong to $\mathbb{R}^2$ and $\cdot$ denotes the standard scalar product between vectors in $\mathbb{R}^2$. The transformation (A.1) leaves the metric (2.17) invariant up to a conformal factor. On the conformal boundary, given by $Z = z = 0$, the map (A.1) becomes a special conformal transformation.

The first special case of (A.1) that we need is the map sending the right half plane $\{(x, y) \in \mathbb{R}^2, x \geqslant 0\}$ at $z = 0$ into the disk $\{(X, Y) \in \mathbb{R}^2, X^2 + Y^2 \leqslant R_{\mathcal{Q}}^2\}$ of radius $R_{\mathcal{Q}}$ at $Z = 0$. Since this transformation must send the straight line $(x, y, z) = (0, y, 0)$ into the circle $\mathcal{C}_{\mathcal{Q}}$ given by $(X, Y, Z) = (R_{\mathcal{Q}} \cos\phi, R_{\mathcal{Q}} \sin\phi, 0)$ with $\phi \in [0, 2\pi)$, it can be constructed by first setting $a_y = a_z = 0$ and $x = z = 0$ in (A.1), and then imposing $X^2 + Y^2 = R_{\mathcal{Q}}^2$. This leads to

$$\frac{\lambda^2 \left(a_x^2 + y^2\right)}{\left(a_x^2 + y^2\right)\left(c_x^2 + c_y^2\right) - 2a_x c_x + 2c_y y + 1} - R_{\mathcal{Q}}^2 = 0 \qquad \forall y \in \mathbb{R} \tag{A.2}$$

which can be written as a quadratic equation in y that must hold $\forall y \in \mathbb{R}$; therefore we have to impose the vanishing of its coefficients. This procedure gives $a_x = \pm R_{\mathcal{Q}}/(2\lambda)$ and $\boldsymbol{c} = (\pm\lambda/R_{\mathcal{Q}}, 0)$, where the choice of the sign determines whether the right half plane $x \geqslant 0$ is mapped in the region inside (positive sign) or outside (negative sign) the circle $\mathcal{C}_{\mathcal{Q}}$. Considering the former option, we find that (A.1) becomes

$$\begin{cases} X = \dfrac{R_{\mathcal{Q}} \left[4\lambda^2 (x^2 + y^2 + z^2) - R_{\mathcal{Q}}^2 \right]}{R_{\mathcal{Q}}^2 + 4\lambda^2 \left(x^2 + y^2 + z^2\right) + 4\lambda R_{\mathcal{Q}}\, x} \\ Y = \dfrac{4\lambda R_{\mathcal{Q}}^2\, y}{R_{\mathcal{Q}}^2 + 4\lambda^2 \left(x^2 + y^2 + z^2\right) + 4\lambda R_{\mathcal{Q}}\, x} \\ Z = \dfrac{4\lambda R_{\mathcal{Q}}^2\, z}{R_{\mathcal{Q}}^2 + 4\lambda^2 \left(x^2 + y^2 + z^2\right) + 4\lambda R_{\mathcal{Q}}\, x} \end{cases} \qquad \begin{cases} x = \dfrac{R_{\mathcal{Q}} \left(R_{\mathcal{Q}}^2 - X^2 - Y^2 - Z^2 \right)}{2\lambda \left[(R_{\mathcal{Q}} - X)^2 + Y^2 + Z^2 \right]} \\ y = \dfrac{R_{\mathcal{Q}}^2\, Y}{\lambda \left[(R_{\mathcal{Q}} - X)^2 + Y^2 + Z^2 \right]} \\ z = \dfrac{R_{\mathcal{Q}}^2\, Z}{\lambda \left[(R_{\mathcal{Q}} - X)^2 + Y^2 + Z^2 \right]} \end{cases} \tag{A.3}$$

where also the inverse map has been reported. The transformations in (A.3) relate the setups described in section 2.2.1 and section 2.2.2. Since in (A.3) the constant λ can be reabsorbed through the rescaling $(x, y, z) \to \lambda(x, y, z)$, which leaves $\mathbb{H}_3$ invariant, we are

JHEP08(2018)164

allowed to set $\lambda = 1$ in (A.3) without loss of generality. The first transformation in (A.3) maps the half plane (2.20) into the following spherical cap [69]

$$X^2 + Y^2 + (Z - R_{\mathcal{Q}} \cot\alpha)^2 = \frac{R_{\mathcal{Q}}^2}{\sin^2\alpha} \qquad Z > 0 \tag{A.4}$$

which has been written also in (2.24) by means of cylindrical coordinates. When $\alpha = \pi/2$, (A.4) reduces to the hemisphere of radius $R_{\mathcal{Q}}$.

The second map in (A.3) has been used in section 4.2 to obtain the holographic entanglement entropy of a disk disjoint from a flat boundary starting from the holographic entanglement entropy of a disk concentric to a circular boundary computed in section 4.1. Indeed, by considering the circle $(X, Y) = (b_\circ + R_\circ \cos\phi, R_\circ \sin\phi)$ with $\phi \in [0, 2\pi)$ inside the disk delimited by $\mathcal{C}_{\mathcal{Q}}$, its image through the second map in (A.3) is the circle $(x, y) = (d + R + R\cos\phi, R\sin\phi)$ in the right half plane at $z = 0$, which has radius R and distance d from the straight boundary at $x = 0$. We find that $(R_\circ, b_\circ)$ can be written in terms of (R, d) as follows

$$\frac{R_\circ}{R_{\mathcal{Q}}} = \frac{4\, R/R_{\mathcal{Q}}}{1 + 4(d/R_{\mathcal{Q}} + 2R/R_{\mathcal{Q}})d/R_{\mathcal{Q}} + 4(d/R_{\mathcal{Q}} + R/R_{\mathcal{Q}})} \tag{A.5}$$

$$\frac{b_\circ}{R_{\mathcal{Q}}} = 1 - \frac{2\big[1 + 2(d/R_{\mathcal{Q}} + R/R_{\mathcal{Q}})\big]}{\big[1 + 2(d/R_{\mathcal{Q}} + 2R/R_{\mathcal{Q}})\big]\,\big[1 + 2d/R_{\mathcal{Q}}\big]} \tag{A.6}$$

where the r.h.s.'s depend only on the ratios $R/R_{\mathcal{Q}}$ and $d/R_{\mathcal{Q}}$. For a circle concentric to the circular boundary (considered e.g. in section 4.1), $b_\circ = 0$. The expressions in (4.21) have been obtained by solving (A.5) and (A.6) in this special case.

The second map in (A.3) has been also employed to obtain the analytic expressions for the extremal surfaces shown in figure 10 and figure 11.

The second transformation coming from (A.1) that we consider is the one mapping the disk delimited by $\mathcal{C}_{\mathcal{Q}}$ into itself. Let us rename $(x, y, z) = (X', Y', Z')$ in (A.1) for this case, where $Z = Z' = 0$. By imposing that the circle $\mathcal{C}_{\mathcal{Q}}$ is mapped into itself in the coordinates (X', Y'), we find the following two options: either $\boldsymbol{a} = (\pm R_{\mathcal{Q}}\sqrt{(\lambda+1)/\lambda}, 0)$ and $\boldsymbol{c} = (\pm\sqrt{\lambda(1+\lambda)}/R_{\mathcal{Q}}, 0)$ or $\boldsymbol{a} = (\pm R_{\mathcal{Q}}\sqrt{(\lambda-1)/\lambda}, 0)$ and $\boldsymbol{c} = (\mp\sqrt{\lambda(\lambda-1)}/R_{\mathcal{Q}}, 0)$ with $\lambda \geqslant 1$. Since the first option exchanges the interior and the exterior of the disk, we have to select the second one, where the lower or upper choice of the signs move the center of the disk along either $X' > 0$ or $X' < 0$ respectively. Being the disk invariant under a rotation of π about the origin, we can choose one of these two options without loss of generality. Considering e.g. $\boldsymbol{a} = -(R_{\mathcal{Q}}\sqrt{(\lambda-1)/\lambda}, 0)$ and $\boldsymbol{c} = (\sqrt{\lambda(\lambda-1)}/R_{\mathcal{Q}}, 0)$ with $\lambda \geqslant 1$, the resulting transformation maps the circle $(X, Y) = (R_\circ \cos\phi, R_\circ \sin\phi)$ with $R_\circ < R_{\mathcal{Q}}$ into the circle $(X', Y') = (b'_\circ + R'_\circ \cos\phi, R'_\circ \sin\phi)$, where

$$\frac{R'_\circ}{R_{\mathcal{Q}}} = \frac{R_\circ/R_{\mathcal{Q}}}{\lambda\big[1 - (R_\circ/R_{\mathcal{Q}})^2\big] + (R_\circ/R_{\mathcal{Q}})^2} \qquad \frac{b'_\circ}{R_{\mathcal{Q}}} = \frac{\sqrt{(\lambda-1)\lambda}\,\big[1 - (R_\circ/R_{\mathcal{Q}})^2\big]}{\lambda\big[1 - (R_\circ/R_{\mathcal{Q}})^2\big] + (R_\circ/R_{\mathcal{Q}})^2} \tag{A.7}$$

By inverting these relations, one gets $R_\circ/R_{\mathcal{Q}}$ and λ in terms of $R'_\circ/R_{\mathcal{Q}}$ and $b'_\circ/R_{\mathcal{Q}}$. We have checked that, under the transformation that we have constructed, the surface $\mathcal{Q}$ in (A.4) remains unchanged for any value of $\lambda \geqslant 1$.

JHEP08(2018)164

The expression of $R_\circ/R_\mathcal{Q}$ obtained in this way and (4.13) provide the finite term F_A for the holographic entanglement entropy of a disk A inside the disk delimited by $\mathcal{C}_\mathcal{Q}$ in the cases where these two disks are not concentric.

B On the disk concentric to a circular boundary

In this appendix we provide some technical details underlying the derivation of the results reported in section 4.1. Considering the setup introduced in section 2.2.2, we are interested in the extremal surfaces anchored to the boundary of a disk A with radius $R_\circ$ concentric to the disk of radius $R_\mathcal{Q} > R_\circ$, which corresponds to a spatial slice of the spacetime where the BCFT$_3$ is defined. In the following we will adapt to this case the analysis reported in appendix D.2 of [45] about the extremal surfaces anchored to the boundary of an annulus in AdS$_4$/CFT$_3$ (see also [96–99]).

B.1 Extremal surfaces

The invariance under rotations about the vertical axis z of this configuration significantly simplifies the analysis of the corresponding extremal surfaces. Indeed, by introducing the polar coordinates (ρ, ϕ) in the $z = 0$ plane, an extremal surface is determined by the curve $z = z(\rho)$ obtained by taking its section at a fixed angle ϕ. The area functional evaluated on these surfaces becomes

$$\mathcal{A} = 2\pi L^2_{\text{AdS}} \int d\rho\, \rho\, \frac{\sqrt{z'^2 + 1}}{z^2} \tag{B.1}$$

The equation of motion coming from the extremization of this functional reads

$$z\, z'' + \left(1 + z'^2\right)\left(2 + \frac{z\, z'}{\rho}\right) = 0 \tag{B.2}$$

By introducing the variable u and the function $\zeta(\rho)$ as follows

$$z(\rho) = \rho\, \zeta(\rho) \qquad u = \log \rho \qquad \zeta_u = \partial_u \zeta \tag{B.3}$$

the differential equation (B.2) becomes

$$\zeta\, \zeta_u (1 + \partial_\zeta \zeta_u) + \left[1 + (\zeta + \zeta_u)^2\right]\left[2 + \zeta(\zeta + \zeta_u)\right] = 0 \tag{B.4}$$

Integrating this equation, one finds

$$\zeta_{u,\pm} = -\frac{1 + \zeta^2}{\zeta}\left[1 \pm \frac{\zeta}{\sqrt{k(1 + \zeta^2) - \zeta^4}}\right]^{-1} \qquad k > 0 \tag{B.5}$$

where k is the integration constant. By employing that $du = d\zeta/\zeta_u$ and integrating (B.5) starting from an arbitrary initial point, we get

$$\log(\rho/\rho_{\text{in}}) = \int_{u_{\text{in}}}^{u} d\tilde{u} = -\int_{\zeta_{\text{in}}}^{\zeta} \frac{\lambda}{1 + \lambda^2}\left[1 \pm \frac{\lambda}{\sqrt{k(1 + \lambda^2) - \lambda^4}}\right] d\lambda \tag{B.6}$$

JHEP08(2018)164

Since the extremal surfaces are anchored to the boundary of the disk A of radius $R_\circ$ at $z = 0$, from (B.3) we have $\zeta(R_\circ) = 0$ and $u = \log R_\circ$ when $\rho = R_\circ$. Choosing $\rho_{\text{in}} = R_\circ$ and the negative sign within the integrand in (B.6), one finds the first equation in the r.h.s. of (4.1), namely

$$\log(\rho/R_\circ) = -\, q_{-,k}(\zeta) \tag{B.7}$$

where $q_{-,k}(\zeta)$ has been defined in (4.2). The choice of the negative sign in (B.7) will be discussed at the end of this subsection.

The solution (B.7) is well defined as long as the expression under the square root of (B.6) is positive. Such expression vanishes at the point $P_m = (\rho_m, \zeta_m)$, whose coordinates have been reported in (4.3). Following the curve given by (B.7) starting from $(\rho, z) = (R_\circ, 0)$, if it intersects $\mathcal{Q}$ before reaching P_m, then (B.7) fully describes the profile of $\hat{\gamma}_A^{\text{con}}$. Otherwise, (B.7) provides the profile of $\hat{\gamma}_A^{\text{con}}$ until P_m and for the part between P_m and the point $P_* = (\rho_*, \zeta_*)$ (which fully characterises the curve $\partial\hat{\gamma}_{\mathcal{Q}} = \hat{\gamma}_A \cap \mathcal{Q}$ in this case) also the function defined by (B.6) with the positive sign must be employed. In particular, the profile between P_m and P_* reads

$$\log(\rho/R_\circ) = -\, q_{+,k}(\zeta) + q_{+,k}(\zeta_m) - q_{-,k}(\zeta_m) \tag{B.8}$$

which can be written also in the form given by the second expression in the r.h.s. of (4.1), once (4.4) has been used.

In order to justify (4.3) for the coordinates of P_m, let us consider the unit vectors $v_\pm^\mu$ tangent to the radial profile of $\hat{\gamma}_A^{\text{con}}$ along the two branches characterised by $q_{\pm,k}$. They read

$$v_\pm^\mu = \big(v_\pm^\rho, v_\pm^z, v_\pm^\phi\big) = \frac{\pm\, z}{\sqrt{(q'_{\pm,k})^2 + (1 - \zeta\, q'_{\pm,k})^2}} \big(\, q'_{\pm,k}\,, \zeta\, q'_{\pm,k} - 1\,, 0\,\big) \tag{B.9}$$

where $\pm$ refer to the two different branches. At the matching point P_m, the tangent vector field defined by $v_\pm^\mu$ must be continuous, hence a necessary condition is that $g_{\mu\nu}\, v_+^\mu v_-^\nu = 1$ at P_m. From (B.9), one finds that this requirement gives $\zeta^4 = k(1 + \zeta^2)$, whose only admissible solution is the first expression in (4.3).

The boundary condition along the curve $\partial\hat{\gamma}_{\mathcal{Q}} = \hat{\gamma}_A \cap \mathcal{Q}$ provides the parameter k. The condition to impose is that $\hat{\gamma}_A^{\text{con}}$ and $\mathcal{Q}$ intersects orthogonally along $\partial\hat{\gamma}_{\mathcal{Q}}$. This requirement is equivalent to impose that the vector v_μ tangent to $\hat{\gamma}_A^{\text{con}}$ and the vector u_μ tangent to $\mathcal{Q}$ are orthogonal along $\partial\hat{\gamma}_{\mathcal{Q}}$. From (2.24), we find

$$u^\mu = (u^\rho, u^z, u^\phi) = (\cot\alpha - \rho\,\zeta/R_{\mathcal{Q}}\,, \rho/R_{\mathcal{Q}}\,, 0) \tag{B.10}$$

By using (B.9) and (B.10), we find that the orthogonality condition $v^\rho u^\rho + v^z u^z = 0$ at the intersection between $\hat{\gamma}_A^{\text{con}}$ and $\mathcal{Q}$ gives

$$q'_{\pm,k}(\rho_*) = \frac{\rho_*}{R_Q} \tan\alpha \tag{B.11}$$

where $q'_{\pm,k}$ can be read from (4.2) and $\rho_*/R_{\mathcal{Q}}$ can be obtained by specializing (2.25) to P_*. This leads to

$$\frac{\sqrt{\zeta_*^2 + \sin^2\alpha}}{\cos\alpha} = \pm\, \frac{\zeta_*^2}{\sqrt{k(1+\zeta_*^2) - \zeta_*^4}} \tag{B.12}$$

JHEP08(2018)164

that allows us to write ζ_* as a function of k and α. Indeed, the first expression of (4.7) can be found by taking the square of (B.12). The $\pm$ in the r.h.s. of (B.12) correspond to the same choice of sign occurring in (B.11). From (B.12) and $\zeta_* \geqslant 0$, one observes that the orthogonality condition can be satisfied only by $q_{+,k}$ when $\alpha \leqslant \pi/2$, while for $\alpha \geqslant \pi/2$ the orthogonality condition leads to select $q_{-,k}$. Consequently, P_* belongs to the branch described $q_{-,k}$ for $\alpha \leqslant \pi/2$ and to the one characterised by $q_{+,k}$ for $\alpha \geqslant \pi/2$. When $\alpha \to \pi/2$ the l.h.s. of (B.12) diverges; therefore the argument of the square root in the r.h.s. must vanish in this limit. This means that $\zeta_* = \zeta_m$, being ζ_m given in (4.3). Thus, when $\alpha = \pi/2$, the extremal surface $\hat{\gamma}_A^{\text{con}}$ intersects $\mathcal{Q}$ at the matching point P_m of the two branches characterised by $q_{\pm,k}$.

In order to justify the choice of $q_{-,k}$ in (B.7), in the following we show that a contradiction is obtained if $q_{+,k}$ is assumed in (B.7) instead of $q_{-,k}$. In this case the profile of $\hat{\gamma}_A$ can be obtained from (4.1) simply by exchanging the role of $R_\circ$ and R_{aux}, i.e.

$$\rho_\gamma(\theta) = \begin{cases} R_\circ \, e^{-q_{+,k}(\zeta)} \\ R_{\text{aux}} \, e^{-q_{-,k}(\zeta)} \end{cases} \tag{B.13}$$

where now $R_{\mathcal{Q}} > R_\circ > R_{\text{aux}}$. First, let us notice that the maximum value of $z(\zeta)$ is realized in the $q_{+,k}$ branch because from (B.9) we have that $v_\pm^z = 0$ only for the $q_{+,k}$ branch (at $\zeta = \sqrt[4]{k}$). Since $R_{\mathcal{Q}} > R_\circ > R_{\text{aux}}$, this observation leads to conclude that $\mathcal{Q}$ cannot intersect the $q_{-,k}$ branch without intersecting the one described by $q_{+,k}$ (see e.g. the red and the black curves in the top panel of figure 6 as guidance). Thus, the only possibility is that $\mathcal{Q}$ intersects orthogonally the branch described by $q_{+,k}$. In this case, the condition (B.12) leads to $\alpha \leqslant \pi/2$. In order to find a contradiction, let us compare the quantity $\rho^2 + z^2$ for the branch $q_{+,k}$ with the one for $\mathcal{Q}$. For $\mathcal{Q}$ in the range $\alpha \leqslant \pi/2$ we get

$$\rho^2 + z^2 = R_{\mathcal{Q}}^2 \big(1 + \zeta^2\big) Q_\alpha^2 = R_{\mathcal{Q}}^2 \frac{\big(\sqrt{\zeta^2 (\csc\alpha)^2 + 1} + \zeta \cot\alpha\big)^2}{\zeta^2 + 1} \geqslant R_{\mathcal{Q}}^2 \tag{B.14}$$

being Q_α the function introduced in (2.25). As for the $q_{+,k}$ branch, from (B.13) and (B.3) we get $\rho_\gamma^2 + z^2 = (1+\zeta^2)\rho_\gamma^2 = R_\circ^2 \, e^{-2 f_{+,k}}$ where $f_{+,k} \equiv q_{+,k} - \log\sqrt{1+\zeta^2}$ (see (4.5)). Since $f_{+,k} > 0$ for any ζ and $R_\circ > R_{\mathcal{Q}}$, we have $\rho_\gamma^2 + z^2 < R_{\mathcal{Q}}^2$. This means that the branch described by $q_{+,k}$ cannot intersect $\mathcal{Q}$ in the whole range $\alpha \leqslant \pi/2$, ruling out the possibility that $\hat{\gamma}_A$ is described by the profile (B.13).

B.2 Area

In this appendix we evaluate the area of $\hat{\gamma}_A^{\text{con}}$ in two ways: by a direct computation of the integral (B.1) and by specialising the general formula (2.19) to the extremal surfaces $\hat{\gamma}_A^{\text{con}}$.

The analysis performed in section B.1 allows to write the area of $\hat{\gamma}_A^{\text{con}}$ from (B.1) and (B.3) as follows

$$\mathcal{A} = \begin{cases} 2\pi L_{\text{AdS}}^2 \left(\displaystyle\int_{\varepsilon/R_\circ}^{\zeta_m} \frac{d\zeta}{\zeta^2 \sqrt{1+\zeta^2-\zeta^4/k}} + \int_{\zeta_*}^{\zeta_m} \frac{d\zeta}{\zeta^2 \sqrt{1+\zeta^2-\zeta^4/k}} \right) & 0 < \alpha \leqslant \pi/2 \\ 2\pi L_{\text{AdS}}^2 \displaystyle\int_{\varepsilon/R_\circ}^{\zeta_*} \frac{d\zeta}{\zeta^2 \sqrt{1+\zeta^2-\zeta^4/k}} & \pi/2 \leqslant \alpha < \pi \end{cases} \tag{B.15}$$

JHEP08(2018)164

where the UV cutoff ε has been introduced to regularise $\mathcal{A}$, which is a divergent quantity as $\varepsilon \to 0$. Le us recall that $\zeta_* = \zeta_m$ for $\alpha = \pi/2$. The integrals in (B.15) can be explicitly written by using that

$$\int \frac{d\zeta}{\zeta^2 \sqrt{1+\zeta^2-\zeta^4/k}} = -\mathcal{F}_k(\zeta) + \text{const} \tag{B.16}$$

where $\mathcal{F}_k(\zeta)$ has been introduced in (4.14). The expression (4.13) for F_{con} can be found from (B.15) by employing the expansions of $\mathcal{F}_k(\zeta)$ as $\zeta \to 0^+$, which reads

$$\mathcal{F}_k(\zeta) = \frac{1}{\zeta} + \frac{\zeta}{2} + O\left(\zeta^3\right) \tag{B.17}$$

In the remaining part of this appendix we show that the analytic expression for F_{con} given in (4.13) can be obtained also by applying the general formula (2.19) in the special cases of the extremal surfaces $\hat{\gamma}_A^{\text{con}}$.

In order to evaluate the surface integral over $\hat{\gamma}_A$ in (2.19), we need the normal vector $\tilde{n}_\mu$ and the area element $d\tilde{\mathcal{A}}$, which are given respectively by

$$\tilde{n}^\mu = (n^\rho, n^z, n^\phi) = \frac{1}{\sqrt{1+z'^2}}\left(z', -1, 0\right) \qquad d\tilde{\mathcal{A}} = \sqrt{z'^2+1}\,\rho\, d\rho\, d\phi \tag{B.18}$$

The evaluation of the surface integral over $\hat{\gamma}_A$ in (2.19) can be performed by using (B.3) and (B.18), finding

$$\int \frac{(\tilde{n}^z)^2}{z^2}\, d\tilde{\mathcal{A}} = \begin{cases} 2\pi\Big(\mathcal{F}_{k,-}(\zeta_m) + \mathcal{F}_{k,+}(\zeta_m) - \mathcal{F}_{k,+}(\zeta_*)\Big) & 0 < \alpha \leqslant \pi/2 \\ 2\pi\, \mathcal{F}_{k,-}(\zeta_*) & \pi/2 \leqslant \alpha < \pi \end{cases} \tag{B.19}$$

(which can be written as reported in (4.18)) where we have introduced the following functions

$$\mathcal{F}_{k,\pm}(\zeta) \equiv \frac{1}{\sqrt{k}} \int_0^\zeta \frac{\left(\sqrt{k(1+\xi^2)-\xi^4} \pm \xi\right)^2}{(\xi^2+1)^2 \sqrt{k(1+\xi^2)-\xi^4}}\, d\xi \tag{B.20}$$

which can be written in terms of $\mathcal{F}_k(\zeta)$ (see (4.19)). The relation (4.19) has been found by integrating the following identity

$$\frac{\left(\sqrt{k\,(\zeta^2+1)-\zeta^4} \pm \zeta\right)^2}{\sqrt{k}\,(\zeta^2+1)^2 \sqrt{k\,(\zeta^2+1)-\zeta^4}} + \frac{1}{\sqrt{k}}\frac{\partial}{\partial\zeta}\left(\frac{\sqrt{k\,(\zeta^2+1)-\zeta^4} \pm \zeta}{\zeta(\zeta^2+1)}\right) = -\frac{1}{\zeta^2\sqrt{\zeta^2+1-\zeta^4/k}} \tag{B.21}$$

The result of this indefinite integration contains an arbitrary integration constant which can be fixed by taking $\zeta \to 0$ and imposing that both sides of the equation are consistent in this limit (also (B.17) is useful in this computation).

In order to facilitate the recovering of the expression (4.13) for F_{con}, let us observe that, by employing (4.19), the expression (4.18) can be written as follows

$$\int_{\hat{\gamma}} \frac{(\tilde{n}^z)^2}{z^2}\, d\tilde{\mathcal{A}} = F_{\text{con}} - 2\pi\, \frac{\zeta_*^3 + \eta_\alpha \sqrt{k\,(\zeta_*^2+1)-\zeta_*^4}}{\sqrt{k}\,\zeta_*(\zeta_*^2+1)} = F_{\text{con}} - 2\pi\, \frac{\zeta_*^3 - \sqrt{k}\,\cos\alpha}{\sqrt{k}\,\zeta_*(\zeta_*^2+1)} \tag{B.22}$$

JHEP08(2018)164

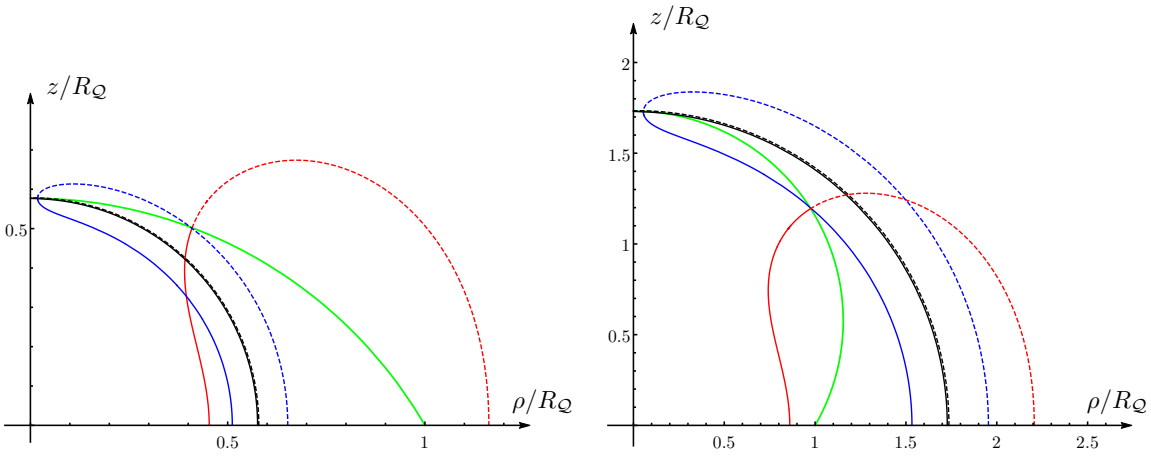

Figure 16. Radial profiles of extremal surfaces $\hat{\gamma}_A^{\rm con}$ intersecting $\mathcal{Q}$ (green curve) orthogonally and anchored to a disk A of radius $R_\circ$ concentric to a circular boundary with radius $R_{\mathcal{Q}}$ (see section 4.1.1). Here $\alpha = 2\pi/3$ (left panel) and $\alpha = \pi/3$ (right panel). Any solid line provides $\hat{\gamma}_A^{\rm con}$ and the dashed line with the same colour gives the radial profile of the corresponding auxiliary surface $\hat{\gamma}_{A,\,\rm aux}^{\rm con}$. Here the values of k associated to $\hat{\gamma}_A^{\rm con}$ (see figure 5) are $k = 1$ (red), $k = 1000$ (blue) and $k = 10^7$ (black). For large k, both $\hat{\gamma}_A^{\rm con}$ and the corresponding $\hat{\gamma}_{A,\,\rm aux}^{\rm con}$ tend to the hemisphere with radius $\cot(\alpha/2)$, which is tangent to $\mathcal{Q}$ at $\rho = 0$.

where in the last step we used the identity $\sqrt{k\,(\zeta_*^2+1)-\zeta_*^4} = -\sqrt{k}\,\eta_\alpha \cos\alpha$, which comes from the explicit form of ζ_* given in the first expression of (4.7).

As for the boundary term in (2.19), the vector $\tilde{b}^\mu$ can be obtained from the vector which is tangent to $\mathcal{Q}$ given in (B.10), finding

$$\tilde{b}^\mu = \big(\tilde{b}^\rho, \tilde{b}^z, \tilde{b}^\phi\big) = \left(\sqrt{1-\left(\frac{\rho_*}{R_{\mathcal{Q}}}\zeta_* \sin\alpha - \cos\alpha\right)^2}\,,\, \frac{\rho_*}{R_{\mathcal{Q}}}\,\zeta_* \sin\alpha - \cos\alpha\,,\, 0\right) \tag{B.23}$$

that coincides with (B.9) evaluated at P_*. From the component $\tilde{b}^z$ in (B.23) and the fact that $d\tilde{s} = \rho_* d\phi$ along $\partial\hat{\gamma}_{\mathcal{Q}}$, we find that the boundary contribution in (2.19) becomes

$$\int_{\partial\hat{\gamma}_{\mathcal{Q}}} \frac{\tilde{b}^z}{z}\, d\tilde{s} = 2\pi\,\frac{\tilde{b}^z}{\zeta_*} = 2\pi\left(\frac{\rho_*}{R_{\mathcal{Q}}}\sin\alpha - \frac{\cos\alpha}{\zeta_*}\right) \tag{B.24}$$

which reduces to (4.20), once the second expression of (4.7) has been employed. Then, plugging (B.22) and (4.20) into (2.19), one obtains

$$F_A = F_{\rm con} - 2\pi\,\frac{\zeta_*^2 - \sqrt{k\big[\zeta_*^2 + (\sin\alpha)^2\big]}}{\sqrt{k}\,(\zeta_*^2+1)} \tag{B.25}$$

where, by using (B.12) and the identity given in the text below (B.22), it is straightforward to observe that the numerator in the r.h.s. vanishes.

B.3 Limiting regimes

In the remaining part of this appendix we provide some technical details about the limiting regimes $k \to 0$ and $k \to \infty$ of the analytic expressions for $R_\circ/R_{\mathcal{Q}}$ and $F_{\rm con}$ (see (4.9)

JHEP08(2018)164

and (4.13) respectively). The results of this analysis have been reported in (4.10), (4.11) and (4.16).

As for the ratio $R_\circ/R_{\mathcal{Q}}$, whose analytic expression is (4.9) with $\chi(\zeta_m)$ given by (4.4), we have to study $q_{\pm,k}(\zeta_*)$ and $q_{\pm,k}(\zeta_m)$ in these limiting regimes.

In order to find $q_{\pm,k}(\zeta_*)$ for $k \to 0$, let us write $q_{\pm,k}(\zeta_*)$ from the integral (4.2) evaluated for $\zeta = \zeta_*$ (see (4.7)) and adopt $\zeta_*\lambda$ as integration variable because it leads us to a definite integral whose extrema are 0 and 1. By first expanding the integrand of the resulting formula and then integrating separately the terms of the expansion, we find

$$q_{\pm,k}(\zeta_*) = \pm\Big[\mathbb{E}\big(\arcsin(\sqrt{\sin\alpha}\,)\big|-1\big) - \mathbb{F}\big(\arcsin(\sqrt{\sin\alpha}\,)\big|-1\big)\Big]\sqrt[4]{k} + \frac{\sin\alpha}{2}\sqrt{k} + O\big(k^{3/4}\big) \tag{B.26}$$

Adapting this analysis to $q_{\pm,k}(\zeta_m)$, we obtain

$$q_{\pm,k}(\zeta_m) = \pm\Big(\mathbb{E}(-1) - \mathbb{K}(-1)\Big)\sqrt[4]{k} + \frac{\sqrt{k}}{2} + \mathcal{O}(k^{3/4}) \tag{B.27}$$

By employing the expansions (B.26) and (B.27) into (4.4) and (4.9), one gets the result (4.10).

As for the $k \to \infty$ regime, for the integrals (4.2) we have

$$q_{\pm,k}(\zeta) = \frac{1}{2}\log(1+\zeta^2) + \mathcal{O}\big(1/\sqrt{k}\,\big) \tag{B.28}$$

Moreover, from (4.3) and (4.7) notice that both ζ_* and ζ_m diverge, with $\zeta_*/\zeta_m \to 1$. Thus, being $\zeta = z/\rho$ with finite z for the surfaces that we are considering, we have that $\rho_* \to 0$ and $\rho_m \to 0$. These observations tell us that, in the regime of large k, the two branches in (4.1) become the same arc of circle from $\rho = R_\circ$ to $\rho = 0$ (see the black curves in figure 16). In particular, we have $R_{\text{aux}} \to R_\circ$. By taking the limit of (2.25) for large ζ and employing the identity $\cot\alpha + \csc\alpha = \cot(\alpha/2)$, one finds that $P_* = P_m = R_{\mathcal{Q}}(0, \cot(\alpha/2))$ in this regime. Then, being the limiting curve a circle of radius $R_\circ$, we have that $R_{\mathcal{Q}}\cot(\alpha/2) = R_\circ$. The latter relation provides (4.11), which is the asymptotic behaviour of the curves in figure 5. In figure 16 we show some examples of extremal surfaces (which are not necessarily the global minimum of the area) as k increases for two fixed values of α, highlighting the limit of large k, which corresponds to the black curves.

In order to study the subleading term of area of the extremal surfaces as $k \to 0$ or $k \to \infty$, we find it convenient to employ the expressions (2.19), (4.18) and (4.20). Indeed, since $\mathcal{F}_{k,\pm}(\zeta_*)$ and $\mathcal{F}_{k,\pm}(\zeta_m)$ can be written through the integral representation (B.20) of the functions $\mathcal{F}_{k,\pm}(\zeta)$, we can adapt the above analysis to this case (e.g. for $\mathcal{F}_{k,\pm}(\zeta_*)$ one first introduces $\zeta_*\xi$ as integration variable, obtaining a definite integral between 0 and 1, then expands the integrand of the resulting expression and finally integrates the various terms of the expansion), finding

$$\begin{aligned}\mathcal{F}_{k,\pm}(\zeta_*) = {}& \frac{1}{\sqrt[4]{k}}\Big[\mathbb{E}\big(\arcsin(\sqrt{\sin\alpha}\,)\big|-1\big) - \mathbb{F}\big(\arcsin(\sqrt{\sin\alpha}\,)\big|-1\big)\Big] \pm \sin\alpha \\ & + \left(\frac{1}{4}\,\mathbb{F}\big(\arcsin(\sqrt{\sin\alpha}\,)\big|-1\big) - \eta_\alpha\cos\alpha\sqrt{\sin\alpha}\right)\sqrt[4]{k} + \mathcal{O}\big(\sqrt{k}\,\big)\end{aligned} \tag{B.29}$$

JHEP08(2018)164

and

$$\mathcal{F}_{k,\pm}(\zeta_m) = \frac{\mathbb{E}(-1) - \mathbb{K}(-1)}{\sqrt[4]{k}} \pm 1 + \frac{\mathbb{K}(-1)}{4}\sqrt[4]{k} + \mathcal{O}(\sqrt{k}) \tag{B.30}$$

By using these expansions into (4.18), together with (4.20) into (2.19), the expansion (4.16) is obtained.

The asymptotic value 2π for large k in figure 7 can be found by employing that the profile of $\hat{\gamma}_A^{\rm con}$ in this regime is the one of the hemisphere in $\mathbb{H}_3$ anchored to $R_\circ$ (see also the appendix D in [45]). Since the finite term of the area for the hemisphere in $\mathbb{H}_3$ is 2π, we can easily conclude that the curves in figure 7 tend to this value as $k \to \infty$.

C On the infinite wedge adjacent to the boundary

In the gravitational setup described in section 2.2.1, let us consider an infinite wedge A in (6.7), which is adjacent to the flat boundary and whose opening angle is ω. As for the corresponding holographic entanglement entropy, by a direct evaluation of the area $\mathcal{A}[\hat{\gamma}_\varepsilon]$, it has been found that (1.5) holds and the analytic expression of the corner function $F_\alpha(\omega)$ has been found [87]. In this appendix we provide some technical details underlying the discussion of section 6.2, where we have shown that the analytic expression for $F_\alpha(\omega)$ can be recovered also through (2.22).

Let us consider first the line integral over $\partial\hat{\gamma}_{\mathcal{Q}}$ occurring in (2.22). The curve $\partial\hat{\gamma}_{\mathcal{Q}}$ is a line on $\mathcal{Q}$ which can be parameterised as follows [87]

$$\partial\hat{\gamma}_{\mathcal{Q}}: \quad (z,x,y) = \rho\,\big(-\sin\phi_*\tan\alpha\,,\,\sin\phi_*\,,\,\cos\phi_*\big) \qquad 0 \leqslant \rho \leqslant L \tag{C.1}$$

where ϕ_* is the angular coordinate characterising the projection of $\partial\hat{\gamma}_{\mathcal{Q}}$ on the $z=0$ plane. The line element $d\tilde{s}$ induced by the flat metric in (2.22) reads

$$d\tilde{s} = \sqrt{x'^2+y^2+z'^2}\,d\rho = \frac{\sqrt{x'^2+\cos^2\alpha\,y'^2}\,d\rho}{|\cos\alpha|} = -\frac{\eta_\alpha}{\cos\alpha}\sqrt{\sin^2\phi_* + \cos^2\alpha\,\cos^2\phi_*}\,d\rho \tag{C.2}$$

By employing (C.1) and (C.2), the line integral over $\partial\hat{\gamma}_{\mathcal{Q}}$ in (2.22) becomes

$$-\cos\alpha\int_{\partial\hat{\gamma}_{\mathcal{Q}}}\frac{1}{z}\,d\tilde{s} = -\cot\alpha\int_{\rho_\varepsilon}^{L}\frac{\sqrt{1+\cos^2\alpha\cot^2\phi_*}}{\rho}\,d\rho \tag{C.3}$$

where $\text{sign}(\sin\phi_*) = \eta_\alpha$ has been used. The integral in the r.h.s. of (C.3) has been regularised by introducing the lower extremum ρ_ε, which is defined by the condition $\varepsilon = -\rho_\varepsilon\sin\phi_*\tan\alpha$, obtained by intersecting $\partial\hat{\gamma}_{\mathcal{Q}}$ in (C.1) with the plane $z=\varepsilon$. The radial integral (C.3) can be easily evaluated, finding (6.18) at leading order as $\varepsilon \to 0$.

In order to compute the surface integral over $\hat{\gamma}_\varepsilon$ in (2.22), we need the unit normal vector $\tilde{n}_\nu$. Up to a normalization factor, this vector is given by the gradient of the equation $\mathcal{C} = z - \rho/q(\phi) = 0$, where $q(\phi)$ has been introduced in (6.8) and characterises the minimal surface. By imposing the normalization condition $\tilde{n}_\mu\tilde{n}^\mu = 1$, we get

$$\tilde{n}_\mu = \frac{1}{\sqrt{q^4+q^2+q'^2}}\,\big(q^2, -q, q'\rho\big) \tag{C.4}$$

JHEP08(2018)164

where the index μ spans the cylindrical coordinates (z, ρ, ϕ) defined in section 6.2. The first derivative q' of q with respect to ϕ can be expressed in term of q and q_0 with the help of the integral of motion associated to the cyclic coordinate ϕ [22, 23, 87], finding that

$$\frac{(q')^2}{q^2} = (q^2+1)\left(\frac{q^4+q^2}{q_0^4+q_0^2} - 1\right) \qquad q \geqslant q_0 \tag{C.5}$$

By using (C.4) and (C.5) the integrand of the integral over $\hat{\gamma}_\varepsilon$ in (2.22) can be written as

$$\frac{(\tilde{n}^z)^2}{z^2} = \frac{q^6}{\rho^2\,(q^4+q^2+q'^2)} = \frac{q^2(q_0^4+q_0^2)}{(q^2+1)^2\rho^2} \tag{C.6}$$

In terms of the cylindrical coordinates introduced in section 6.2, the area element induced by the flat metric reads

$$d\tilde{\mathcal{A}} = \frac{\sqrt{q'^2+q^4+q^2}}{q^2}\,\rho\,d\rho\,d\phi = \frac{q^2+1}{\sqrt{q_0^4+q_0^2}}\,\rho\,d\rho\,d\phi \tag{C.7}$$

Plugging (C.6) and (C.7) into the surface integral over $\hat{\gamma}_\varepsilon$ in (2.22), it reduces to the following double integral

$$\int_{\hat{\gamma}_\varepsilon} \frac{(\tilde{n}^z)^2}{z^2}\,d\tilde{\mathcal{A}} = \int_{\rho_{\min}}^{\rho_{\max}} \frac{1}{\rho}\,d\rho \int_{\phi_*}^{\omega_\varepsilon} \frac{q^2\sqrt{q_0^4+q_0^2}}{q^2+1}\,d\phi \tag{C.8}$$

The integration domain in the angular integral is defined by the angle ϕ_* characterising $\partial\hat{\gamma}_{\mathcal{Q}}$ and $\omega_\varepsilon \equiv \omega - \delta_\varepsilon$, where $\delta_\varepsilon \sim 0$ is the angle between the border of the wedge at $\phi = \omega$ and the straight line in the $z = 0$ half plane connecting the tip of the wedge to the intersection point between the circle given by $\rho = \rho_{\max}$ and the projection of $\hat{\gamma}_A \cap \{z = \varepsilon\}$ on the half plane $z = 0$. In the radial direction we have introduced the large cutoff $\rho_{\max}$ to regulate the infrared divergences of this integral, while the lower extremum $\rho_{\min} = q_0\,\varepsilon$ (being q_0 the minimum value of q) controls the UV behaviour. The cutoff $\rho_{\max}$ is related to L in (6.7) and to δ_ε through the relation $L = \rho_{\max}\cos\delta_\varepsilon$, and to ε through the condition

$$\rho_{\max} = \varepsilon\,q(\omega - \delta_\varepsilon) \tag{C.9}$$

In order to perform the angular integration in (C.8), it is convenient to change the integration variable from ϕ to q. However, since q is not monotonic as function of ϕ for some values of α, we have to split the integral into two separate contributions (depending on the sign of $\cot\alpha$) as follows

$$\int_{\hat{\gamma}} \frac{(\tilde{n}^z)^2}{z^2}\,d\tilde{\mathcal{A}} = \int_{\rho_{\min}}^{\rho_{\max}} \frac{d\rho}{\rho}\left(\int_{q_0}^{\rho/\varepsilon} \frac{q^2\sqrt{q_0^4+q_0^2}}{(q^2+1)\,q'}\,dq - \eta_\alpha \int_{q_0}^{q_*} \frac{q^2\sqrt{q_0^4+q_0^2}}{(q^2+1)\,q'}\,dq\right) \tag{C.10}$$

where (C.5) can be used to express q'. By introducing the integration variable $\tilde{\rho} = \rho/\varepsilon$ in the radial integration, we get

$$\int_{\hat{\gamma}} \frac{(\tilde{n}^z)^2}{z^2}\,d\tilde{\mathcal{A}} = \int_{\rho_{\min}/\varepsilon}^{\rho_{\max}/\varepsilon} \frac{d\tilde{\rho}}{\tilde{\rho}}\left(\int_{\rho_{\min}/\varepsilon}^{\tilde{\rho}} \frac{q^2\sqrt{q_0^4+q_0^2}}{(q^2+1)\,q'}\,dq - \eta_\alpha \int_{q_0}^{q_*} \frac{q^2\sqrt{q_0^4+q_0^2}}{(q^2+1)\,q'}\,dq\right) \equiv I_1 - \eta_\alpha\,I_2 \tag{C.11}$$

JHEP08(2018)164

where I_2 is defined as the integral multiplying η_α, while I_1 is the remaining one. Considering I_1 first, in order to single out the logarithmic divergence we exchange the order of integration between $\tilde{\rho}$ and q, finding that

$$I_1 = \int_{\rho_{\min}/\varepsilon}^{\rho_{\max}/\varepsilon} \frac{q^2\sqrt{q_0^4+q_0^2}}{(q^2+1)\,q'}\,dq \int_q^{\rho_{\max}/\varepsilon} \frac{d\tilde{\rho}}{\tilde{\rho}} \tag{C.12}$$

Now the integration over ρ can be easily performed, obtaining

$$I_1 = \int_{\rho_{\min}/\varepsilon}^{\rho_{\max}/\varepsilon} \sqrt{q_0^4+q_0^2}\left(\frac{q^2}{(q^2+1)\,q'}\,\log(\rho_{\max}/\varepsilon) - \frac{q^2\log q}{(q^2+1)\,q'}\right) dq \tag{C.13}$$

Since L is large, the dominant contribution comes from the first integral (the second one is finite in this limit). In particular, we find

$$I_1 = \left(\int_{q_0}^{+\infty} \frac{q^2\sqrt{q_0^4+q_0^2}}{(q^2+1)\,q'}\,dq\right)\log(L/\varepsilon) + \cdots \tag{C.14}$$

where the integral multiplying the logarithmic divergence provides an integral representation of the function $F(q_0)$ given in (6.16) in terms of elliptic function, i.e.

$$\int_{q_0}^{+\infty} \frac{q^2\sqrt{q_0^4+q_0^2}}{(q^2+1)\,q'}\,dq = F(q_0) \tag{C.15}$$

The second integral I_2 in (C.11) can be also calculated in closed form in terms of elliptic functions. Expanding the result for large L, one finds that the dominant contribution is the following logarithmic divergence

$$I_2 = \left(S(q_*,q_0) + \sqrt{\frac{\left(q_*^2-q_0^2\right)\left(q_*^2+q_0^2+1\right)}{q_*^2+1}}\right)\log(L/\varepsilon) + \cdots \tag{C.16}$$

where $S(q_*,q_0)$ has been defined in (6.21).

Combining (C.14) and (C.16) into (C.11), we get the logarithmic divergence provided by the surface integral over $\hat{\gamma}_\varepsilon$ in (2.22), which is given by (6.19) and (6.20). By taking into account also the logarithmic divergence provided by the line integral over $\partial\hat{\gamma}_{\mathcal{Q}}$ (see (6.18)), for the coefficient of $\log(L/\varepsilon)$ in the subleading term F_A we find

$$\begin{aligned} F_\alpha(q_0) \,=\, & F(q_0) - \eta_\alpha S(q_*(\alpha,q_0),q_0) \\ & - \eta_\alpha\sqrt{\frac{\left(q_*^2-q_0^2\right)\left(q_*^2+q_0^2+1\right)}{q_*^2+1}} - \sqrt{1+\cos^2\alpha\cot^2\phi_*(\alpha,q_0)}\,\cot\alpha \end{aligned} \tag{C.17}$$

where the last two terms in (C.17) cancel, once the explicit expressions for $\phi_*(\alpha,q_0)$ and $q_*(\alpha,q_0)$ (see (6.13) and (6.14)) have been used. Hence, $F_\alpha(q_0)$ simplifies to

$$F_\alpha(q_0) = F(q_0) - \eta_\alpha\, S(q_*(\alpha,q_0),q_0) \tag{C.18}$$

In order to show that (C.18) coincides with (6.15), we have to prove that $S(q_*,q_0) = -\,\mathcal{G}(q_*,q_0)$. This follows from two observations that can be easily verified: the function obtained by taking the derivative of (6.17) with respect to q and then evaluating it for $q=q_*$ is the opposite of the derivative of (6.21) with respect to q_* and $S(q_0,q_0) = \mathcal{G}(q_0,q_0) = 0$ for any α.

JHEP08(2018)164

D Auxiliary surfaces

In this appendix we discuss a way to relate an extremal surface $\hat{\gamma}_A$ anchored to the entangling curve of a region A in $AdS_4/BCFT_3$ to an extremal surface in AdS_4/CFT_3 anchored to a corresponding entangling curve in $\mathbb{R}^2$, which is the spatial slice of the CFT_3, being the gravitational background the one obtained by removing $\mathcal{Q}$. We will discuss only the simplest cases where a spatial section of the gravitational spacetimes is given by $\mathbb{H}_3$ or part of it.

In $AdS_4/BCFT_3$ setups of section 2.2.1 and section 2.2.2, if the extremal surface $\hat{\gamma}_A$ does not intersect the boundary $\mathcal{Q}$, then it can be also seen as an extremal surface in $\mathbb{H}_3$. Instead, when $\hat{\gamma}_A$ intersects orthogonally $\mathcal{Q}$ along some curve $\partial\hat{\gamma}_{\mathcal{Q}}$ (since we mainly consider extremal surfaces intersecting $\mathcal{Q}$ orthogonally, in this appendix we denote by $\hat{\gamma}_A$ the surfaces $\hat{\gamma}_A^{\text{con}}$ of section 4.1.1), we can consider the unique auxiliary surface $\hat{\gamma}_{A,\,\text{aux}}$ such that $\hat{\gamma}_A \cup \hat{\gamma}_{A,\,\text{aux}}$ is an extremal surface in $\mathbb{H}_3$ and $\hat{\gamma}_{A,\,\text{aux}}$ is orthogonal to $\mathcal{Q}$ along $\partial\hat{\gamma}_{\mathcal{Q}}$. The extremal surface $\hat{\gamma}_A \cup \hat{\gamma}_{A,\,\text{aux}}$ in $\mathbb{H}_3$ is anchored to ∂A_{aux} of some auxiliary region A_{aux} in the plane $\mathbb{R}^2$ at $z = 0$.

As first example, let us consider an infinite strip A of width ℓ adjacent to the flat boundary in the setup of section 2.2.1. In this case, A_{aux} is a strip whose width is [87]

$$\ell_{\text{aux}} = \frac{2\sqrt{\pi}\,\Gamma(\frac{3}{4})}{\Gamma(\frac{1}{4})\,\mathfrak{g}(\alpha)}\,\ell \tag{D.1}$$

where $\mathfrak{g}(\alpha)$ has been defined in (3.2). We remark that the strip A is not necessarily a subset of the A_{aux}. Indeed, for $\alpha \leqslant \alpha_{c,\,\text{aux}}$ we have that $A \subseteq A_{\text{aux}}$, while $A_{\text{aux}} \subseteq A$ when $\alpha \geqslant \alpha_{c,\,\text{aux}}$. The value of $\alpha_{c,\,\text{aux}}$ is defined by imposing that $\ell_{\text{aux}} = \ell$, which gives $\mathfrak{g}(\alpha_{c,\,\text{aux}}) = 2\sqrt{\pi}\,\Gamma(\frac{3}{4})/\Gamma(\frac{1}{4})$. From the latter result and (3.2), for $\alpha \in (0, \pi)$ we have

$$\mathfrak{g}(\pi - \alpha) = \mathfrak{g}(\alpha_{c,\,\text{aux}}) - \mathfrak{g}(\alpha) \tag{D.2}$$

By specifying this relation to $\alpha = \alpha_c$, the critical value of α defined in section 3 as the zero of $\mathfrak{g}(\alpha)$, one finds that $\alpha_{c,\,\text{aux}} = \pi - \alpha_c$.

Another interesting configuration is given by a disk A disjoint from the boundary which is either flat or circular (see section 4). In these cases the extremal surfaces $\hat{\gamma}_{A,\,\text{aux}} \cup \hat{\gamma}_A$ are anchored to a pair of circles and they have been studied in [45, 96–99] for the gravitational background given by $\mathbb{H}_3$. In the setup of section 2.2.2, considering a disk A of radius $R_\circ$ concentric to a circular boundary of radius $R_{\mathcal{Q}}$ as in section 4.1, we have that $\hat{\gamma}_A \cup \hat{\gamma}_{A,\,\text{aux}}$ is an extremal surface in $\mathbb{H}_3$ anchored to the boundary of an annulus characterised by the radii $R_\circ$ and $R_{\text{aux}} > R_\circ$ (see also (4.1)). The ratio $R_\circ/R_{\text{aux}}$ is given by (4.4).

Partitioning $\mathbb{H}_3$ into the part $\mathcal{M}_3$, introduced in section 2.1, and its complement $\overline{\mathcal{M}}_3$, we have that part of $\hat{\gamma}_{A,\,\text{aux}}$ belongs to $\overline{\mathcal{M}}_3$ because $\hat{\gamma}_{A,\,\text{aux}} \perp \mathcal{Q}$ along $\partial\hat{\gamma}_{\mathcal{Q}}$. It can happen that the intersection between $\hat{\gamma}_{A,\,\text{aux}}$ and $\mathcal{M}_3$ is non trivial (see e.g. the right panel in figure 10). In figure 17 we show the ratio $R_{\text{aux}}/R_{\mathcal{Q}}$ as function of k for some values of α. Let us introduce the critical value $\alpha_{c,\,\text{aux}}$ such that $R_{\text{aux}}/R_{\mathcal{Q}} < 1$ for every k at fixed $\alpha > \alpha_{c,\,\text{aux}}$. For this configuration we observe numerically that $\alpha_{c,\,\text{aux}} = \pi - \alpha_c$, namely the same relation found above for the strip adjacent to the flat boundary. Three qualitatively

JHEP08(2018)164

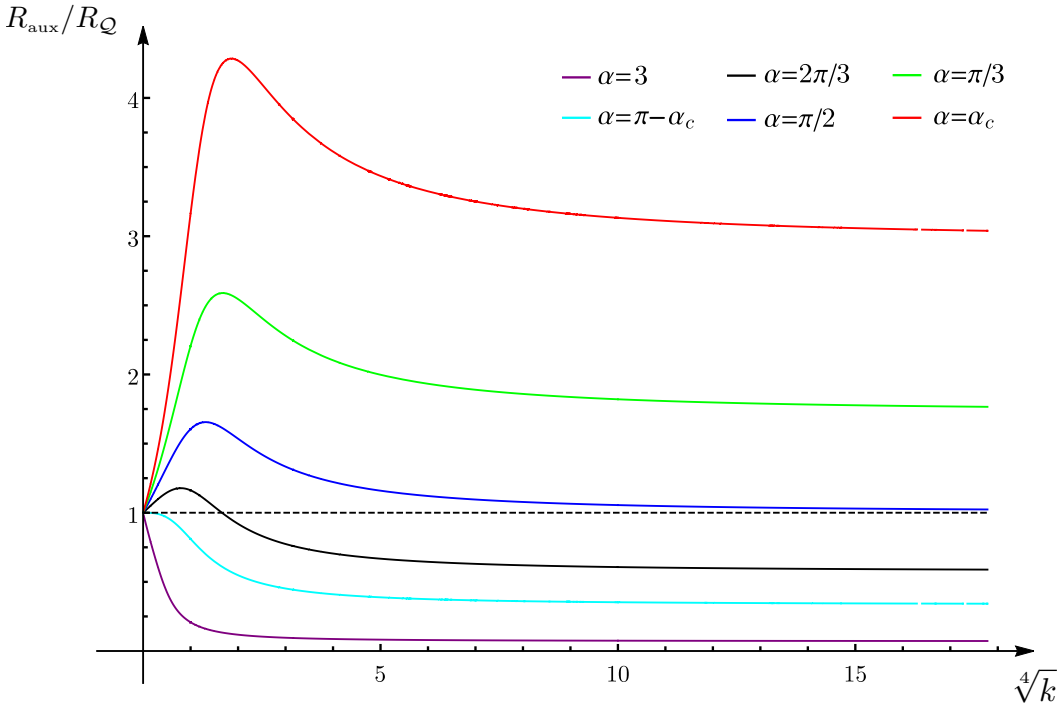

Figure 17. The ratio $R_{\rm aux}/R_{\mathcal{Q}}$ for a disk A concentric to a circular boundary of radius $R_{\mathcal{Q}}$ (see section 4.1.1 and appendix D) in terms of the parameter k, obtained by combining (4.4) and (4.9). For $\alpha \geqslant \pi - \alpha_c$ we have that $R_{\rm aux} \leqslant R_{\mathcal{Q}}$, therefore part of $\hat{\gamma}_{A,\,\rm aux}$ belongs to the gravitational spacetime bounded by $\mathcal{Q}$.

different situations are observed (see figure 17): when $\alpha \leqslant \pi/2$ we have $R_{\rm aux} > R_{\mathcal{Q}}$ and $\hat{\gamma}_{A,\,\rm aux} \cap \mathcal{M}_3 = \emptyset$, for $\pi/2 \leqslant \alpha \leqslant \pi - \alpha_c$ it is possible that $\hat{\gamma}_{A,\,\rm aux} \cap \mathcal{M}_3 \neq \emptyset$, while when $\alpha \geqslant \pi - \alpha_c$ we have that some part of $\hat{\gamma}_{A,\,\rm aux}$ always belongs to $\mathcal{M}_3$ because $R_{\rm aux} < R_{\mathcal{Q}}$.

By employing the map (A.3), analogous considerations can be done for the extremal surfaces anchored to a disk A disjoint from a flat boundary, considered in section 4.2. The extremal surface is anchored to a pair of circles in $\mathbb{R}^2$ and one of them is ∂A. For this configuration explicit examples are given in figure 10 and figure 11, where $\hat{\gamma}_{A,\,\rm aux}$ are the shaded surfaces.

As for the auxiliary surfaces corresponding to the extremal surfaces anchored to the singular domains considered in section 6 we refer the reader to the exhaustive discussion reported in [87]. Here we just recall that for the half disk adjacent to the boundary (see section 6.1) $\hat{\gamma}_A \cup \hat{\gamma}_{A,\,\rm aux}$ is the hemisphere and for the infinite wedge adjacent to the boundary (see section 6.2) $\hat{\gamma}_A \cup \hat{\gamma}_{A,\,\rm aux}$ is the extremal surface anchored to an infinite wedge in $\mathbb{R}^2$ found in [22, 23].

JHEP08(2018)164

References

[1] L. Amico, R. Fazio, A. Osterloh and V. Vedral, *Entanglement in many-body systems*, *Rev. Mod. Phys.* **80** (2008) 517 [quant-ph/0703044] [INSPIRE].

[2] J. Eisert, M. Cramer and M.B. Plenio, *Area laws for the entanglement entropy — a review*, *Rev. Mod. Phys.* **82** (2010) 277 [arXiv:0808.3773] [INSPIRE].

[3] P. Calabrese, J. Cardy and B. Doyon, *Entanglement entropy in extended quantum systems*, *J. Phys.* **A 42** (2009) 500301.

[4] S.N. Solodukhin, *Entanglement entropy of black holes*, *Living Rev. Rel.* **14** (2011) 8 [arXiv:1104.3712] [INSPIRE].

[5] M. Rangamani and T. Takayanagi, *Holographic Entanglement Entropy*, *Lect. Notes Phys.* **931** (2017) pp.1 [arXiv:1609.01287] [INSPIRE].

[6] S. Ryu and T. Takayanagi, *Holographic derivation of entanglement entropy from AdS/CFT*, *Phys. Rev. Lett.* **96** (2006) 181602 [hep-th/0603001] [INSPIRE].

[7] S. Ryu and T. Takayanagi, *Aspects of Holographic Entanglement Entropy*, *JHEP* **08** (2006) 045 [hep-th/0605073] [INSPIRE].

[8] V.E. Hubeny, M. Rangamani and T. Takayanagi, *A covariant holographic entanglement entropy proposal*, *JHEP* **07** (2007) 062 [arXiv:0705.0016] [INSPIRE].

[9] M. Freedman and M. Headrick, *Bit threads and holographic entanglement*, *Commun. Math. Phys.* **352** (2017) 407 [arXiv:1604.00354] [INSPIRE].

[10] M. Headrick and V.E. Hubeny, *Riemannian and Lorentzian flow-cut theorems*, *Class. Quant. Grav.* **35** (2018) 105012 [arXiv:1710.09516] [INSPIRE].

[11] M. Headrick and T. Takayanagi, *A holographic proof of the strong subadditivity of entanglement entropy*, *Phys. Rev.* **D 76** (2007) 106013 [arXiv:0704.3719] [INSPIRE].

[12] V.E. Hubeny, H. Maxfield, M. Rangamani and E. Tonni, *Holographic entanglement plateaux*, *JHEP* **08** (2013) 092 [arXiv:1306.4004] [INSPIRE].

[13] S.N. Solodukhin, *The conical singularity and quantum corrections to entropy of black hole*, *Phys. Rev.* **D 51** (1995) 609 [hep-th/9407001] [INSPIRE].

[14] S.N. Solodukhin, *On 'Nongeometric' contribution to the entropy of black hole due to quantum corrections*, *Phys. Rev.* **D 51** (1995) 618 [hep-th/9408068] [INSPIRE].

[15] S.N. Solodukhin, *One loop renormalization of black hole entropy due to nonminimally coupled matter*, *Phys. Rev.* **D 52** (1995) 7046 [hep-th/9504022] [INSPIRE].

[16] R.C. Myers and A. Sinha, *Seeing a c-theorem with holography*, *Phys. Rev.* **D 82** (2010) 046006 [arXiv:1006.1263] [INSPIRE].

[17] R.C. Myers and A. Sinha, *Holographic c-theorems in arbitrary dimensions*, *JHEP* **01** (2011) 125 [arXiv:1011.5819] [INSPIRE].

[18] D.L. Jafferis, I.R. Klebanov, S.S. Pufu and B.R. Safdi, *Towards the F-Theorem: $N = 2$ Field Theories on the Three-Sphere*, *JHEP* **06** (2011) 102 [arXiv:1103.1181] [INSPIRE].

[19] I.R. Klebanov, S.S. Pufu and B.R. Safdi, *F-Theorem without Supersymmetry*, *JHEP* **10** (2011) 038 [arXiv:1105.4598] [INSPIRE].

[20] H. Liu and M. Mezei, *A refinement of entanglement entropy and the number of degrees of freedom*, *JHEP* **04** (2013) 162 [arXiv:1202.2070] [INSPIRE].

JHEP08(2018)164

[21] H. Casini and M. Huerta, *On the RG running of the entanglement entropy of a circle*, *Phys. Rev.* **D 85** (2012) 125016 [arXiv:1202.5650] [INSPIRE].

[22] N. Drukker, D.J. Gross and H. Ooguri, *Wilson loops and minimal surfaces*, *Phys. Rev.* **D 60** (1999) 125006 [hep-th/9904191] [INSPIRE].

[23] N. Drukker and V. Forini, *Generalized quark-antiquark potential at weak and strong coupling*, *JHEP* **06** (2011) 131 [arXiv:1105.5144] [INSPIRE].

[24] H. Casini and M. Huerta, *Universal terms for the entanglement entropy in 2+1 dimensions*, *Nucl. Phys.* **B 764** (2007) 183 [hep-th/0606256] [INSPIRE].

[25] H. Casini, M. Huerta and L. Leitao, *Entanglement entropy for a Dirac fermion in three dimensions: Vertex contribution*, *Nucl. Phys.* **B 814** (2009) 594 [arXiv:0811.1968] [INSPIRE].

[26] T. Hirata and T. Takayanagi, *AdS/CFT and strong subadditivity of entanglement entropy*, *JHEP* **02** (2007) 042 [hep-th/0608213] [INSPIRE].

[27] P. Bueno, R.C. Myers and W. Witczak-Krempa, *Universality of corner entanglement in conformal field theories*, *Phys. Rev. Lett.* **115** (2015) 021602 [arXiv:1505.04804] [INSPIRE].

[28] P. Bueno and R.C. Myers, *Corner contributions to holographic entanglement entropy*, *JHEP* **08** (2015) 068 [arXiv:1505.07842] [INSPIRE].

[29] T. Faulkner, R.G. Leigh and O. Parrikar, *Shape Dependence of Entanglement Entropy in Conformal Field Theories*, *JHEP* **04** (2016) 088 [arXiv:1511.05179] [INSPIRE].

[30] L. Bianchi, M. Meineri, R.C. Myers and M. Smolkin, *Rényi entropy and conformal defects*, *JHEP* **07** (2016) 076 [arXiv:1511.06713] [INSPIRE].

[31] V.E. Hubeny, *Extremal surfaces as bulk probes in AdS/CFT*, *JHEP* **07** (2012) 093 [arXiv:1203.1044] [INSPIRE].

[32] I.R. Klebanov, T. Nishioka, S.S. Pufu and B.R. Safdi, *On Shape Dependence and RG Flow of Entanglement Entropy*, *JHEP* **07** (2012) 001 [arXiv:1204.4160] [INSPIRE].

[33] A. Allais and M. Mezei, *Some results on the shape dependence of entanglement and Rényi entropies*, *Phys. Rev.* **D 91** (2015) 046002 [arXiv:1407.7249] [INSPIRE].

[34] M. Mezei, *Entanglement entropy across a deformed sphere*, *Phys. Rev.* **D 91** (2015) 045038 [arXiv:1411.7011] [INSPIRE].

[35] G. Thomsen, *Über Konforme Geometrie, I: Grundlagen der Konformen Flächentheorie*, *Abn. Math. Sem. Hamburg* (1923) 31.

[36] W. Blaschke, *Vorlesungen über Differentialgeometrie III*, Springer, Berlin, Germany (1929).

[37] T. Willmore, *Note on embedded surfaces*, *An. St. Univ. Iasi sIa Mat.* **B 11B** (1965) 493.

[38] T. Willmore, *Mean curvature of Riemannian immersions*, *J. Lond. Math. Soc.* **3** (1971) 307.

[39] T. Willmore, *Riemannian geometry*, Oxford University Press, New York, U.S.A., (1992).

[40] M. Babich and A. Bobenko, *Willmore tori with umbilic lines and minimal surfaces in hyperbolic space*, *Duke Math. J.* **72** (1993) 151.

[41] S. Alexakis and R. Mazzeo, *Renormalized Area and Properly Embedded Minimal Surfaces in Hyperbolic 3-Manifolds*, *Commun. Math. Phys.* **297** (2010) 621 [arXiv:0802.2250].

JHEP08(2018)164

[42] P. Fonda, D. Seminara and E. Tonni, *On shape dependence of holographic entanglement entropy in AdS_4/CFT_3*, *JHEP* **12** (2015) 037 [arXiv:1510.03664] [INSPIRE].

[43] K. Brakke, *The Surface Evolver*, *Exper. Math.* **1** (1992) 141.

[44] *Surface Evolver* program: http://www.susqu.edu/brakke/evolver/evolver.html.

[45] P. Fonda, L. Giomi, A. Salvio and E. Tonni, *On shape dependence of holographic mutual information in AdS_4*, *JHEP* **02** (2015) 005 [arXiv:1411.3608] [INSPIRE].

[46] J. Cardy, *Some results on the mutual information of disjoint regions in higher dimensions*, *J. Phys.* **A 46** (2013) 285402 [arXiv:1304.7985] [INSPIRE].

[47] L.-Y. Hung, R.C. Myers and M. Smolkin, *Twist operators in higher dimensions*, *JHEP* **10** (2014) 178 [arXiv:1407.6429] [INSPIRE].

[48] P. Calabrese, J. Cardy and E. Tonni, *Entanglement entropy of two disjoint intervals in conformal field theory*, *J. Stat. Mech.* **0911** (2009) P11001 [arXiv:0905.2069] [INSPIRE].

[49] M. Headrick, *Entanglement Rényi entropies in holographic theories*, *Phys. Rev.* **D 82** (2010) 126010 [arXiv:1006.0047] [INSPIRE].

[50] P. Calabrese, J. Cardy and E. Tonni, *Entanglement entropy of two disjoint intervals in conformal field theory II*, *J. Stat. Mech.* **1101** (2011) P01021 [arXiv:1011.5482] [INSPIRE].

[51] A. Coser, L. Tagliacozzo and E. Tonni, *On Rényi entropies of disjoint intervals in conformal field theory*, *J. Stat. Mech.* **1401** (2014) P01008 [arXiv:1309.2189] [INSPIRE].

[52] C. De Nobili, A. Coser and E. Tonni, *Entanglement entropy and negativity of disjoint intervals in CFT: Some numerical extrapolations*, *J. Stat. Mech.* **1506** (2015) P06021 [arXiv:1501.04311] [INSPIRE].

[53] J.L. Cardy, *Conformal Invariance and Surface Critical Behavior*, *Nucl. Phys.* **B 240** (1984) 514 [INSPIRE].

[54] J.L. Cardy, *Boundary Conditions, Fusion Rules and the Verlinde Formula*, *Nucl. Phys.* **B 324** (1989) 581 [INSPIRE].

[55] J.L. Cardy, *Boundary conformal field theory*, hep-th/0411189 [INSPIRE].

[56] D.M. McAvity and H. Osborn, *Energy momentum tensor in conformal field theories near a boundary*, *Nucl. Phys.* **B 406** (1993) 655 [hep-th/9302068] [INSPIRE].

[57] D.M. McAvity and H. Osborn, *Conformal field theories near a boundary in general dimensions*, *Nucl. Phys.* **B 455** (1995) 522 [cond-mat/9505127] [INSPIRE].

[58] K. Jensen and A. O'Bannon, *Constraint on Defect and Boundary Renormalization Group Flows*, *Phys. Rev. Lett.* **116** (2016) 091601 [arXiv:1509.02160] [INSPIRE].

[59] S.N. Solodukhin, *Boundary terms of conformal anomaly*, *Phys. Lett.* **B 752** (2016) 131 [arXiv:1510.04566] [INSPIRE].

[60] D. Fursaev, *Conformal anomalies of CFT's with boundaries*, *JHEP* **12** (2015) 112 [arXiv:1510.01427] [INSPIRE].

[61] C.P. Herzog, K.-W. Huang and K. Jensen, *Universal Entanglement and Boundary Geometry in Conformal Field Theory*, *JHEP* **01** (2016) 162 [arXiv:1510.00021] [INSPIRE].

[62] K.-W. Huang, *Boundary Anomalies and Correlation Functions*, *JHEP* **08** (2016) 013 [arXiv:1604.02138] [INSPIRE].

JHEP08(2018)164

[63] C.P. Herzog and K.-W. Huang, *Boundary Conformal Field Theory and a Boundary Central Charge*, *JHEP* **10** (2017) 189 [arXiv:1707.06224] [INSPIRE].

[64] D. Deutsch and P. Candelas, *Boundary Effects in Quantum Field Theory*, *Phys. Rev.* **D 20** (1979) 3063 [INSPIRE].

[65] C. Bachas, *Asymptotic symmetries of AdS_2 branes*, in *Proceedings, Meeting on Strings and Gravity: Tying the Forces Together: 5th Francqui Colloquium: Brussels, Belgium, October, 19-21, 2001*, pp. 9–17, hep-th/0205115 [INSPIRE].

[66] A. Karch and L. Randall, *Locally localized gravity*, *JHEP* **05** (2001) 008 [hep-th/0011156] [INSPIRE].

[67] O. DeWolfe, D.Z. Freedman and H. Ooguri, *Holography and defect conformal field theories*, *Phys. Rev.* **D 66** (2002) 025009 [hep-th/0111135] [INSPIRE].

[68] T. Takayanagi, *Holographic Dual of BCFT*, *Phys. Rev. Lett.* **107** (2011) 101602 [arXiv:1105.5165] [INSPIRE].

[69] M. Fujita, T. Takayanagi and E. Tonni, *Aspects of AdS/BCFT*, *JHEP* **11** (2011) 043 [arXiv:1108.5152] [INSPIRE].

[70] M. Nozaki, T. Takayanagi and T. Ugajin, *Central Charges for BCFTs and Holography*, *JHEP* **06** (2012) 066 [arXiv:1205.1573] [INSPIRE].

[71] A. Faraji Astaneh and S.N. Solodukhin, *Holographic calculation of boundary terms in conformal anomaly*, *Phys. Lett.* **B 769** (2017) 25 [arXiv:1702.00566] [INSPIRE].

[72] R.-X. Miao, C.-S. Chu and W.-Z. Guo, *New proposal for a holographic boundary conformal field theory*, *Phys. Rev.* **D 96** (2017) 046005 [arXiv:1701.04275] [INSPIRE].

[73] C.-S. Chu, R.-X. Miao and W.-Z. Guo, *On New Proposal for Holographic BCFT*, *JHEP* **04** (2017) 089 [arXiv:1701.07202] [INSPIRE].

[74] A. Faraji Astaneh, C. Berthiere, D. Fursaev and S.N. Solodukhin, *Holographic calculation of entanglement entropy in the presence of boundaries*, *Phys. Rev.* **D 95** (2017) 106013 [arXiv:1703.04186] [INSPIRE].

[75] T. Azeyanagi, A. Karch, T. Takayanagi and E.G. Thompson, *Holographic calculation of boundary entropy*, *JHEP* **03** (2008) 054 [arXiv:0712.1850] [INSPIRE].

[76] K. Jensen and A. O'Bannon, *Holography, Entanglement Entropy and Conformal Field Theories with Boundaries or Defects*, *Phys. Rev.* **D 88** (2013) 106006 [arXiv:1309.4523] [INSPIRE].

[77] D.V. Fursaev and S.N. Solodukhin, *Anomalies, entropy and boundaries*, *Phys. Rev.* **D 93** (2016) 084021 [arXiv:1601.06418] [INSPIRE].

[78] C. Berthiere and S.N. Solodukhin, *Boundary effects in entanglement entropy*, *Nucl. Phys.* **B 910** (2016) 823 [arXiv:1604.07571] [INSPIRE].

[79] R.-X. Miao and C.-S. Chu, *Universality for Shape Dependence of Casimir Effects from Weyl Anomaly*, *JHEP* **03** (2018) 046 [arXiv:1706.09652] [INSPIRE].

[80] J. Erdmenger, C. Hoyos, A. O'Bannon and J. Wu, *A Holographic Model of the Kondo Effect*, *JHEP* **12** (2013) 086 [arXiv:1310.3271] [INSPIRE].

[81] J. Erdmenger, M. Flory, C. Hoyos, M.-N. Newrzella and J.M.S. Wu, *Entanglement Entropy in a Holographic Kondo Model*, *Fortsch. Phys.* **64** (2016) 109 [arXiv:1511.03666] [INSPIRE].

JHEP08(2018)164

[82] J. Erdmenger, M. Flory, C. Hoyos, M.-N. Newrzella, A. O'Bannon and J. Wu, *Holographic impurities and Kondo effect*, *Fortsch. Phys.* **64** (2016) 322 [arXiv:1511.09362] [INSPIRE].

[83] J. Erdmenger, C. Hoyos, A. O'Bannon, I. Papadimitriou, J. Probst and J.M.S. Wu, *Two-point Functions in a Holographic Kondo Model*, *JHEP* **03** (2017) 039 [arXiv:1612.02005] [INSPIRE].

[84] J. Erdmenger, C. Hoyos, A. O'Bannon, I. Papadimitriou, J. Probst and J.M.S. Wu, *Holographic Kondo and Fano Resonances*, *Phys. Rev.* **D 96** (2017) 021901 [arXiv:1611.09368] [INSPIRE].

[85] C.-S. Chu and R.-X. Miao, *Anomalous Transport in Holographic Boundary Conformal Field Theories*, *JHEP* **07** (2018) 005 [arXiv:1804.01648] [INSPIRE].

[86] K. Nagasaki, H. Tanida and S. Yamaguchi, *Holographic Interface-Particle Potential*, *JHEP* **01** (2012) 139 [arXiv:1109.1927] [INSPIRE].

[87] D. Seminara, J. Sisti and E. Tonni, *Corner contributions to holographic entanglement entropy in $AdS_4/BCFT_3$*, *JHEP* **11** (2017) 076 [arXiv:1708.05080] [INSPIRE].

[88] G. Hayward, *Gravitational action for space-times with nonsmooth boundaries*, *Phys. Rev.* **D 47** (1993) 3275 [INSPIRE].

[89] S.W. Hawking and C.J. Hunter, *The gravitational Hamiltonian in the presence of nonorthogonal boundaries*, *Class. Quant. Grav.* **13** (1996) 2735 [gr-qc/9603050] [INSPIRE].

[90] M. Henningson and K. Skenderis, *The Holographic Weyl anomaly*, *JHEP* **07** (1998) 023 [hep-th/9806087] [INSPIRE].

[91] M. Bianchi, D.Z. Freedman and K. Skenderis, *How to go with an RG flow*, *JHEP* **08** (2001) 041 [hep-th/0105276] [INSPIRE].

[92] M. Bianchi, D.Z. Freedman and K. Skenderis, *Holographic renormalization*, *Nucl. Phys.* **B 631** (2002) 159 [hep-th/0112119] [INSPIRE].

[93] K. Skenderis, *Lecture notes on holographic renormalization*, *Class. Quant. Grav.* **19** (2002) 5849 [hep-th/0209067] [INSPIRE].

[94] C.R. Graham and E. Witten, *Conformal anomaly of submanifold observables in AdS/CFT correspondence*, *Nucl. Phys.* **B 546** (1999) 52 [hep-th/9901021] [INSPIRE].

[95] E. Tonni, *Holographic entanglement entropy: near horizon geometry and disconnected regions*, *JHEP* **05** (2011) 004 [arXiv:1011.0166] [INSPIRE].

[96] K. Zarembo, *Wilson loop correlator in the AdS/CFT correspondence*, *Phys. Lett.* **B 459** (1999) 527 [hep-th/9904149] [INSPIRE].

[97] P. Olesen and K. Zarembo, *Phase transition in Wilson loop correlator from AdS/CFT correspondence*, hep-th/0009210 [INSPIRE].

[98] N. Drukker and B. Fiol, *On the integrability of Wilson loops in $AdS_5 \times S^5$: Some periodic ansatze*, *JHEP* **01** (2006) 056 [hep-th/0506058] [INSPIRE].

[99] A. Dekel and T. Klose, *Correlation Function of Circular Wilson Loops at Strong Coupling*, *JHEP* **11** (2013) 117 [arXiv:1309.3203] [INSPIRE].

[100] D.E. Berenstein, R. Corrado, W. Fischler and J.M. Maldacena, *The operator product expansion for Wilson loops and surfaces in the large N limit*, *Phys. Rev.* **D 59** (1999) 105023 [hep-th/9809188] [INSPIRE].

JHEP08(2018)164

[101] C. Kristjansen, G.W. Semenoff and D. Young, *Chiral primary one-point functions in the D3-D7 defect conformal field theory*, *JHEP* **01** (2013) 117 [arXiv:1210.7015] [INSPIRE].

[102] J. Estes, K. Jensen, A. O'Bannon, E. Tsatis and T. Wrase, *On Holographic Defect Entropy*, *JHEP* **05** (2014) 084 [arXiv:1403.6475] [INSPIRE].

[103] J. Aguilera-Damia, D.H. Correa and V.I. Giraldo-Rivera, *Circular Wilson loops in defect Conformal Field Theory*, *JHEP* **03** (2017) 023 [arXiv:1612.07991] [INSPIRE].

[104] M. Preti, D. Trancanelli and E. Vescovi, *Quark-antiquark potential in defect conformal field theory*, *JHEP* **10** (2017) 079 [arXiv:1708.04884] [INSPIRE].

[105] M. De Leeuw, C. Kristjansen and G. Linardopoulos, *Scalar one-point functions and matrix product states of AdS/dCFT*, *Phys. Lett.* **B 781** (2018) 238 [arXiv:1802.01598] [INSPIRE].

JHEP08(2018)164